UNIVERSIDAD DE CHILE
FACULTAD DE CIENCIAS FÍSICAS Y MATEMÁTICAS
DEPARTAMENTO DE INGENIERÍA CIVIL

INTERNAL AND EXTERNAL REINFORCEMENTS FOR HOLES IN GLUED LAMINATED BEAMS

MEMORIA PARA OPTAR AL TÍTULO DE INGENIERO CIVIL

CRISTÓBAL ARNOLDO TAPIA CAMÚ

PROFESOR GUÍA:
SIMON AICHER

MIEMBROS DE LA COMISIÓN:
JUAN FELIPE BELTRAN MORALES
MARIO WAGNER MUÑOZ

This work has been financially supported by the Division of Timber Construction of the Material Testing Institute (Otto Graf Institut), University of Stuttgart

SANTIAGO DE CHILE
2015

RESUMEN DE LA MEMORIA PARA OPTAR AL TITULO DE: Ingeniero Civil
POR: Cristóbal Arnoldo Tapia Camú
FECHA: 11/03/2015
PROFSOR GUÍA: Simon Aicher

Internal and external reinforcements for holes in glued laminated beams

El uso de vigas laminadas encoladas requiere con frecuencia la inclusión de aperturas, con el fin de cumplir con especificaciones arquitectónicas, tales como ductos de ventilación o instalaciones sanitarias, entre otros. La perforación produce concentraciones de esfuerzos de tracción perpendiculares a la dirección de las fibras en la región que bordea la apertura, promoviendo el inicio de una grieta. El Anexo Nacional Alemán (NA) para la norma Europea de diseño de estructuras de madera EN 1995-1-1 provee reglas de diseño para esta situación, incluyéndose aperturas sin reforzar, así como también el uso de uno de entre dos tipos de refuerzos: internos (tipo barra) o externos (tipo placa).

Esta tesis analiza diferentes modelos de elementos finitos (EF) para describir la influencia de refuerzos internos dentro de un elemento de madera laminada encolada. Se observa que modelos 2D tienden a sobrestimar la influencia de los refuerzos internos, mientras que el uso de elementos unidimensionales (lineas), para representar los refuerzos internos dentro de un modelo 3D de la madera laminada encolada, resulta en una clara subestimación de dicha influencia. En otro punto, la posición de los refuerzos internos relativos al punto medio de la sección transversal, influye en la cantidad de fuerza vertical que el refuerzo es capaz de transferir. Esto se debe a la anisotropía cilíndrica que caracteriza a las laminas individuales, lo cual gobierna el comportamiento constitutivo de la madera laminada encolada como material.

Las ecuaciones de diseño contenidas en DIN EN 1995-1-1/NA [18] son revisadas y comparadas contra resultados de EF, donde ciertas discrepancias son encontradas y presentadas. Con base en estos resultados, nuevas ecuaciones son desarrolladas, las cuales contienen coeficientes que son posteriormente calibrados haciendo uso de los datos obtenidos de los modelos de EF. Una relación de dependencia con el tamaño para las concentraciones de esfuerzos es encontrada en las ecuaciones aquí derivadas, esto debido al uso de un radio constante en las esquinas de las aperturas rectangulares, lo cual obedece a una práctica común en la manufactura de las mencionadas perforaciones. Un radio de esquina dependiente de la geometría de la viga resolvería parte de este problema. Finalmente, una serie de test relativamente grande —la cual incluye algunas vigas de pino Radiata de Chile— es llevada a cabo, con el fin de evaluar la efectividad de cada tipo de refuerzo, así como para validar los modelos de EF utilizados en las etapas anteriores. En general se obtiene una concordancia satisfactoria entre los experimentos y los resultados de las simulaciones.

Abstract

Glulam beams often require one or more apertures to comply with architectural specifications, such as passing-through of ventilation ducts or water pipes. The hole induces zones of tensile stress concentrations, perpendicular to grain direction at the periphery of the hole, which promote crack initiation. The German National Annex (NA) to the European timber design code EN 1995-1-1 offers design rules that cover this situation, including unreinforced holes as well as the use of one of two types of reinforcements: internal (rod-like) or external (plate-like).

This thesis analyzes different finite elements (FE) models to describe the influence of internal reinforcements within a glulam timber element. It is found that 2D models tend to overestimate the influence of internal reinforcements, whereas the use of 1D (line) elements, to represent the reinforcement within a 3D model of the glulam timber, results in a clear underestimation of the said influence. Another point is that the positioning of the internal reinforcements relative to the cross-sectional mid-width influences the amount of vertical force they transfer, which is due to the characteristic cylindric anisotropy of the individual laminations which governs the constitutive behavior of the material glulam.

The design equations found in DIN EN 1995-1-1/NA [18] were reviewed and compared against FE-computations, where some discrepancies were found and presented. Based on these results, new design equations are developed, containing coefficients that are then calibrated using the data obtained from FE-Models. A size-dependent relationship for stress concentrations is found in the equations due to the use of a constant corner radius in rectangular holes, which is a common practice in the manufacture of these holes. A corner radius dependent on the beam geometry would solve part of this issue. Finally a fairly large test series, including some glulam beams made of Radiata pine from Chile, was carried out in order to evaluate the effectiveness of each type of reinforcement, as well as to validate the FE-Models used in previous stages. Overall, a satisfactory agreement between experiments and analysis was obtained.

To Clara*,*
to Celsa*...*
the youngest and the most experienced
family member, respectively

Acknowledgments

This thesis was only possible thanks to the incredible support of many great people. In a first place I'd like to thank my supervisor, Dr. Simon Aicher, for giving me this great opportunity to come to Germany to write my thesis, always giving me full support and answering any question I had, and for the instructing field trip to Rosenheim, where I could get more in touch with the German culture. Thanks to everyone at the Division of Timber Constructions of the MPA, University Stuttgart for all the fun *Kaffeepausen* and for simply keeping a great ambiance at the institute. Particularly, I would like to thank Gordian Stapf for always giving me useful LaTeX and Python tips, and for waking my interest in climbing; Zachary Christian for his invaluable help with the English corrections and clearing my confusion between British and American English; and Cyrill Stritzke for helping in the instrumentation set-up for the experiments. Thanks to Markus and Mathias from the institute's laboratory for the help in preparing the experimental tests.

I am very grateful to Mr. Natale Albertani, from the Albertani Corporates, for providing the Radiata pine glulam beams for the experiments and for the very interesting visit inside his glulam-manufacturing fabric. Thanks to Roland Falk for driving with me all the way to Edolo to bring the said beams, and later help me with the glued-on of strain gauges. I would also like to thank my co-supervisor at the University of Chile, Dr. Juan Felipe Beltrán, for immediately supporting this project without hesitation.

I'd like to express my immense gratitude to my family —the extended version of it— for always giving me their support in everything. Thanks Mom and Dad, you are super! Thanks to my sister, Fernanda, for all the fun video calls with my favorite and only (to-date) nice, Clara. Thanks to my friends in Germany for supplying the right amount of distraction during this period (much needed to avoid becoming a thesis-zombie), and to my friends in Chile as well for not losing the contact and keeping me up-to-date as much as possible. A special mention to Karel Mündnich for pointing me the way to Python, which has been a key-part in my work ever since, and to Florencia Ramaciotti for her logistical help in Santiago.

Thanks a lot, you are all awesome!

Contents

List of Tables

List of Figures

Introduction

Timber structures have been present in a large number of cultures since ancient times. From the far east to western civilizations, large and not-so-large timber constructions were designed and built for all thinkable usages: homes, temples, ports or bridges. There are good reasons for that: the material is relatively lightweight, easy to work with and esthetically pleasing when appropriately treated. The rapid development of other construction materials in the past century, such as concrete and steel, and the novel designs that they allowed for, led to a decay in the usage of wood as the main construction material for modern buildings. Over the last decades, however, thanks to the development of better production technologies in glued engineered wood products (e.g. glulam, LVL) and improved material apt design methods, this material has seen a rebirth, as the associative price has become more competitive and as architects and engineers have broadened the possibilities for its usage. Further, the unique sustainability aspect of the natural, regrowing material have contributed to an emerging revival of the material. Larger spans, custom-made curved beams and better connections allow for unique designs to be conceived. Several good examples of timber constructions can be seen in the pavilions from diverse countries at the Expo Milan 2015, such as those from France, Austria or Chile, the latter of which is designed by Cristián Undurraga.

In the field of timber construction, one of the most-used structural elements is the so-called glued laminated (glulam) timber. This element's fabrication method allows for the manufacture of resistant, reliable beams made of a wide variety of woods, which are ready to be installed in-situ. In a typical application, however, glulam beams might require several apertures to comply with architectural requirements, such as the passing-through of ventilation or water pipes, among others. These holes weaken the beam locally and produce zones of high stresses perpendicular to grain direction, which considerably reduces the capacity of the element. The stress concentrations at the hole periphery may induce crack propagations along the grain direction which can lead, in the worst cases, to global failure. In order to improve the resistance to such stresses, internal or external reinforcements may be incorporated. Various reinforcement technologies are standardized in the DIN EN 1995-1-1/NA [18], each having a different influence on the behavior of the stress concentrations at the hole periphery.

The mentioned Standard has some known problems regarding the design of holes in glulam beams. Among these is the equation used to determine the force needed to be carried by the reinforcement, which, according to recent investigations [1], might give unsafe results for specific configurations. At the same time, there are some small misconceptions regarding the way a reinforcement should do its job, specifically on whether they should prevent the

initiation of the crack or not, in order to be considered effective.

In this thesis, the above described problem is analyzed from different points of view to satisfy the following objectives:

- study the stress distribution in the vicinity of a hole with various shapes (round, quadratic and rectangular) by means of FE-models accounting for the anisotropic material behavior at different approximation levels;
- study the behavior of an internal bar-type reinforcement in a glulam cube subject to tensile forces with different types of finite element (FE) models, in order to determine which alternatives give better results regarding the rod influence range and to give recommendations for their positionings;
- review the equation to compute the tensile force perpendicular to grain described in DIN EN 1995-1-1/NA [18];
- propose new design equations that fit the results obtained from the FE-models created;
- analyze the performance of the different kinds of reinforcements by means of experimental testings;
- validate the computational models created with he help of the test series, herby including some glulam beams of Radiata pine from Chile.

In order to achieve these objectives, a parametrical FE-model capable of describing a glulam beam with holes of different shapes and sizes and with internal or external reinforcements will be created, as well as a series of different models to analyze the influence of the material simplifications that could be made.

Chapter 1

Geometric and mechanical properties of wood and timber elements

Unlike most of the commonly used building materials, wood is characterized by the presence of a marked anisotropy ($f_{t,0,k}/f_{t,90,k} \approx 40$ and $f_{t,0,k}/f_{m,k} = 0.6$ to 0.7), which derives from the radial growth of the cells around the tree's stem and from the orientation along the tree's stem axis of these grain-like cells, with longitudes of 3 mm to 5 mm and diameters ranging from 20 µm to 50 µm. In a first idealization, this can be represented as a conical material anisotropy, where the diameter gradually decreases around an assumed straight stem from bottom to top [2]. Due to the small relevance of this change in diameter for most of the practical cases, a further simplification can be made, by which the material resembles a cylindrical anisotropy. Given this model, the three principal material axes are the stem axis (pith) and the radial (R) and tangential (T) directions located on a plane normal to the stem axis. Another inhomogeneity is present along the radial direction, where year after year a succession of earlywood (thin cell walls with reduced strength) and latewood (thicker cell walls with greater strength) takes place [27], creating a periodical change in the material properties along this direction. However, this later inhomogeneity can be disregarded in favor of a quasi-homogeneous continuum, when the analysis is to be performed on a macroscale basis [2].

In this chapter the mechanical properties of wood are discussed and their influence on timber elements —specifically glulam— is presented. A correct understanding of the constitutive relations of wood is necessary in order to have a better insight into the main problem to be addressed in this thesis, as well as to comprehend how the FE-Models were built.

1.1 Cylindrical-anisotropic behavior

1.1.1 Within the whole cross section of a tree

Probably one of the most characteristic attributes of wood of trees growing in the northern hemisphere with distinct seasonal climatic differences throughout the year are their concentric year rings, visible when a transversal cut of a trunk is made. Every year, between the months of April and August a layer of new cells grows from the cambium, in a process that can be separated in two stages. In the first stage, during the early sumer period, a layer of thin-walled cells is produced, which is commonly known as earlywood. During the second stage, a relative thick-walled, more compact layer of cells begins to grow. This is the so-called latewood, which normally has a darker color and whose function is primarily to give wood its strength, whereas earlywood is responsible for water transportation [27]. In the southern hemisphere this occurs the other way around.

The progressive addition of new material in a radial manner yields to a variation of the mechanical properties in different directions, along a plane perpendicular to the stem axis. In addition, a notable difference in the mechanical behavior is observed between the longitudinal direction and the ones contained in the plane just described, which is explained by the spacial orientation of the cells in the trunk. A simplified geometry, well suited to fit this type of anisotropy, is that of a cone [2]. This can be thought of as the gradual reduction in the diameter from bottom to top, along the stem axis. None the less, due to the non-triviality of such a model, it would overcomplicate any attempt of considering the anisotropy of wood, and furthermore, the variation in the diameter can normally be ignored without any big loss of generality.

The aforementioned leads us to a more practical model, through a further simplification, which is that of cylindrical anisotropy. Within this model, three principal material axes are defined: the stem axis (pith) and the radial (R) and tangential (T) directions located on a plane normal to the stem axis, as shown in Figure 1.1. Such a model presents the advantage of being able to be implemented in any modern finite element program, as opposed to that of a conic, and is furthermore very intuitive. However, as previously mentioned, another variation in the mechanical properties has to be addressed, namely the fluctuation of the density and herein the correlated surface hardness and stiffness along the radial direction, due to the difference between earlywood and latewood (see Figure 1.2). If one takes into account the number of rings that are present normally in a specimen, this fluctuation becomes less relevant. This is due to the fact that on a macroscale basis such a monotonic, constrained oscillation looks and behaves more as if this perturbation would not exist. Thus, gaining the label of a quasi-homogeneous continuum and eliminating the problem presented by the inhomogeneous behavior.

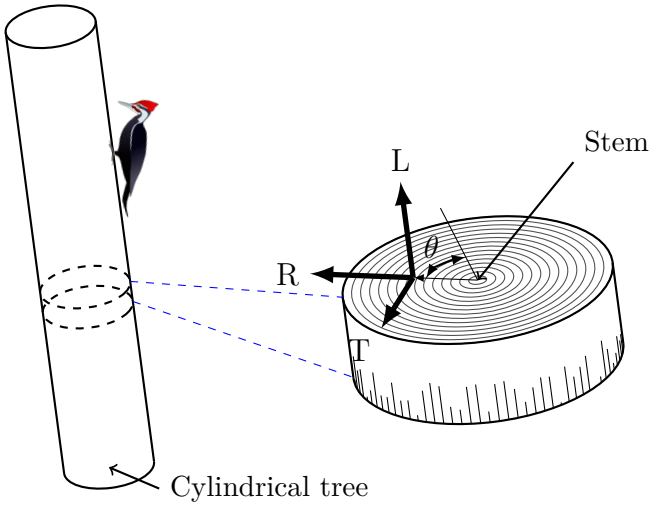

Figure 1.1: *Description of the cylindrical geometry of the section of a idealized tree.*

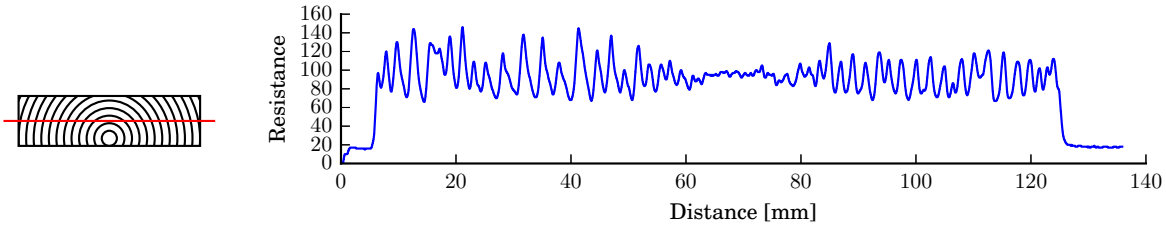

(a) ***(b)***

Figure 1.2: *The figure (b) shows an example of the variation in the resistance of a drilled-through board along the path showed in (a), which lays almost on the radial direction of a transversal plane of the lamination.*

1.1.2 Within a single lamination

For the tree to be used as a structural material it would first normally need to be processed and reduced to individual laminations as shown in Figure 1.3a. Each lamination will of course follow the above described cylindrical anisotropy, but since it is now an arbitrary region of the original stem, two new parameters need to be introduced to fully describe the geometry. These are the distances const.=-d and const.=e, which depict the distances from the bottom of the lamination to the pith along the y-axis, and from the mid-width point of the lamination to the same point along the x-axis, respectively. These two variables can easily be identified on Figure 1.3b, where the local coordinates for an arbitrary point are also shown. The position of the pith depends on the sawing pattern used to obtain the boards and thus, it may just as well be found on the inner, as on the outer region of the lamination's profile.

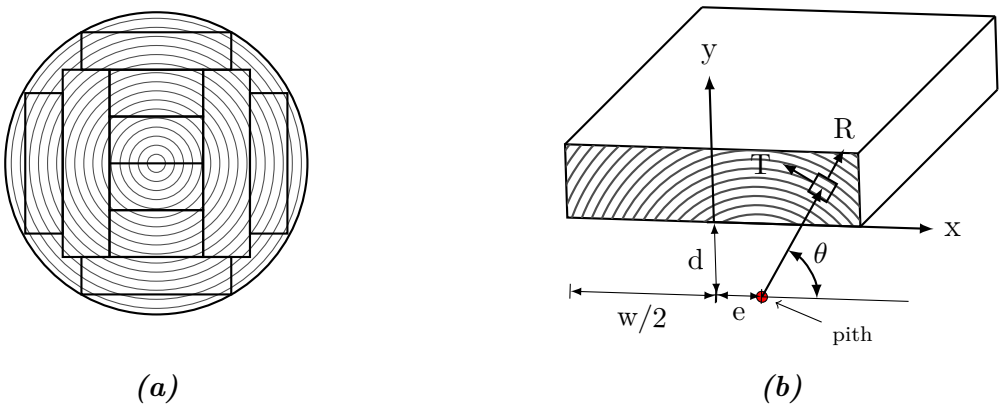

Figure 1.3: *The figure (a) shows exemplary a sawing pattern, that could be used to obtain different laminations. Figure (b) depicts the material coordinate system for a single lamination and its different parameters.*

1.1.3 Within glued laminated timber

The next step is to put a series of the above described single laminations, one on top of the other, which results in a glued laminated beam (referred here as glulam beam). Now we have a set of local cylindrical coordinate systems, one for each lamination. For the particular case where one would like to precisely describe the mechanical behavior of a specific glulam, each one of the piths would have to be adjusted to describe the locations of the real ones. There are, however, some patterns that are more likely to show up. Aicher and Dill-Langer [2] investigated three lay-ups, which have all their piths on the same side, as the European glulam product and production standard DIN EN 14080 [14] requires. These are shown in 1.4a–c, where the different values for the parameters d and e can be seen. Although they used specific geometric dimensions for the width and height of each board (150 mm and 33 mm resp.), the main idea of the different combinations can be applied to any size of laminations.

The lay-ups presented in Figure 1.4 are composed of an alternated repetition of two given laminations, each of which have their own values for the location of their piths, namely d_1 and d_2 for vertical distance, and e_1 and e_2 for the relative to mid-width horizontal shifting.

1.2 Constitutive relationships for timber laminations

In the last section the anisotropic behaviour of a typical lumber element is briefly described and a cylindric geometry is chosen to represent it. For this system three principal axis are introduced, namely the radial (R), tangential (T) and an axis parallel to the stem's axis (L). With this notation the Hook's law relationship for wood takes the form shown in equations 1.1 and 1.2 [9].

$$\boldsymbol{\varepsilon} = \boldsymbol{S}\boldsymbol{\sigma} \tag{1.1}$$

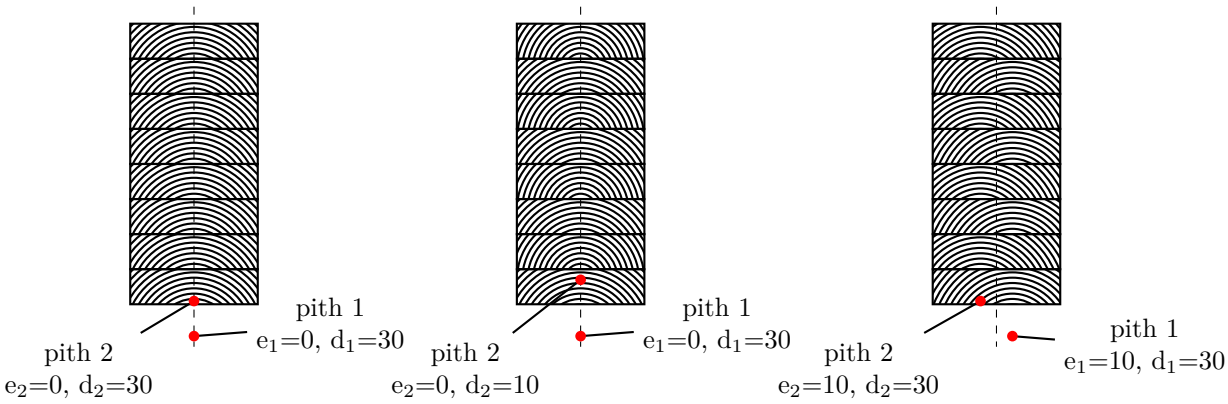

(a) *Configuration* k1. ***(b)*** *Configuration* k2. ***(c)*** *Configuration* k3.

Figure 1.4: *Description of the three different lay-ups of the laminations used in the simulations with finite elements. Dimensions in mm.*

$$\begin{bmatrix} \varepsilon_L \\ \varepsilon_R \\ \varepsilon_T \\ \gamma_{RT} \\ \gamma_{LT} \\ \gamma_{LR} \end{bmatrix} = \begin{bmatrix} s_{11} & s_{12} & s_{13} & 0 & 0 & 0 \\ s_{21} & s_{22} & s_{23} & 0 & 0 & 0 \\ s_{31} & s_{32} & s_{33} & 0 & 0 & 0 \\ 0 & 0 & 0 & s_{44} & 0 & 0 \\ 0 & 0 & 0 & 0 & s_{55} & 0 \\ 0 & 0 & 0 & 0 & 0 & s_{66} \end{bmatrix} \begin{bmatrix} \sigma_L \\ \sigma_R \\ \sigma_T \\ \sigma_{RT} \\ \sigma_{LT} \\ \sigma_{LR} \end{bmatrix}, \tag{1.2}$$

where ε and σ are vectors of strain and stress, respectively, and the matrix $\boldsymbol{S}$ is

$$\boldsymbol{S} = \begin{bmatrix} \frac{1}{E_L} & -\frac{\nu_{RL}}{E_R} & -\frac{\nu_{TL}}{E_T} & 0 & 0 & 0 \\ -\frac{\nu_{LR}}{E_L} & \frac{1}{E_R} & -\frac{\nu_{TR}}{E_T} & 0 & 0 & 0 \\ -\frac{\nu_{LT}}{E_L} & -\frac{\nu_{RT}}{E_R} & \frac{1}{E_T} & 0 & 0 & 0 \\ 0 & 0 & 0 & \frac{1}{G_{RT}} & 0 & 0 \\ 0 & 0 & 0 & 0 & \frac{1}{G_{LT}} & 0 \\ 0 & 0 & 0 & 0 & 0 & \frac{1}{G_{LR}} \end{bmatrix} \tag{1.3}$$

As it will be seen later on, the conversion between cylindrical coordinate system and Cartesian one will be used to calculate stresses and forces in off-axis directions, important for engineering solutions of the shown mechanical problem. To achieve this, a transformation matrix, $\boldsymbol{T}$, needs to be used, like shown in eq. 1.4. Although this procedure is automatically done within the FE program, it should be shown here.

$$\boldsymbol{\sigma}_{\text{cart}} = \boldsymbol{T}\boldsymbol{\sigma} \tag{1.4}$$

$$\begin{bmatrix} \sigma_z \\ \sigma_x \\ \sigma_y \\ \sigma_{xy} \\ \sigma_{xz} \\ \sigma_{yz} \end{bmatrix} = \begin{bmatrix} 1 & 0 & 0 & 0 & 0 & 0 \\ 0 & \cos^2\theta & \sin^2\theta & -2\sin\theta\cos\theta & 0 & 0 \\ 0 & \sin^2\theta & \cos^2\theta & 2\sin\theta\cos\theta & 0 & 0 \\ 0 & \sin\theta\cos\theta & -\sin\theta\cos\theta & \cos^2\theta - \sin^2\theta & 0 & 0 \\ 0 & 0 & 0 & 0 & -\sin\theta & \cos\theta \\ 0 & 0 & 0 & 0 & \cos\theta & \sin\theta \end{bmatrix} \begin{bmatrix} \sigma_L \\ \sigma_R \\ \sigma_T \\ \sigma_{RT} \\ \sigma_{LT} \\ \sigma_{LR} \end{bmatrix} \tag{1.5}$$

Specifically, to obtain the stresses perpendicular to grain on any point, equation 1.6 has to be applied.

$$\sigma_y = \sin^2\theta \cdot \sigma_R + \cos^2\theta \cdot \sigma_T + 2\sin\theta\cos\theta \cdot \sigma_{RT} \tag{1.6}$$

1.3 Board and glulam strength classes acc. to DIN EN 14080

1.3.1 Board properties

In order for a glulam beam to be used as a structural element, it first needs to be classified according to its mechanical properties. The procedure established to do this is found in DIN EN 14080 [14], which is briefly explained afterwards.

In a first step the properties of the boards used to build up the glulam beams need to be obtain. These properties are the tensile strength, the modulus of elasticity (MOE) parallel to fiber direction and the density. The later is correlated to the elastic modulus for the European wood, which is why it is also listed as a variable for the classification. With this information the boards can then be categorized acc. to the T-Classes described in DIN EN 14080 [14], a commonly-used subset of which is shown in Table 1.1. Visual grading is possible in a first stage for Classes, which helps sorting the boards before they are tested. The most relevant German visual grading classes are the so-called S-Classes (S10, S13). For the higher T-Classes it is no longer possible to use the visual grading and the aid of specially designed grading-machines is needed to carry out this job.

Since the boards used in glulam beams are connected to one another by means of finger-joints, the strength of this connection must also be determined. This is achieved through standardized tests, where the connections are tested in a bending test along the flat edge of the board. In this manner the bending strength, $f_{m,j,k}$, is acquired, which, in conjunction with the T-Class, helps determining the glulam strength class.

Table 1.1: *Tensile strength of glulam boards acc. DIN EN 14080 [14] for the most commonly used T-Classes*

Tensile-strength class of boards (T-Class)	Visual-grading class	Corresponding bending strength class; C-Class [1]	Tensile strength $f_{t,0,\ell,k}$	Modulus of elasticity $E_{0,\text{mean}}$	Density ρ_k
			N/mm^2	N/mm^2	kg/m^3
T14	S 10	C24	14	11	350
T18		C30	18	12	380
T21	S 13	C35	21	13	390
T22	machined grading	C36	22	13	390
T26		C40	26	13.5	410
T27		C45	27	15	410
T30		50	30	15.5	430

1: The C-Classes refer to edgewise bending strength, i.e. C24 is characterized by a characteristic (5 % quantile) bending strength (edgewise) of $24\,\text{N/mm}^2$

1.3.2 Glulam build-up and classification

Glulam beams can be manufactured out of up to three regions of boards with different T-Classifications, as shown in Figure 1.5. The main idea of composite glulam beams is to have laminations with larger strengths on the border regions, where larger stresses are expected, and relative lower strengths ones on the core region, where the stresses are smaller, in order to optimize the use of material. Homogeneous glulam beams (made of one T-Class boards only) are also common and can be identified by the letter *h* appended at the end of the glulam class, which has the following nomenclature: *GL XX h*; where the *XX* represents the bending strength and the final letter can be *h* for homogeneous, or *c* for lined build-up (see Table 1.2 for examples).

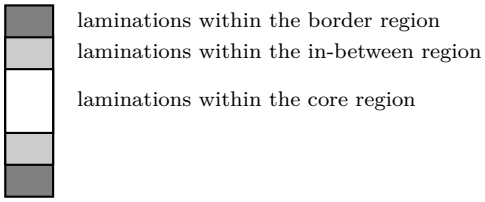

Figure 1.5: *Cross section of a glulam beam showing the different nomenclatures for the laminations within different regions.*

The bending strength for homogeneous glulam beams is computed using the Equation 1.7, which will deliver the respective glulam(GL)-Strength-Class. For composite beam sections, like the one presented in Figure 1.5, the elastic compound theory should be taken into account to derive the apparent strength properties of the combined build-up.

The procedure to classify a specific glulam is carried out in Appendix B to determine the characteristic values of the Radiata Pine used for some of the experimental tests. The glulam beam used in the example is homogeneous, consisting only of T-15 graded laminations.

$$f_{m,g,k} = -2.2 + 2.5 f_{t,0,\ell,k}^{0.75} + 1.5 \left(\frac{f_{m,j,k}}{1.4} - f_{t,0,\ell,k} + 6 \right)^{0.65} \tag{1.7}$$

Table 1.2: *Glulam classes for softwood according to DIN EN 14080 [14]*

Wood type	Glulam strength-class	Laminations within the border-region or full cross-section			Laminations within the core-region		
		strength classes –	percent of cross-section [%]	bending strength of finger-joints [N/mm^2]	strength classes –	percent of cross-section [%]	bending strength of finger-joints [N/mm^2]
Softwood	GL 24h	T14	100	30	–	–	–
	GL 24c	T14	2x33	31	T9	34	19
	GL 28c	T21	2x17	36	T14	66	26
	GL 30c	T22	2x17	41	T14	66	28
	GL 32c	T26	2x17	45	T14	66	26

Chapter 2

Stress distribution in the vicinity of round and rectangular holes

Apertures in glulam beams, as in any other beam, represent a geometrical discontinuity that redistribute the stresses within a region within its close proximity. Depending on the shape of the hole, large stress concentrations may arise, which could lead to a crack initiation that could compromise the structure's integrity. Understanding the principles of this reordering of stresses is of great importance when faced with the design of such elements. Furthermore, if the cylindrical anisotropy described in Chapter 1 is taken into account in the analysis, a more accurate distribution of stresses can be seen, which should lead to a better comprehension of the interaction between reinforcements and the beam.

In this chapter, different configurations of glulam beams with holes (varying in shape, position and loading conditions) will be exemplary shown, in order to give a better insight into the distribution of the stresses in the vicinity of the apertures.

2.1 Stress distributions perpendicular to grain

When dealing with structural timber elements, such as glulam beams, special attention should be paid to the stresses perpendicular to grain, σ_y, due to the relative small resistance that the material offers in this direction. When an aperture is introduced, a redistribution of the stresses takes place near its perimeter and stress concentrations, derived from geometrical discontinuities, arise. A 3-Dimensional, orthotropic finite element (FE) model was created to observe the described situation with different configurations of holes and loading conditions. The program chosen to do this was Ansys v.15.0 with its APDL scripting language, which allows an easy parametrization of diverse variables, such as the hole's dimension and position, material properties, or the beam's dimension, among others. It also offers a very fine control over the discretization of the geometries and allows for the creation of loops, which are a welcome tool when performing a parameter study.

In Figures 2.1a–c the vertical stress distributions for three different configurations with

round holes are illustrated. In Figure 2.1a the aperture is located within the shear-dominated zone of the beam, whereas the configuration shown in Figure 2.1c places the hole in a pure moment area. Figure 2.1b aims to show what happens when the hole is near the loading point. All three configurations use the same beam dimensions and load application points.

In Figure 2.1a a very distinctive pattern of the stresses perpendicular to grain can be

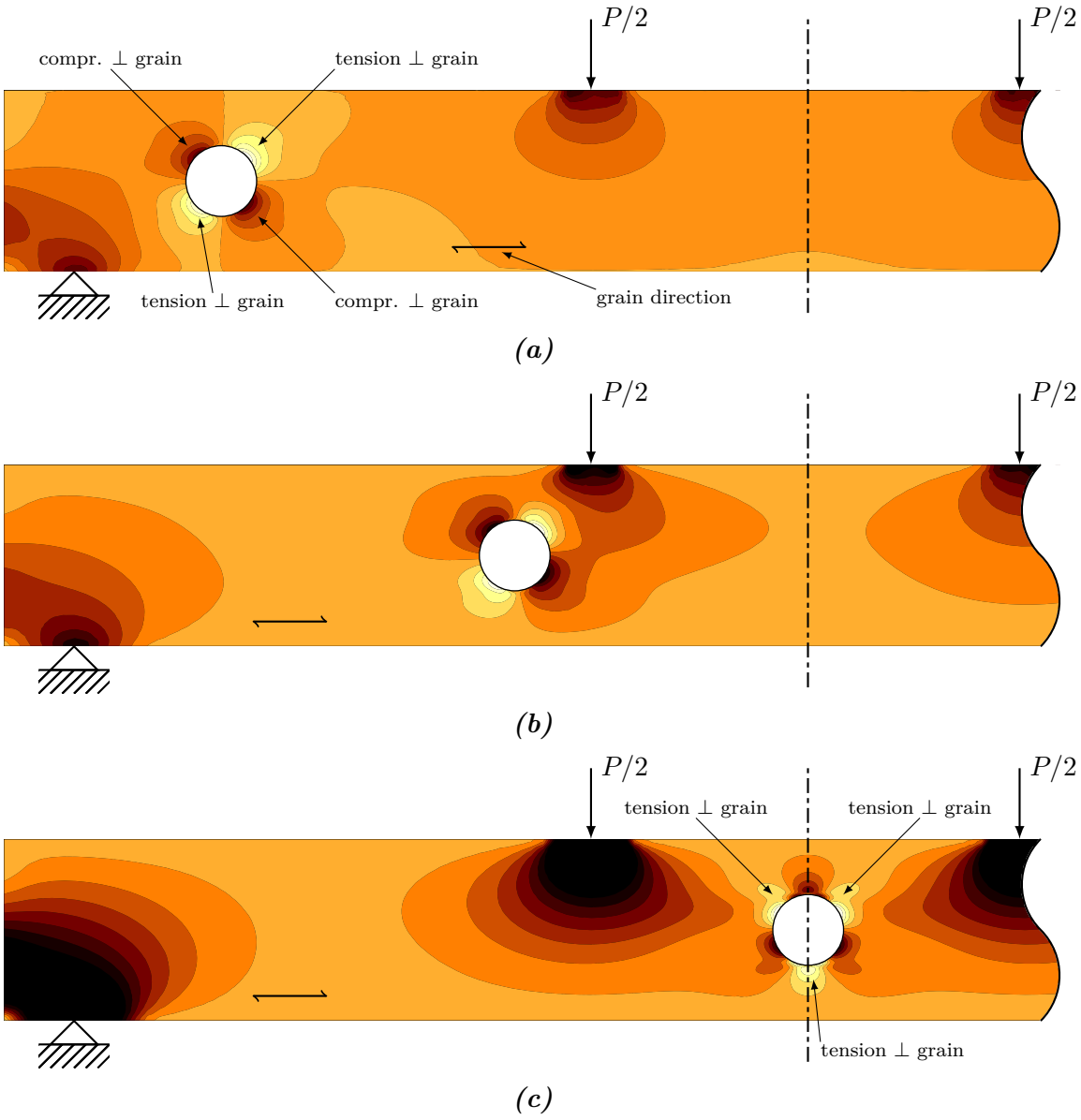

Figure 2.1: *Distribution of stresses perpendicular to grain in a glulam beam with holes at different positions. Lighter colors represent tension zones and darker colors represent compression zones; light orange almost zero stresses perpendicular to grain. (a) The hole is placed at the minimum distance allowed acc. to DIN EN 1995-1-1/NA [18] with respect to the left edge. This also represents the region where the shear force dominates. (b) The hole is placed within the influence zone of the applied load. (c) The hole is placed exactly in the middle of the beam, where, given the loading conditions, only moment is present.*

seen, when a hole is placed in a shear-dominated zone. The distribution consists mainly of two sets of diametrically-opposed regions of tensile and compressive stresses, with their maximum values roughly at angles of 45 °(+180 °) and 135 °(+180 °), forming what one could define as an antisymmetric pattern. The tensile stresses occurring in the given example at the lower left and upper right hole periphery position are precisely one of the main problems with apertures in general and will be analyzed in detail in the course of this thesis. The Figure 2.1b shows the same pattern as the previous one, but because it is near a compression zone, induced by the loading plate, the tensile stresses on the upper right side of the hole are reduced. This can be seen by comparing the tension bulb on the mentioned side against the one on the lower left flank of the hole, by which a bigger tensile zone can be easily noted visually. The Figure 2.1c depicts a quite different situation, where the pattern is now composed of three zones of tensile stresses and three regions of compression stresses, creating a symmetric pattern around a line vertically crossing the hole's center. This is the typical stress distribution for holes in zones of pure moment.

The latter case presented —pure moment— is of special interest here, since it helps to separate the individual effects of moment and shear around a hole, which is of great usefulness when searching for an analytical model. Although a pure shear condition does not exist in the real world, it can artificially be created by subtracting the effects of a pure moment configuration to one where shear is present [3]. By doing this we can easily deduce that the tensile stresses for the upper right corner —when moment and shear are present— should always be bigger than those at the opposite corner, since the ones at the former are superposed with the tensile stresses from the upper right corner of a pure moment case, whereas the ones at the latter corner are superposed with compression stresses from the lower left sector.

In Figures 2.2a to 2.2c other configurations are shown, which include rectangular holes of different height/width ratios (h_d/a) and an evenly distributed load with a round hole. It can be noted, that the stresses create in essence the same pattern as before, only that the stress concentrations for rectangular-like apertures are markedly higher than those of round holes, due to the smaller corner radii. The aperture shown in Figure 2.2b has the biggest h_d/a ratio allowed acc. to DIN EN 1995-1-1/NA [18] equal to 2.5.

2.2 Shear stress distribution

The role of the shear stresses is also to be taken into account when a hole is present. Similarly to what was shown in the previous section, an increment in the shear stresses is observed in the vicinity of an aperture, although the pattern is of course different. Figures 2.3a and 2.3b show this distribution for two different shapes, one with a round hole and the other with a quadrilateral one. Qualitatively they look very alike, but the stresses for the rectangular shape reach higher values near the corners. This result is due to this shape having a much grater geometrical discontinuity as a consequence of having a small corner radius.

It was already mentioned that the tensile concentrations on the two sides of the hole were good candidates to initiate a crack due to the low resistance in the direction perpendicular to grain of the wood, and therefore, it is logical to investigate how the shear stresses interact in

this zone of probable failure. According to the linear fracture mechanics theory three failure modes I, II and III are defined. Mode I is caused by the tensile stresses and modes II and III by the shear stresses in the crack propagation direction and perpendicular to it, respectively. Of the three modes described, mode III is not expected to occur, due the symmetry present in the element, leaving modes I and II as the only ones playing a role in this model. In Figure 2.4, two paths are shown for the shear stresses of models in Figure 2.3, that allow for a better insight into the peaks noted previously. The paths drawn on figures 2.4b and 2.4d start at the point where the vertical stresses reach their maximum and continue horizontally on from

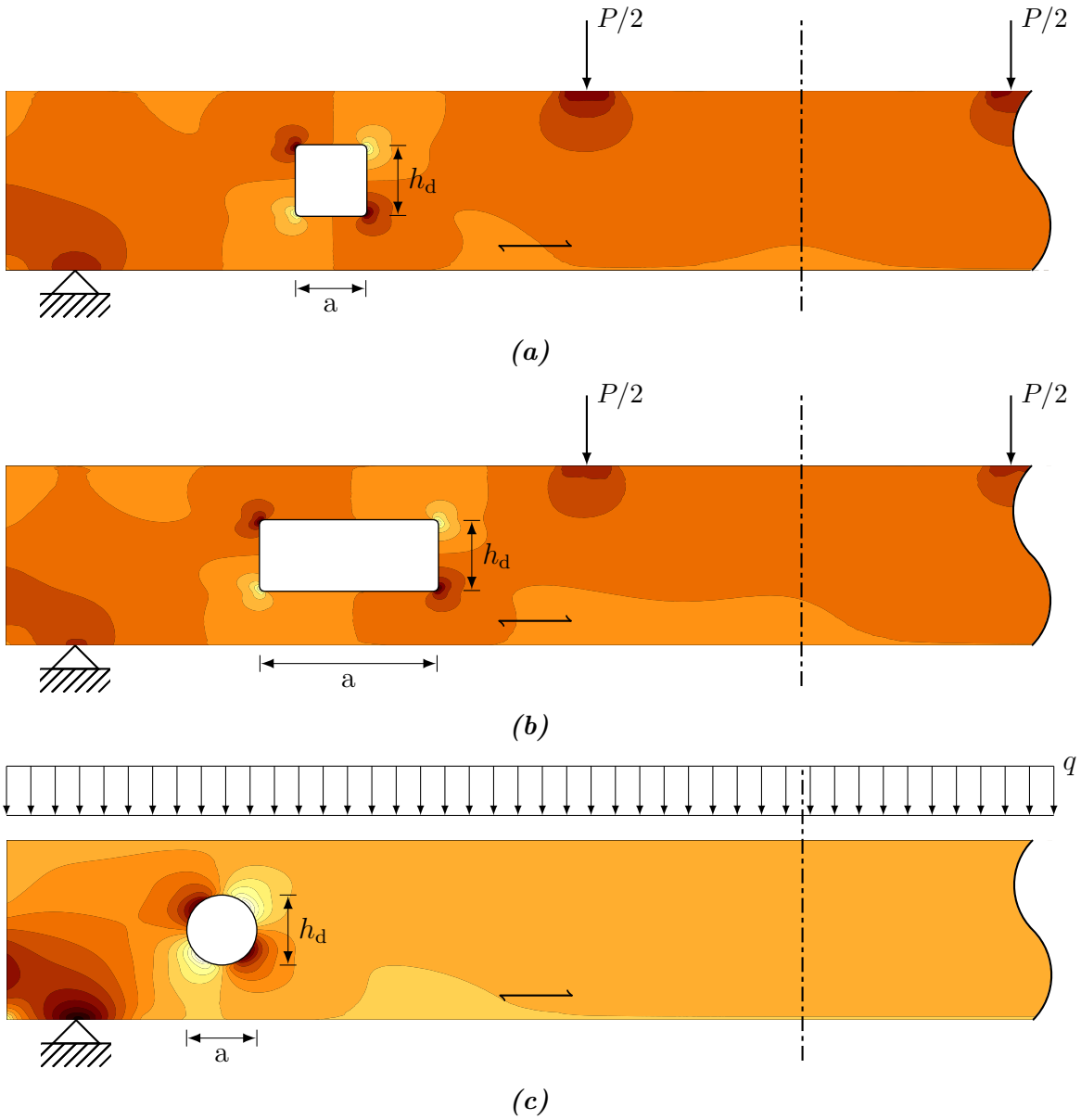

Figure 2.2: *Distribution of stresses perpendicular to grain in a glulam beam with holes with different shapes and loading conditions. Lighter colors represent the tension zones and darker colors represent compression zones. (a) Square hole. (b) Rectangular hole with* $a/h_\mathrm{d} = 2.5$*. (c) Round hole under an evenly-distributed load condition.*

there. The peaks in both models can clearly be seen as well as the difference in magnitude between both maximum values. Figures 2.4a and 2.4c show a vertical path touching the aperture's edge. Worth noting in these figures is the region with little to no shear stress located in the middle of the beam. Due to the presence of the hole, the shear stresses, which would normally be distributed parabolically along the vertical direction, must find another way through the beam to avoid the hole, generating the increment of the vertical stresses discussed in Section 2.1 in the vicinity of the aperture.

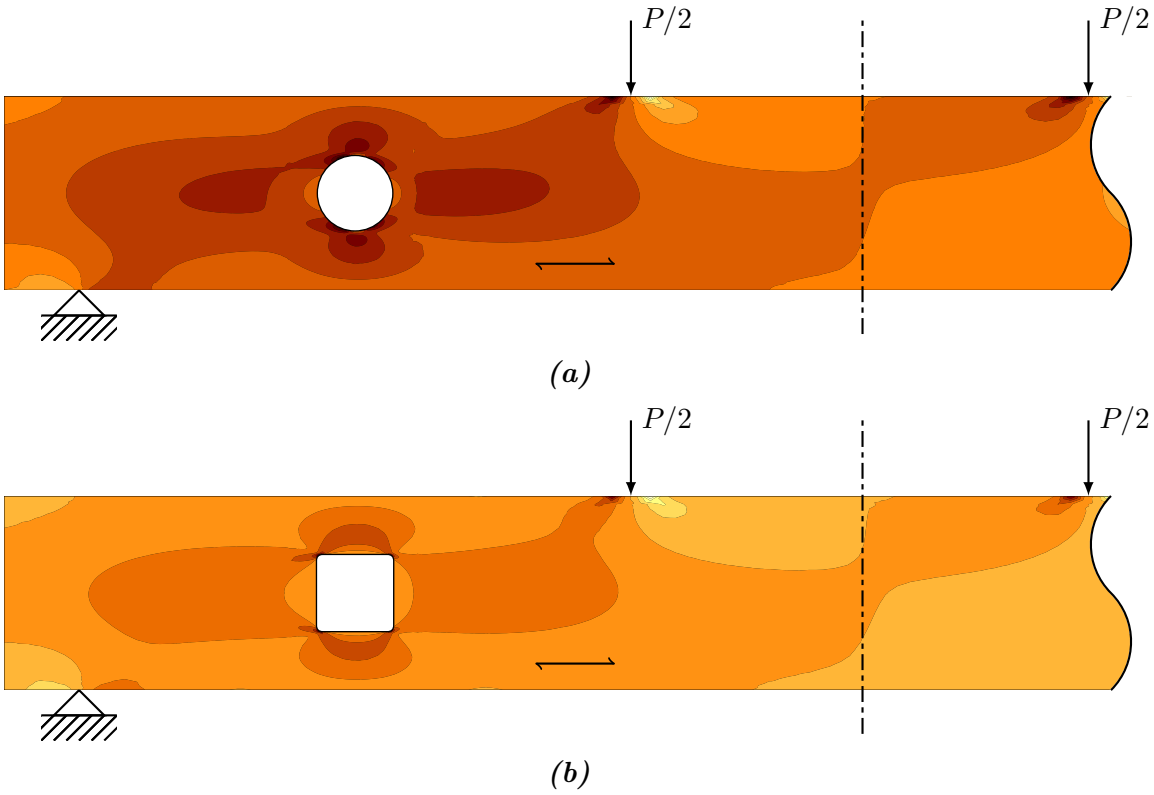

Figure 2.3: *Shear stress distributions for glulam beam models with different hole shapes: (a) round hole and (b) quadrilateral hole. Both holes are placed in a shear-dominated region.*

2.3 Definition of the force $F_{t,90}$

Now that the distribution of the stresses around a hole has been described, an important definition, which is of great importance for the design of glulam beams with holes, can be introduced, namely the force $F_{t,90}$. This force is the one that results from the integration of the vertical stresses along the horizontal path starting from the point of maximum stress value away from the hole until the stresses reach zero. Figure 2.5 depicts this definition exemplarily for the case of a round hole. In this figure the tensile stresses are colored in blue and the compressive ones in red. Following the definition, the value of $F_{t,90}$ is equal to the blue area. This is also valid for the lower left corner, where tensile stresses are present as well.

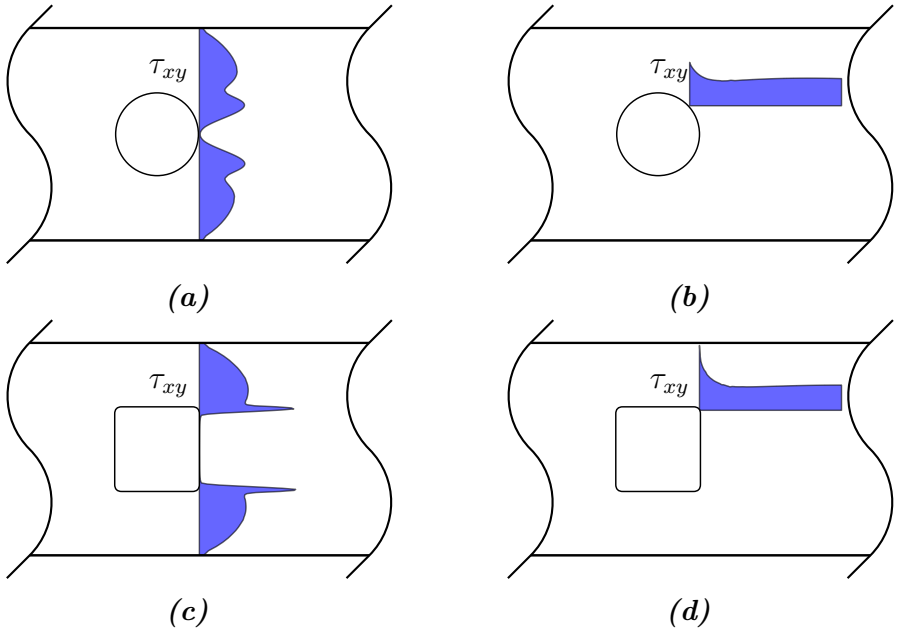

Figure 2.4: *Figures (a) through (d) show exemplary the variation of the shear stresses τ_{xy} in the vicinity of two types of holes. Figure (a) and (c) show a path along the aperture's edge, where peaks can clearly be seen. In Figures (b) and (d) an horizontal path is shown starting in the location of maximum σ_y stress on the hole's periphery. The load conditions correspond to the ones shown in Figures 2.3a and 2.3b respectively.*

The reason why this force is so important for the design as has been mentioned previously, rests on the fact that the vertical stresses are the main cause for crack initiation. This is a force that originally is not there, but after the perforation of a hole it appears and therefore needs somehow to be taken by the beam. If this force is big enough, the glulam beam will need additional help to safely redirect the vertical stresses, calling for the need of reinforcement. The type of reinforcement and the procedure to design them is discussed in Chapter 4.

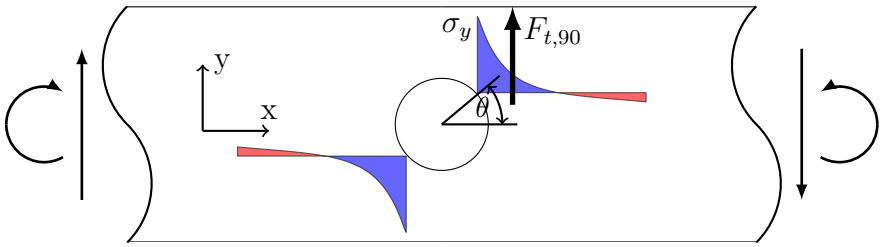

Figure 2.5: *Definition of the force $F_{t,90}$. This force is the integral of the σ_y-stresses along the horizontal path starting at the highest value of σ_y on the corner. The integral only considers the positive values, here showed in blue color.*

Figure 2.5 was created using data extracted from a 3-D orthotropic model. As one would expect from such a model, the vertical stresses along the width-direction remain almost exactly the same for the whole section, as can be seen by the blue areas in Figure 2.6. This figure illustrates the same path described in Figure 2.5 but seen in a 3-Dimensional plane. If the cylindrical anisotropy is considered, then something like what is shown in the red areas of

Figure 2.6 is to be expected. This figure shows clearly the effect that the consideration of the cylindrical anisotropy has on the distribution of the vertical stresses σ_y over the cross section of the beam. It is evident then, that the stresses, when considering this kind of anisotropy, reach peaks of more than twice the value of the ones obtained with an orthotropic model, which gives good reason to think that this model might be better suited for some of the calculations needed in the design process.

The opposite occurs at the sides of the beam, where the σ_y-stresses for the cylindrical-anisotropic model reach lower values, compared to that of the orthotropic model. This result might lead one to think that the $F_{t,90}$ force remains almost the same for both models. Contrarily, however, there might be significant differences, depending on the specific configuration of each beam, where the width of the element or the position of the pith in a single lamination could have a greater or lesser effect. For example, for a beam with a width $w = 100\,\text{mm}$ the difference in $F_{t,90}$ is about 14 % higher with respect to the orthotropic model, and for $w = 260\,\text{mm}$, the difference slightly rises further to about 20 %. It is also important to notice *where* this force is concentrated. For the cylindrical model, the force clearly is concentrated at the mid-width of the beam, but for the orthotropic model, it is almost evenly distributed along the whole section.

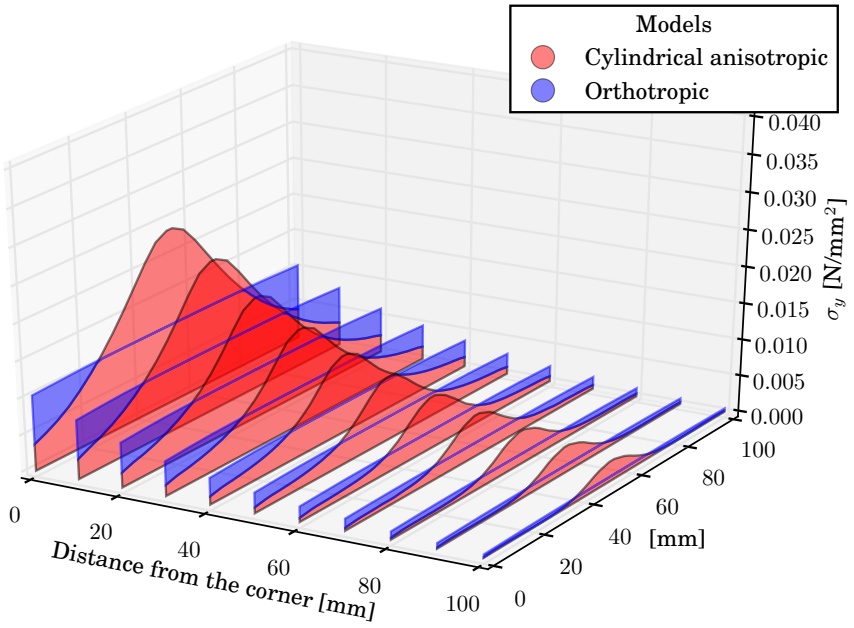

Figure 2.6: *Distribution of the stresses perpendicular to grain on a horizontal plane located at the height on beam where this stresses hit their maximum value on the edge of the hole. The red areas represent the data obtained from a cylindrical-anisotropic FE-model, whilst the blue ones depict the output of an orthotropic 3D model.*

2.4 Discussion

The stress concentrations present around holes in glulam beams play an important role in the integrity of these elements in timber structures. Due to high stresses perpendicular to grain combined with high shear stresses on the edge of the hole, the initiation of a crack seems highly probable, if not inevitable for determined conditions. The need of reinforcement becomes apparent, which for example, for the German national anex of the European code DIN EN 1995-1-1/NA [18], comes in two forms, namely inner reinforcements (screws/rods) or as lateral plates. The definition of the force $F_{t,90}$ comes in handy in the design of such reinforcements, and is thus the basis of the design of holes in glulam beams. An analytical model to calculate $F_{t,90}$ is given in Chapter 4. Later, in Chapter 5, a modification to that model is proposed based on parametrical computations.

Chapter 3

Influence of material simplification

When modeling any kind of structure, different decisions have to be made in order to achieve good results by consuming the least amount of resources possible. Although modern computers can easily handle hundreds of thousands of nodes of a 3-D FE-model, the time consumed by creating it certainly exceeds the time needed to create a simplified version of it. The use of any simplification depends exclusively on each individual problem and on the availability of data supporting it.

A typical beam would normally be modeled as a one-dimensional line, which would be absolutely reasonable due to the loading conditions and the geometry of most problems and should give very good results for normal applications, like the obtention of displacements or internal forces. However, as the complexity of the problem to be solved increases, a more sophisticated model might be necessary to get a better understanding of the present variables. Although perforated beams have mainly been studied with two-dimensional orthotropic models [3] and lately also with three-dimensional orthotropic models [7], it was shown in Chapter 2 that in order to get a better insight into what is happening in the vicinity of a hole, it might be helpful to take into account the cylindrical anisotropy described in Chapter 1.

In this Chapter four different models are investigated to observe the interaction between an internal reinforcement, such as a screw or rod, and glulam timber when subjected to pure tension. The main premise is to observe the amount of the total vertical force that is taken by the screw for each model and be able to compare them in order to select a suitable model for further analysis.

3.1 Problem description

To have an idea of how the modeling of the glulam beam influences the force taken by an internal reinforcement, the situation shown in Figure 3.1 is modeled with four different approaches. This problem consists on a material volume of dimensions $w \times \ell \times h$ that is subjected to an evenly distributed surface load over the top face with a value of $\sigma =$

$1\,\mathrm{N/mm^2}$. The bottom face is constrained in the vertical direction only, so that the stresses can also be evenly distributed. The height is chosen to be $h = 462\,\mathrm{mm}$ and the length is $\ell = 300\,\mathrm{mm}$, whereas the width varies in the range of $w = 100\,\mathrm{mm}$ to $260\,\mathrm{mm}$ in increments of $20\,\mathrm{mm}$. A steel screw-like reinforcement is placed vertically in the middle of the box-type volume ($w/2$ and $\ell/2$) with a length $\ell_s = 264\,\mathrm{mm}$, which is smaller than h, so that the tip of the screw doesn't take force directly from the surface load. The diameter of the reinforcement was also analyzed over a range of $\varnothing = 8\,\mathrm{mm}$ to $24\,\mathrm{mm}$ in increments of $2\,\mathrm{mm}$.

Due to the higher stiffness of the reinforcement in relation to the wood, a redistribution of the stresses in the vicinity of the rod takes place, alleviating the stresses on the wood and passing them to the reinforcement. This redistribution will of course vary with each model and will directly affect the amount of force taken by the rod.

The four FE-models that are described in this chapter are (reference name in parenthesis):

1. a plain-stress two-dimensional model of the problem, where the reinforcement is modeled as a unidimensional element (2D+Beam),

2. a three-dimensional orthotropic model of the glulam timber, with the rod modeled as a unidimensional element as well (3D+Beam),

3. a three-dimensional orthotropic model of the wood and a three-dimensional isotropic model for the reinforcement (3D+3DBeam), and

4. a three-dimensional cylindric-anisotropic model of each lamination of the glulam timber with a three-dimensional isotropic model of the rod (3DCylindric+3DBeam).

In the following sections each one of these models will be described and the results that each one returns will be presented. At the end of the chapter a comparison of all the models is made, while attempting to highlight the important differences.

3.2 2-D orthotropic model of glulam timber with a BEAM-Element to represent the inner reinforcement

3.2.1 Model description

Two-dimensional plain-stress plate elements (PLANE182) were used to describe the geometry required. These elements have four nodes and two degrees of freedom (*dof*) at each node. Plane stress with thickness input was set as one of the so-called *keyoptions* in the program ANSYS, which allows for specification of the desired width. The reinforcement is modeled with a 3-D uniaxial beam element (BEAM188), which is based on the Timoshenko beam theory. This element can have two, three or up to four nodes, however for the elements to interact correctly with the plane elements chosen, they can have a maximum of only two

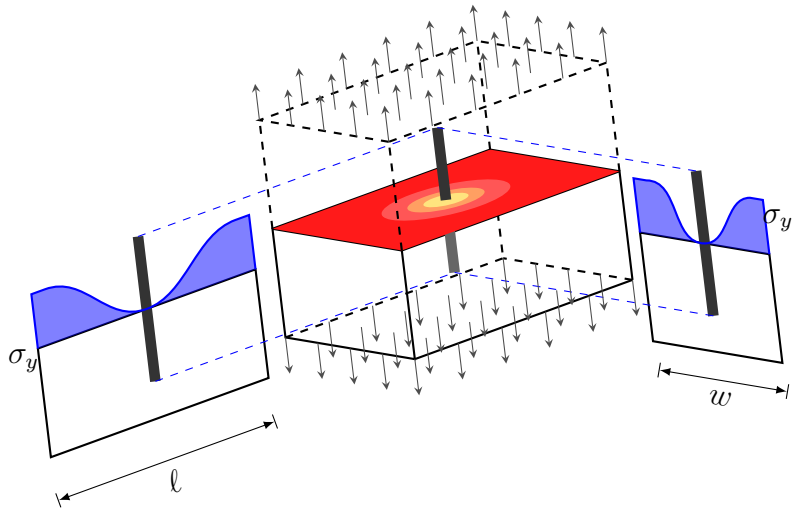

Figure 3.1: *Problem investigated with the different models. It consists of a box-type material volume with dimensions w, ℓ and h which is reinforced with a beam-like element. A vertical load distributed over the top face is applied and the distribution of vertical stresses σ_y is then observed in the zone where the reinforcement has the highest force.*

nodes. Each node has six *dof*, so it is important to constrain the ones that don't play a role in the analyzed plane. All vertical *dof* on the bottom edge of the box-type volume were constrained, plus one horizontal to ensure numerical stability.

The mechanical properties addressed to the timber are given in Table 3.1 and correspond to the glulam class GL32h acc. to DIN EN 14080 [14]. The typical values for steel are also given. The loading was applied as a line load on the upper most edge of the geometry. The size of the elements was chosen to be 5 mm, which should give a good resolution. The whole model was written in the APDL-language, which allowed for the analysis of all the parameters in one run, through use of loops.

Table 3.1: *Mechanical properties for the glulam beam and steel used for the 2-D model*

Glulam		
E_x	13700	N/mm^2
E_y	460	N/mm^2
G_{xy}	850	N/mm^2
ν_{xy}	0.015	–
Steel		
E_{steel}	2.1×10^5	N/mm^2
G_{steel}	7.93×10^4	N/mm^2
ν_{steel}	0.3	–

3.2.2 Results

After running the aforementioned analysis, the results were processed in two different ways. The first way was to present the stresses perpendicular to grain on the mid-height, where the force in the screw achieves its maximum value. A couple of examples are shown in Figure 3.2 for widths of 120 mm and 200 mm and diameters of 10 mm and 20 mm accordingly. Since the load applied on the surface is equal to $1\,\mathrm{N/mm^2}$, then, if the reinforcement wasn't present, the stresses would be equally distributed with a value equal to the applied load. It can be seen that, for example, the maximum values of σ_y in Figure 3.2b lies around $0.5\,\mathrm{N/mm^2}$, meaning that the reinforcement would have reduced the stresses effectively by 50 %. On the other side, if attention is paid to what is happening directly at the position of the steel reinforcement, one can observe that vertical stresses are still present in the wood, even though one would expect them to be much closer to zero, since at that point only the rod is present. This is of course an inherent problem of the model, since nodes belonging to both the reinforcement and the glulam timber are present at the same location. In fact, at every position where a node from the rod is present there is also one from the wood mesh. This means that the wood is also taking force at that point, which is of course not true in the reality. This is, however, the way that such reinforcements are commonly modeled in two dimensions, and complicating it more would probably lead to further issues.

The second way of processing the information retrieved gives a better global understanding of the variation of the two variables studied, namely width and diameter, by plotting the different percentage of force taken by the reinforcement in each combination of width w and rod diameter Ø) in the ranges specified in Section 3.2.1. Figure 3.3 shows what has just been described. In it, a line for each width considered in the analysis is plotted, where the thinner the specimen, the higher the percentage of force that a given screw can take. This makes sense and is what one should expect. But to really be able to make a good judgment about this model, it first needs to be compared against the other alternatives.

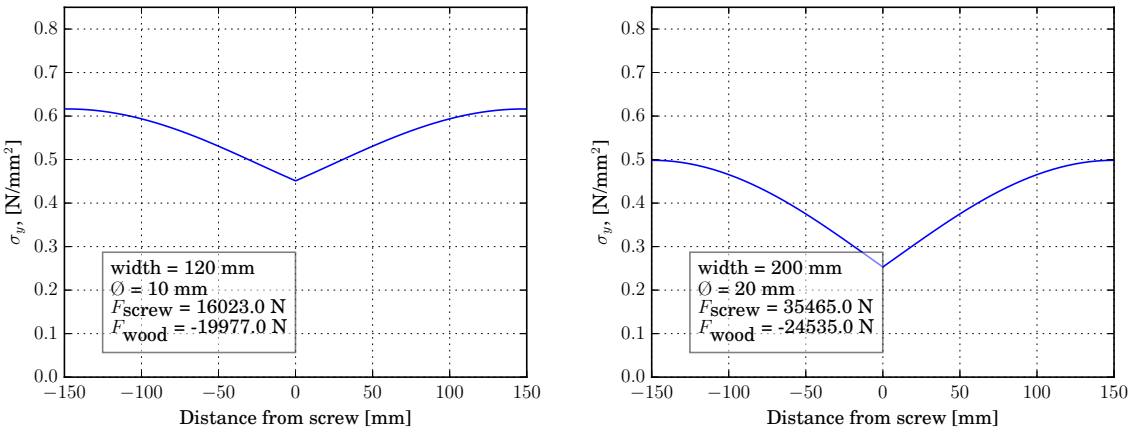

(a) *(b)*

Figure 3.2: *Distribution of σ_y-stresses along the mid-height of the model, where the force in the screw hits its maximum for two different sizes of volume element and rod*

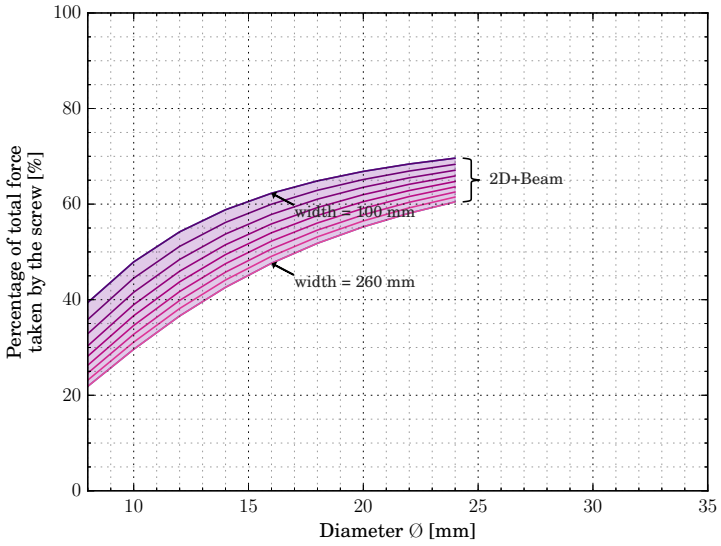

Figure 3.3: *Percentage of force taken by the screw for different widths w and reinforcement diameter Ø, for a 2-D orthotropic model.*

3.3 3-D orthotropic model of glulam timber with a BEAM-Element to represent the inner reinforcement

3.3.1 Model description

The second model to be analyzed is a three-dimensional orthotropic model, where the reinforcement is modeled as a beam element (BEAM188) just like in the previous model. The three-dimensional elements chosen are the SOLID185 ones. These elements have 8 nodes, each of which has three *dof*, corresponding to translations in the three main directions. All vertical *dof* in the bottom plane of the box-type volume were constrained, as well as two others in the length and thickness directions accordingly to ensure numerical stability.

The mechanical properties used to model the glulam timber can be seen in the Table 3.2 and correspond to glulam class GL32h acc. to [14], whilst the properties used for the steel remain the same as shown in Table 3.1. The load was applied evenly along the top face with the ANSYS-command `sfa` and then transfered to the model using `sftran` in the APDL-script.

3.3.2 Results

A similar analysis to the one performed previously was carried out with the data obtained from this model. One difference is that, because the geometry is now three-dimensional, there is now a horizontal plane at the mid-height of the model that needs to be analyzed.

Table 3.2: *Mechanical properties for the glulam beam used for the 3-D orthotropic model*

Glulam		
E_x	13700	N/mm^2
E_y	460	N/mm^2
E_z	460	N/mm^2
G_{xy}	850	N/mm^2
G_{yz}	50	N/mm^2
G_{xz}	850	N/mm^2
ν_{xy}	0.015	–
ν_{yz}	0.35	–
ν_{xz}	0.015	–

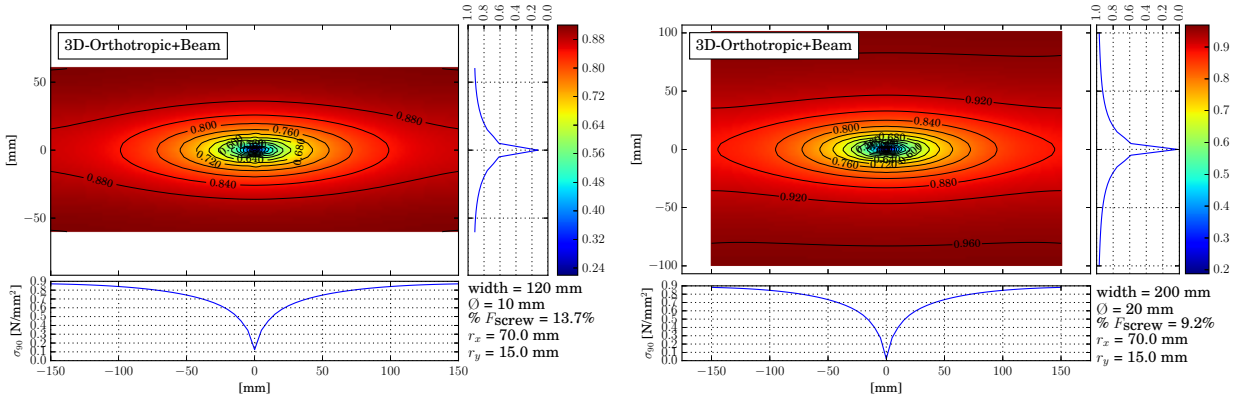

(a) ***(b)***

Figure 3.4: *Distribution of stresses perpendicular to grain in an horizontal plane at mid-height for a 3-D orthotropic model with a beam element representing the reinforcement*

In this plane the stresses perpendicular to grain are observed and a better insight into the influence area of the reinforcement can be obtained. Figure 3.4 shows this plane for the same configurations that were already shown in the 2-D model, namely widths of 120 mm and 200 mm and diameters equal to 10 mm and 20 mm. Concentric ellipse-like level curves are observed in both figures due to the orthotropic behaviour in this model. A minimum value is observed on the position of the beam element (reinforcement), which is smaller than the one obtained in the 2-D model.

This model has the same problem as the two-dimensional model, in the sense that the nodes of the beam element are coupled with the nodes of the wood material and at the same positions. This kind of reinforcement has no volume and thus, does not interact spatially as it would in the real world. This characteristic obliges the solid elements surrounding it to take on more stresses, leaving a smaller part of the total force for the rod to carry, as can be seen in Figure 3.5. Here it can be observed that the percentage of force carried by the reinforcement is considerably reduced, ranging between 6 % to 18 %, which in comparison to the previous model is relatively small.

An additional property observed here is the *influence radius* in both x and y-directions. It is defined here as the distance in each direction (x and y) needed from the center of the reinforcement to reach a σ_y-value of $0.8\,\mathrm{N/mm^2}$, i.e. 80 % of the vertical stresses that would be there without the steel rod. This value was chosen arbitrarily but it should be able to help to compare the efficiency of different configurations of reinforcements and how each of the following models affects it.

3.4 3-D orthotropic model of glulam timber with 3-D Elements to represent the inner reinforcement

3.4.1 Model description

Taking into account the problems detected in the previous models regarding the use of a beam element to represent the internal reinforcement, a third model was designed, that tries to solve this issue by modeling the reinforcement with three-dimensional elements. For this, the same elements implemented previously (SOLID185) were used to model the glulam timber as well as the steel rod. The mechanical properties from Table 3.2 still apply for these computations, as well as the steel properties described in Table 3.1. The same methodology used to apply the surface loads in Section 3.3 is used here as well along with the same constraints.

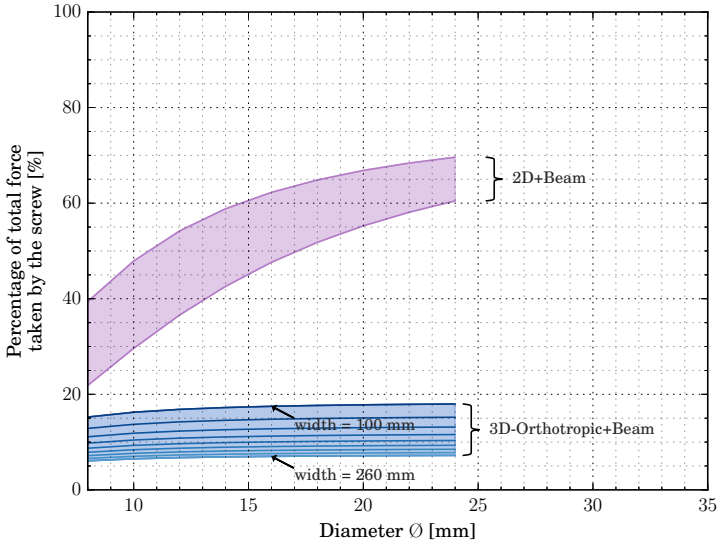

Figure 3.5: *Percentage of force taken by the screw for different combinations of width w and screw diameters Ø, for a 3-D orthotropic model with beam elements to represent reinforcement*

3.4.2 Results

Following the same procedure as before, Figure 3.6a and Figure 3.6b were created from the output of the FE-Analysis. In these two figures a somewhat different picture can be seen in relation to what was shown in the previous section, namely that the area occupied by the reinforcement has now been more accurately reproduced. This time there are no wood elements in the zone where the screw is located, thus representing the actual situation in a more realistic way.

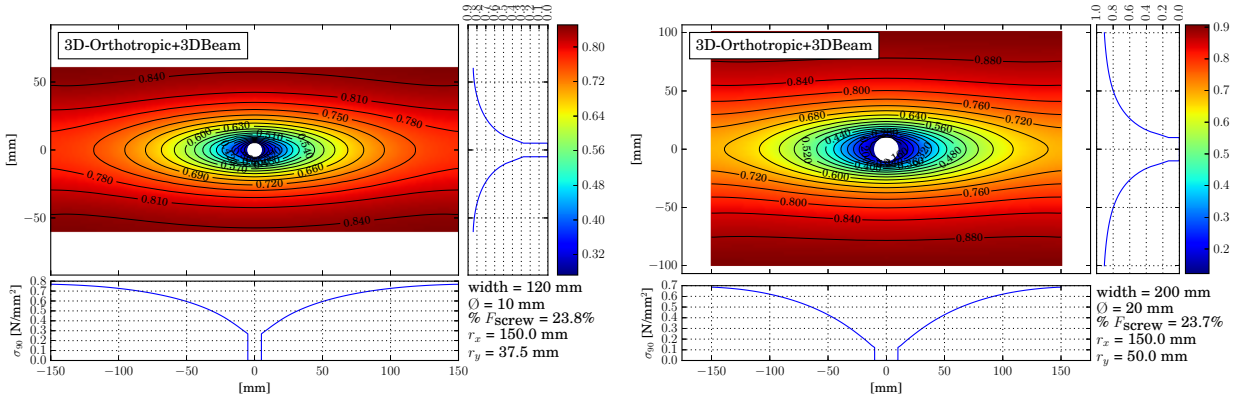

(a) ***(b)***

Figure 3.6: *Distribution of stresses perpendicular to grain for two different configurations of width and diameter of rod. (a) width equals 120 mm and reinforcement Ø is 10 mm; (b) width equals 200 mm and reinforcement Ø is 20 mm*

The defined influence radii can now be compared between this and the former model, where one can see some marked differences. In the x-direction the radius increased from 70 mm to 150 mm for both w =120 mm and 200 mm, with diameters equal to 10 mm and 20 mm accordingly. For the other direction, y, the changes increase from 15 mm to 37 mm and from 15 mm to 50 mm for the widths 120 mm and 200 mm respectively, which represents a change of about three times more than what was deduced with the latter model. The exact values calculated depend on the discretization of the mesh, since they are measured on every node, and an interpolation isn't considered. This shouldn't present a problem since one normally speaks in terms of diameters, which are greater then the resolution used in the models, which is around 5 mm.

What has just been described clearly means that the rod is now taking more load, what can be more clearly seen in Figure 3.7. This figure shows how the percentage of the load taken by the reinforcement increases to about 47 %, a much larger value than the highest obtained when the screw was modeled as an unidimensional beam element. A comparison between this and the first two models can also be shown in this figure. The solutions obtained lies between the two models already discussed, namely the two-dimensional orthotropic with a beam element to represent the inner reinforcement and the three-dimensional one with the same way of modeling the reinforcement.

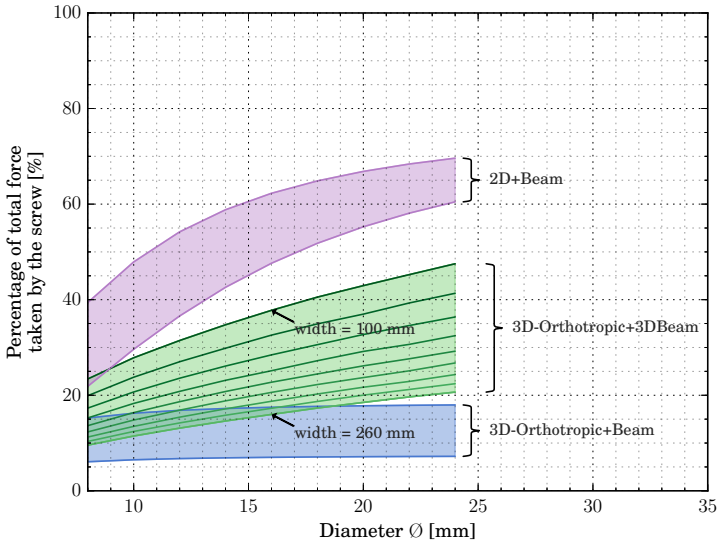

Figure 3.7: *Percentage of force taken by the steel reinforcement for different configurations of widths and rod diameters, for a 3-D orthotropic model with a 3-D modeled reinforcement*

3.5 3-D cylindric-anisotropic model of glulam timber with 3-D Elements to represent the inner reinforcement

3.5.1 Model description

Finally, a three-dimensional cylindric-anisotropic model of the glulam element was created with a 3-D model of the reinforcement (see Figure 3.7). Each lamination has a thickness of h_ℓ=33 mm, having a total of 14 laminations with the positions of the piths —determined by the variables e and d— the same as the ones shown in Figure 1.4, i.e. three different configurations are analyzed here. The position of the rod/screw is kept constant.

The mechanical properties used follow the relation 3.1, which was taken from [2]. The values of the elastic constants can be seen in Table 3.3. The nodes along the perimeter of the reinforcements are coupled to the nodes of the wood in those positions, but not along the upper and bottom faces of it. This means that the stresses can only be transmitted through the curved periphery of the rod/screw. This holds true for the previous model as well.

$$E_r : E_\ell : E_t : G_{\ell r} : G_{rt} : G_{\ell t} = 1 : 10.8 : 0.67 : 0.67 : 0.042 : 0.67 \tag{3.1}$$

Table 3.3: *Mechanical properties used for the cylindric-anisotropic model of the glulam element*

Glulam		
E_ℓ	13694	N/mm^2
E_r	1268	N/mm^2
E_t	849	N/mm^2
$G_{\ell r}$	849	N/mm^2
G_{rt}	53	N/mm^2
$G_{\ell t}$	849	N/mm^2
$\nu_{\ell r}$	0.015	–
ν_{rt}	0.35	–
$\nu_{\ell t}$	0.015	–

3.5.2 Results

The results obtained with this model are very interesting, since they are in some ways, different from the others. Figure 3.6 shows again the same two configurations that were exemplary presented for the other three models, for the configuration *k1* described in Figure 1.4. It can be seen how the vertical stresses no longer form the ellipse-like patterns seen before and concentrate instead along a line in the mid-width of the glulam. This region reaches very high stresses, more than twice the value of the original surface load applied on the top face. Looking at the distributions it can be deduced that the force taken by the reinforcement should be fairly large, since it is located exactly within the zone of maximum stresses. The influence radius, previously defined as 80 % of the surface load applied, now has little meaning, since the stresses now reach much higher values, as has just been observed.

Figure 3.10 shows again the percentage of force carried by the screw for each combination of width and diameter, and further compares it, with the results from the other models. It can be clearly seen that the region overlaps the upper-area of the 3-D orthotropic model with the 3-D rod and the lower-zone of the 2-D model. It can be seen then for example, that for

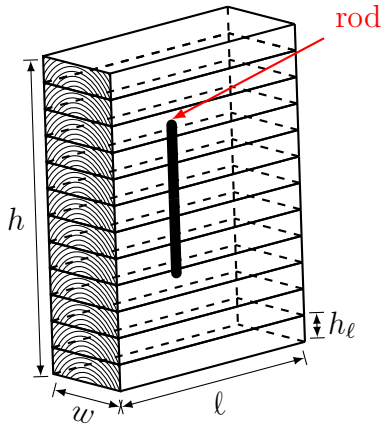

Figure 3.8: *Example of the model used to investigate the influence of the radial anisotropy. The actual model has a total of 14 laminations.*

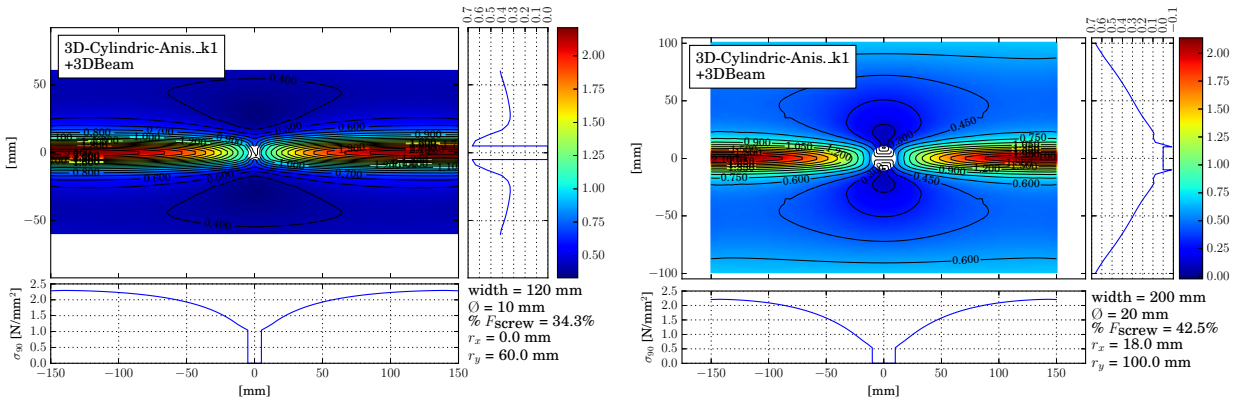

Figure 3.9: *Distribution of stresses perpendicular to grain for the cylindric-anisotropic model, for two different configurations of width and diameter of rod. (a) width equals 120 mm and reinforcement Ø is 10 mm; (b) width equals 200 mm and reinforcement Ø is 20 mm*

w=100 mm and Ø=16 mm approximately a 10 % difference should be expected compared to a two-dimensional model.

The position of the screw will also have an impact on this. If, instead of one rod of cross section A in the mid-width, two of cross sections $A/2$ placed at thirds along the width were used, then the total force taken by this new configuration would probably be lower than the one taken by the former. This is something that should be kept in mind when designing this elements, since it could help to maximize the use of each reinforcement.

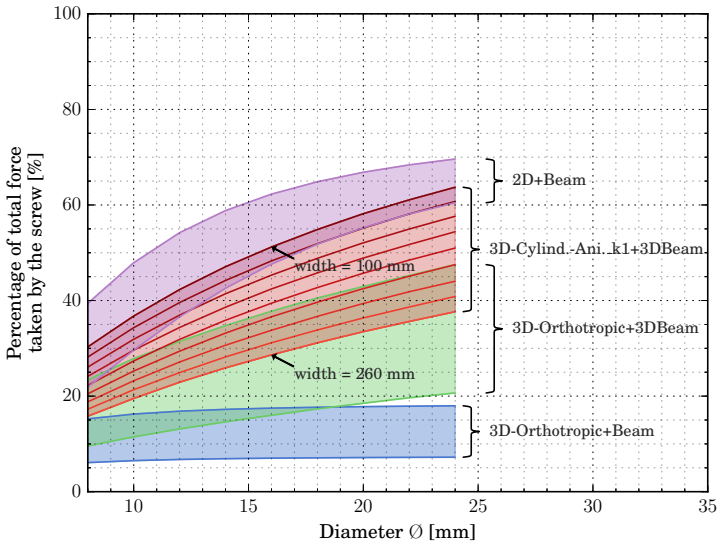

Figure 3.10: *Percentage of force taken by the reinforcement in a cylindric-anisotropic model, with the reinforcement modeled with 3-D elements. The other models are shown for comparison*

There is one more comparison that should be made, namely between the different configurations used in this model (*k1, k2* and *k3*), previously defined in Figure 1.4 in Section 1.1.3. Figure 3.11 shows the percentage of force taken by the internal reinforcement for these three cases. It can be seen that all three lay-ups show very similar behaviors, practically giving the same results. It can also be noted that, although the differences are small, the *k1*-alternative requires the rod to carry a bit more force than the other lay-ups. The explanation for this, regarding the *k3*-configuration, is straight-forward, since, as it was discussed, the position of the reinforcement no longer lies exactly there where the stresses achieve their maximum (the concentration of σ_y observed on Figure 3.9a), since they are now displaced. Hence, the rod can't take as much force as in the other case. Regarding the lay-up *k2* it can be said that a smaller value of d requires the rod to carry less force. However, these effects can be safely disregarded, at least as long as the values for e remain small.

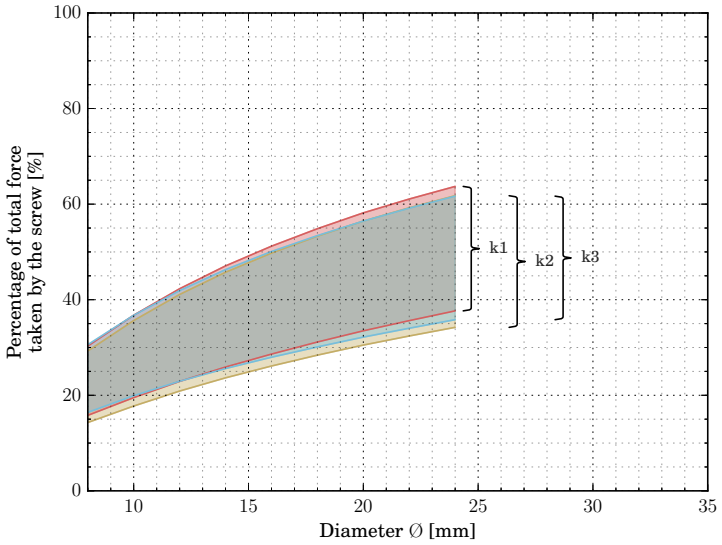

Figure 3.11: *Comparison of the percentage of force taken by the reinforcement for the different laminations build-up configurations k_1, k_2 and k_3 defined in Figure 1.4 for the cylindric-anisotropic model*

3.6 Modeling an internal reinforcement in the vicinity of a hole in a glulam

Considering the previous results regarding the influence of the internal reinforcement in a tension-dominated situation for different FE-models, it is clear that a radial anisotropy is the best option to represent the interaction of the glulam beam and the steel rod. This is so at least for the models studied (see Figure 3.10). Following this, a radial anisotropic model of the glulam beam was created to better understand the interaction of the reinforcement and the shear stresses on the crack-initiation zone.

3.6.1 Model description

A FE-Model of a glulam beam with a hole and internal reinforcements was created applying the submodeling technique, which can be easily handled by ANSYS. The submodelling technique was adopted, since the number of elements needed to represent each lamination with radial anisotropy in a good way is very large, and would therefore need too much computation time. Figure 3.12 shows the submodel created, where the screw and the timber can be identified for their different colors.

The model was created using the same 3-D solid elements as previously for the box-type volume model 3DCylindric+3DBeam. The same thickness for each lamination of 33 mm is chosen as well. A total distance of 300 mm from the hole's edge to the rightmost side is modeled. The height of the beam is 450 mm and the width is 120 mm. Symmetry is applied vertically along the longitudinal direction, which further reduces the amount of elements used. A 3-Dimensional reinforcement is modeled in the mid-width of the beam at a distance of 36 mm from its center to the edge of the hole. The border conditions are taken from a 3-D orthotropic model of a simply supported beam, like the one shown in Figure 6.3, with a total span of 3150 mm and a total load of 400 N applied vertically at mid-span. The full model has a hole of the same geometry and in the same position, only the meshing is coarser. The location of the maximum stresses perpendicular to grain at the hole periphery is obtained from this coarse model, which is used then on the submodel to create an horizontal layer of nodes at this height. This helps to obtain results exactly where they are needed.

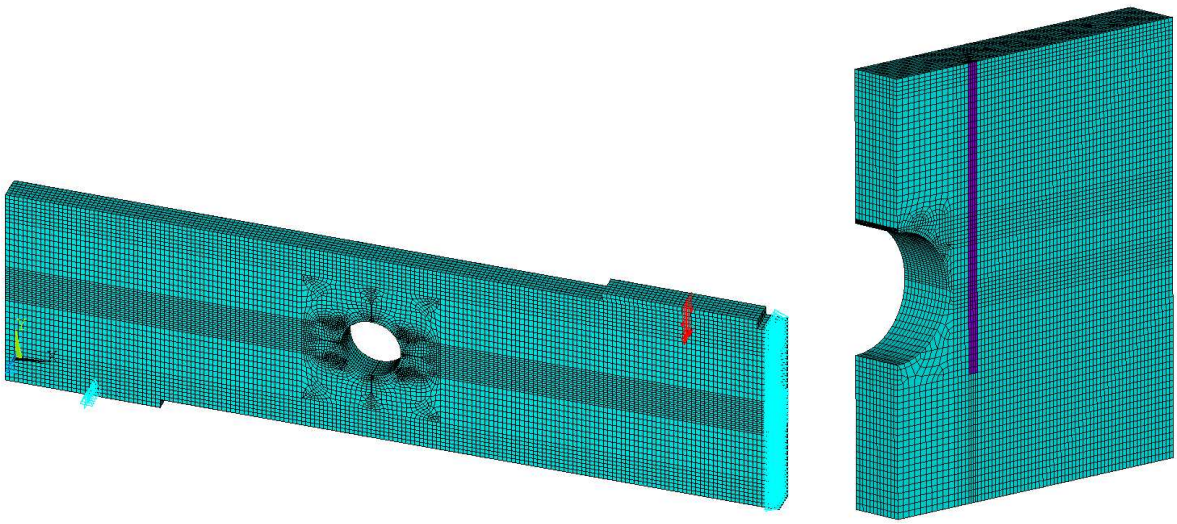

(a) ***(b)***

Figure 3.12: *Figure (a) is the coarse model used to assign the border conditions to the Submodel (Figure (b)) created to represent the anisotropy of each lamination of the glulam beam and the influence of the internal reinforcement along the crack-initiation zone*

3.6.2 Results

The model was run a total of two times, one with the internal reinforcements and the other without them. In this way a comparison of the two material/construction configurations is possible and the influence of the reinforcement can be clearly seen. The results at the horizontal surface that lies at the location of the maximum vertical stresses are presented in Figure 3.13. The red surfaces indicate the stresses when the model has an internal reinforcement and the blue areas depict the stresses in absence of them.

Figure 3.13a shows the influence of a rod-like reinforcement on the stresses perpendicular to grain. The red areas indicate the stress distribution in presence of the reinforcement, whilst the blue areas show the stress distribution in absence of it. It can be clearly seen that there is a slight reduction in the maximum stresses on the corner and that by moving towards the rod this reduction becomes more relevant, as it would be to expect. Crossing to the other side of the reinforcement, coming from the highest stressed hole periphery, there is almost a complete absence of vertical stresses, which means that the rod has effectively taken the stresses formerly present in this zone.

In Figure 3.13b the effect of the internal reinforcement on the shear stresses along the same aforementioned surface is depicted. From this Figure it is clear that the influence that a rod-like reinforcement has in the control of the shear stresses is practically zero. Only a very small reduction is observed directly on the corner, but from there on the stresses remain unchanged.

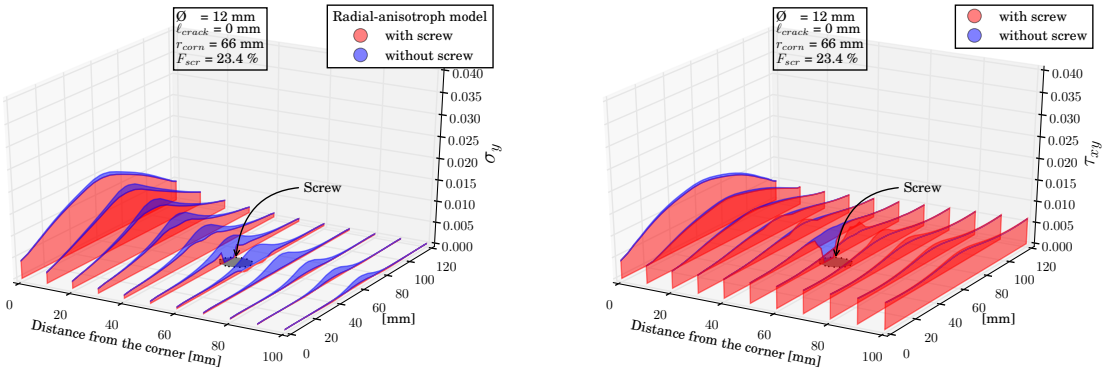

Figure 3.13: *The figures show the stresses along the horizontal surface located at the same height as the maximal vertical stresses at the hole periphery. Figure (a) shows a comparison of the vertical stresses in the presence and absence of internal reinforcements; Figure (b) shows a comparison of the shear stresses under the two situations as well.*

3.7 Discussion

3.7.1 Influence of the model

In this chapter four different ways of modeling the interaction of an internal reinforcement and a glulam element were performed. The 2-D model gave the highest values for the load taken by the reinforcement in the mid-height of the box-type wood volume. The 3-D orthotropic model, with beam-elements describing the steel rod, gave the lowest results for this force. These two models present the same problem regarding the way the reinforcement is modeled, since the plane/solid elements used for describing the wood can't take into account the *volume* of the reinforcement. The 2-D model further completely ignores the fact that it can't possibly act along the whole width. Thus mixing beam elements with plane or solid ones in this way does not represent a proper mechanical approximation of the real situation.

The 3-D orthotropic model, with the reinforcement modeled as three-dimensional solid elements, gave results located between the previous two models. These results seem reasonable but it is interesting to compare them with the cylindric-anisotropic model. This one reaches values higher than the ones in the *3D+3DBeam*-model but smaller than the 2-D model. Although it is clear that a cylindrical-anisotropic representation is more realistic, it is also important to note that it highly depends on the lay-up of each lamination in the zone of interest. It has been shown that, for certain typical lay-ups, the vertical stresses will concentrate mainly in the mid-width zone of the glulam (see Figure 3.9), making the reinforcement more effective if placed in that area. If the value of d gets bigger, i.e. the curvature of each year-ring gets smaller, the model will then become very similar to the orthotropic one. Since the *3D+3DBeam*-model gives smaller values for the force taken by the rod (lying on the safer side) and considering the difficulties of creating cylindric-anisotropic models, it seems that the 3-D orthotropic model with 3-D representation of the reinforcement is the most efficient solution for this problem.

Regardless of the conclusions just made about the more complex cylindrical model, it is important to take note of some of the things that could be seen in that model, such as the influence of the position of the reinforcement linked to the zone of higher stresses in the middle. Even though one could use the *3D+3DBeam*-model to calculate the force $F_{t,90}$, the position of the internal reinforcement will influence the amount of this force that the rod will carry, and it is important to have this in mind even if we are on the safe side.

3.7.2 Shear stresses control with internal reinforcements

From the results obtained it is evident that internal reinforcements are not well suited to reduce the shear stresses present along the highest stressed hole periphery in the zone of crack initiation. This is due to the relatively low stiffness that they posses in the direction of the shear stresses.

Chapter 4

Design of holes acc. to EN-1995-1-1/NA

Holes in glulam beams are the source of stress concentrations that affect the regions near the height stressed hole periphery. The nature of this stresses was described in Section 2.1, where it was stated that the tensile stresses are the ones that need to be more carefully observed, since they act in the weakest direction of the material. The redistribution of stresses generates a vertical force in the crack-plane, presenting a critical area which must be checked during design. The capacity of a given beam to resist such force for a specific kind of hole or hole-array is essential in the design of these elements.

In this chapter the design of unreinforced holes acc. to DIN EN 1995-1-1/NA [18] is described, starting from the basic concepts to the use of the design equations. Subsequently, the different types of reinforcements allowed by the Standard are introduced, and the procedure to dimension them is explained. Finally a discussion of different aspects of the Standard is made, which will give an insight into the next chapter.

4.1 Unreinforced holes

4.1.1 Basic concepts

According to DIN EN 1995-1-1/NA [18], holes in beams are defined as apertures with dimension $d \geq 50\,mm$ (see Figure 4.1). They may be rounded or rectangular shapes, and be placed in series of multiple holes as long as the minimal distance, ℓ_Z, is ensured (Table 4.1). In rectangular holes, rounded corners are needed in order to avoid extreme stress concentrations that arise as a result of the singularity present. These concepts are explained with more detail below.

Hole shapes

In the German national annex of the EC5, only two different hole shapes are allowed, which are circular and rectangular ones. The former are described entirely by one value, its diameter Ø, which is equal to the parameters a, h_d and d shown in Figure 4.1 and is limited, for unreinforced holes, to a value of $0.15h$. Rectangular holes can have different width to height ratios, a/h_d, as long as the conditions $a \leq 0.4h$ and $h_\mathrm{d} \leq 0.15h$ are satisfied. These holes have another parameter, namely the corner radius, which helps to reduce the stress concentrations at the corners of the hole. According to the DIN EN 1995-1-1/NA [18] this radius must be at least of 15 mm. From the production point of view this is not a problem, since the machine used to make the holes (CNC) has a rotating tip, which creates the rounded corners with ease. Any other geometrical form, like a triangle or trapezium, is not inherently approved and would need a special approval to be built.

Arrays of holes

Multiple holes in a single beam are also allowed, but only when placed one next to the other at a minimum separation of $\ell_Z \geq 1.5h$, yet not closer than 300 mm. Placing holes one above the other is not permitted. It is also not allowed to put multiple holes next to each other, even when the area comprising the holes and solid section in between are considered as one large hole and would satisfy the conditions for a hole explained above.

There is no problem in mixing different kinds of shapes when placing multiple holes in a beam, as long as the minimum distance is assured.

Minimum and maximum values

There are a couple of values, other than the ones just described, that need to be taken into account. The first one is the distance from the upper or bottom face of the beam to the hole's edge, $h_\mathrm{ro(ru)}$, which must be equal to or larger than $0.35h$. This comes from the fact that at smaller distances the stresses parallel to grain between the hole and the upper/bottom faces begin to distribute in a highly non-linear way [3]. Another value that needs to be taken care of is the distance from the nearest beam's end grain face to the corresponding edge of the hole, ℓ_V, which cannot be smaller than the height of the beam, h. This accounts for the amount of horizontal surface present to oppose the shear stresses that make the crack propagate. Finally, the distance between the center of the nearest support and the hole's edge (closer to that support), ℓ_A, needs to be greater than $h/2$ in order to avoid stress concentrations that may be in the region surrounding the support. All these values, as well as the ones mentioned before, are summarized in Table 4.1.

Table 4.1: *Minimum and maximum values for different parameters in the design of unreinforced holes acc. to DIN EN 1995-1-1/NA [18]*

$\ell_V \geq$	h	
$\ell_Z \geq$	$\begin{cases} 1.5 \cdot h, \\ 300\,\text{mm}, \end{cases}$	$\begin{cases} \text{if } h \geq 200\,\text{mm} \\ \text{otherwise} \end{cases}$
$\ell_A \geq$	$\frac{h}{2}$	
$h_{\text{ro(ru)}} \geq$	$0.35 \cdot h$	
$a \leq$	$0.4 \cdot h$ (for rectangular holes)	
$h_{\text{d}} \leq$	$0.15 \cdot h$	

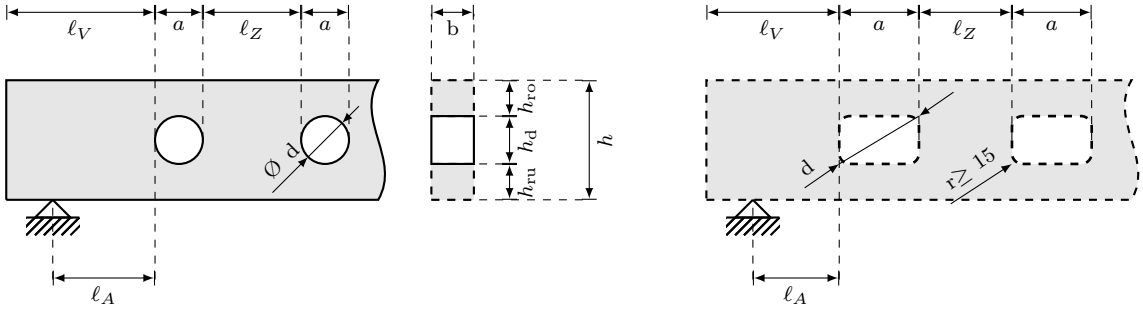

Figure 4.1: *Parameters used for the design of unreinforced holes in glulam and LVL beams*

Limitations

Due to the relatively small maximum sizes that unreinforced holes are allowed to have ($h_{\text{d}} \leq 0.15h$), they are not practical to use in many scenarios. One of the major reasons to restrict the maximum size of an unreinforced hole to 00.15h as compared to 00.3h in the former German timber design code DIN 1052 [10] is in order to avoid the possibly superimposed stresses due to extreme climate changes.

4.1.2 Design equations

The DIN EN 1995-1-1/NA [18] is based on a strength of materials design approach, where the main idea is to compare the design force $F_{t,90,\text{d}}$ against the force of an assumed triangular strength-distribution with the maximum value equal to a constant design tension strength perpendicular to grain, $f_{t,90,\text{d}}$, as shown in Figure 4.2. The design strength is calculated as a function of the characteristic strength value $f_{t,90,k}$, given a reference volume of 10 liters [4], and the pertinent modification factors specified in the Standard (see Eq. 4.1). The modification factor, k_{mod}, takes into account the climate condition (in form of the service class) and the accumulated time of load duration, and γ_M is a partial safety factor for the material, whose recommended value for glulam beams is equal to 1.25 [17]. The actual design

verification is shown in Eq. 4.2. The term $k_{t,90}$ is a size-effect factor that has the form showed in Equation 4.3.

$$f_{t,90,\mathrm{d}} = \frac{f_{t,90,k} \cdot k_{\mathrm{mod}}}{\gamma_M} \tag{4.1}$$

$$\frac{F_{t,90,\mathrm{d}}}{0.5 \cdot \ell_{t,90} \cdot b \cdot k_{t,90} \cdot f_{t,90,\mathrm{d}}} \leq 1 \tag{4.2}$$

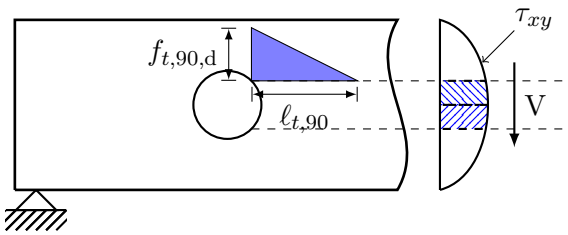

, and force equilibrium model

Figure 4.2: *Graph to explain the values $f_{t,90,\mathrm{d}}$ and $\ell_{t,90}$*

$$k_{t,90} = \min\left\{1; (450/h)^{0.5}\right\}, \quad \text{with } h \text{ in mm} \tag{4.3}$$

$$\ell_{t,90} = \begin{cases} 0.5 \cdot (h_{\mathrm{d}} + h) & \text{,if hole is rectangular} \\ 0.353 \cdot h_{\mathrm{d}} + 0.5 \cdot h & \text{,if hole is circular} \end{cases} \tag{4.4}$$

In order to evaluate Eq. 4.2 the force $F_{t,90,\mathrm{d}}$ needs to be determined. In the Standard this value is composed of two terms related to the internal forces (see Eq. 4.5), one accounting for the effects of the moment on the region of the beam where the hole is placed, and the other one to include the impact of the shear force in the same place. These two terms are defined in the next subsections.

$$F_{t,90,\mathrm{d}} = F_{t,M,\mathrm{d}} + F_{t,V,\mathrm{d}} \tag{4.5}$$

Moment effect

The effect of the moment on the vertical force $F_{t,90,\mathrm{d}}$ relates to the horizontal stresses, σ_x, present in the beam at the same height as the hole. These stresses need to be redirected around the zone of the aperture, which leads to vertical stresses. Equation 4.6 was derived semi-empirically by Kolb and Epple [24] and is used in the Standard.

$$F_{t,M,\mathrm{d}} = 0.008 \cdot \frac{M_{\mathrm{d}}}{h_r}, \tag{4.6}$$

where h_r is defined as

$$h_r = \begin{cases} \min\left(h_{\mathrm{ro}}; h_{\mathrm{ru}}\right) & \text{,if hole is rectangular} \\ \min\left(h_{\mathrm{ro}} + 0.15 \cdot h_{\mathrm{d}}; h_{\mathrm{ru}} + 0.15 \cdot h_{\mathrm{d}}\right) & \text{,if hole is circular} \end{cases} \tag{4.7}$$

Shear force effect

In Section 2.2, it was explained how the shear stresses redistribute in the vicinity of the hole, inducing vertical stresses. With this in mind an equation can easily be derived from the force equilibrium model shown in Figure 4.2 [4]. The hatched regions of the figure represent the stresses that need to be redistributed, which makes the derivation of the Eq. 4.8 very transparent and straight-forward.

$$F_{t,V,\mathrm{d}} = \frac{V_{\mathrm{d}} \cdot h_{\mathrm{d}}}{4 \cdot h} \cdot \left[3 - \frac{h_{\mathrm{d}}^2}{h^2}\right] \tag{4.8}$$

In this equation h_{d} may be replaced by $0.7h_{\mathrm{d}}$ when round holes are being used.

4.2 Reinforced holes

4.2.1 Types of reinforcements

If the conditions described for unreinforced holes are not met, then the addition of a reinforcement is mandatory in order to prevent an uncontrolled propagation of the cracks within the zones of tensile stress. Reinforcements are elements placed perpendicular to grain direction that help to improve the resistance of timber structural members when subjected to a condition of traction in that direction. Several kinds of reinforcements are available, which can be divided into two main groups: *(a)* internal reinforcements (rod-like) and *(b)* external reinforcements (plate-like). These two groups are described as follows.

Internal reinforcements

Internal reinforcements are understood as steel rod-like elements placed perpendicular to grain inside a beam in the regions of vertical tensile stresses. Figure 4.3 shows the positioning of these as well as the nomenclature for the dimensions. The different kinds of reinforcements allowed by the Standard to be used are:

- screws with threads along the whole shaft,
- glued in threaded rods and

- glued in concrete steel-rods (rebars).

When using any of these reinforcements DIN EN 1995-1-1/NA [18] needs to be considered. Also the weakened cross section shall be considered in the zone exposed to tensile stresses.

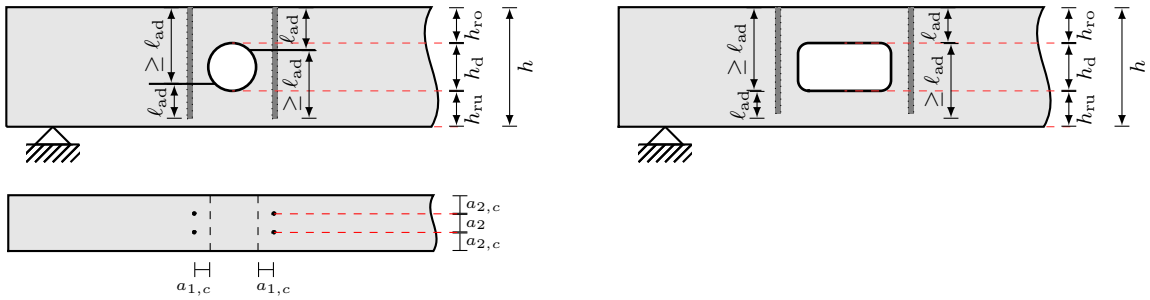

Figure 4.3: *Positioning of internal reinforcements acc. to DIN EN 1995-1-1/NA [18] for circular and rectangular holes*

External reinforcements

External reinforcements are plate-like elements placed on the sides of the beam elements, surrounding the hole area, that help to carry the vertical stresses around the aperture. In the DIN EN 1995-1-1/NA [18] four different types of these elements are allowed:

- glued on plywood panels acc. to DIN EN 13986 [13] combined with DIN EN 636 [19] and DIN 20000-1 [11]
- glued on laminated veneer lumber acc. to DIN EN 14374 [16] or to DIN EN 13986 [13] combined with DIN EN 14279 [15] and DIN 20000-1 [11]. A supervised verification for cases not included in the cited Standards is permissible as well.
- glued on boards
- pressed-in nail plates

Figure 4.4 shows the positioning of these elements for rounded and rectangular holes, and all the geometrical parameters that describe them.

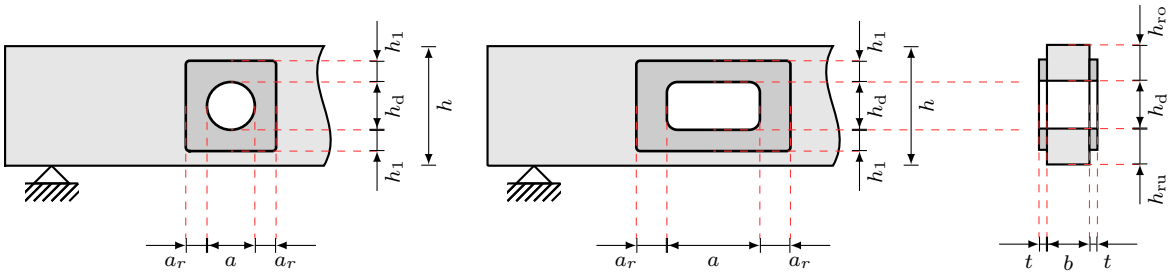

Figure 4.4: *Positioning of external reinforcements acc. to DIN EN 1995-1-1/NA [18] for circular and rectangular holes*

4.2.2 Generalities

The hole shapes allowed for use with the addition of reinforcement are exactly the same as the ones used for the unreinforced holes described earlier. Regarding the use of multiple holes in a single beam the same condition still apply as for the first case. The differences can be seen in the sizes and minimum and maximum values that are now permitted.

Maximum and minimum values

When designing reinforcements for holes, some minimum and maximum values have to be regarded, which differ somewhat from the unreinforced case. The minimum values for the hole-edge distance, ℓ_V, inter-hole separation, ℓ_Z, and distance to the support, ℓ_A, (see Figure 4.1) remain the same as described in the previous case. At the same time, $h_{\mathrm{ro(ru)}}$ is reduced to a value of $0.25h$ (from a previous value of 0.35h). This means that the holes are now allowed to be placed nearer to the top or bottom edges of the beam.

Regarding the size of the hole, it can now have much larger dimensions. The horizontal length, a has now a maximum value equal to h, which is 2.2 times bigger than the unreinforced condition. For the height of the hole, h_{d}, a difference is made between the two types of reinforcements; For the internal reinforcements the height is limited to $0.3h$, while for the externally reinforced ones it goes up to $0.4h$. The difference is based on the evidence of high non-linear distribution of bending stresses at the hole's edge [3], where plate-like reinforcements are assumed to help carrying them, while internal reinforcements are not capable of taking said stresses. The ratio a/h_{d} is limited to ≤ 2.5. A summary of all these values can be found in Table 4.2.

Table 4.2: *Minimum and maximum values for different parameters in the design of unreinforced holes acc. to DIN EN 1995-1-1/NA [18]*

$\ell_V \geq$	h	
$\ell_Z \geq$	$\begin{cases} 1.5 \cdot h, \\ 300\,\mathrm{mm}, \end{cases}$	$\begin{array}{l} \text{if } h \geq 200\,\mathrm{mm} \\ \text{otherwise} \end{array}$
$\ell_A \geq$	$\dfrac{h}{2}$	
$h_{\mathrm{ro(ru)}} \geq$	$0.25 \cdot h$	
$a \leq$	h	
$a/h_{\mathrm{d}} \leq$	2.5	
$h_{\mathrm{d}} \leq$	$\begin{cases} 0.3 \cdot h, \\ 0.4 \cdot h, \end{cases}$	$\begin{array}{l} \text{for internal reinforcements} \\ \text{for external reinforcements} \end{array}$

4.2.3 Design equations

The design equations for both types of reinforcements are based on the assumption that they carry the whole force $F_{t,90}$, computed with Equations 4.5 to 4.8.

Internal reinforcements

When steel rods are used as reinforcement, the tension at the glueline needs to be verified acc. to Equation 4.9

$$\frac{\tau_{\mathrm{ef,d}}}{f_{\mathrm{k1,d}}} \leq 1 \tag{4.9}$$

, where the term $\tau_{\mathrm{ef,d}}$ is calculated as

$$\tau_{\mathrm{ef,d}} = \frac{F_{t,90,\mathrm{d}}}{n \cdot \mathrm{d}_r \cdot \pi \cdot \ell_{\mathrm{ad}}} \tag{4.10}$$

Here, n is the number of rods used per side, that can only be placed at a distance $a_{1,c}$ from the hole's edge (see Figure 4.3); d_r is the rod's diameter, which must be $\leq 20\,\mathrm{mm}$; $f_{\mathrm{k1,d}}$ is the design value of the strength of the glueline; and ℓ_{ad} is the anchorage length of the rod with respect to the most probable crack surface, and is as

$$\ell_{\mathrm{ad}} = \begin{cases} h_{\mathrm{ro(ru)}} + 0.15 \cdot h_{\mathrm{d}} & \text{if hole is circular} \\ h_{\mathrm{ro(ru)}} & \text{if hole is rectangular} \end{cases} \tag{4.11}$$

In Equation 4.11 the formula is defined for both h_{ru} and h_{ro}, as the cracks may appear as much in the upper half as in the lower half of the hole. Although there is a higher probability that the first crack may occur at the hole position with the higher section forces due to material scatter also the leser stressed hole edge has to be verified.

The minimal length of the rod is restricted to $2\ell_{\mathrm{ad}}$ and the distance of the rod to the edge of the hole, $a_{1,c}$, needs to be in the range $2.5 \cdot \mathrm{d}_r \leq a_{1,c} \leq 4 \cdot \mathrm{d}_r$. Also, when a rectangular hole is present, the shear stresses should be verified within the regions near the corners subjected to tensile stresses. For the latter design, however, DIN EN 1995-1-1/NA [18] does not specify explicit equations (see below).

External reinforcements

For plate reinforcements it is assumed that the stresses along the glueline are evenly distributed, and the (maximum) design shear stress must comply with the following relations.

$$\frac{\tau_{\mathrm{ef,d}}}{f_{\mathrm{k2,d}}} \leq 1 \tag{4.12}$$

$$\tau_{\mathrm{ef,d}} = \frac{F_{t,90,\mathrm{d}}}{2 \cdot a_r \cdot h_{\mathrm{ad}}}, \tag{4.13}$$

where

$$h_{\mathrm{ad}} = \begin{cases} h_1 & \text{for rectangular holes} \\ h_1 + 0.15 \cdot h_{\mathrm{d}} & \text{for circular holes} \end{cases} \tag{4.14}$$

The definitions for the values a_r, h_1 and h_{d} can be seen in Figure 4.4; $f_{\mathrm{k2,d}}$ is the design value of the glue-line strength.

The tensile stresses on the reinforcement plate needs to be verified as follows:

$$k_k \cdot \frac{\sigma_{t,\mathrm{d}}}{f_{t,\mathrm{d}}} \leq 1, \tag{4.15}$$

with

$$\sigma_{t,\mathrm{d}} = \frac{F_{t,90,\mathrm{d}}}{2 \cdot a_r \cdot t_r} \tag{4.16}$$

The value t_r represents the thickness of the reinforcement plate and the factor 2 accounts for the fact that there are plates at both sides. The factor k_k in Equation 4.15 considers the uneven distribution of the stresses. Without further analysis $k_k = 2.0$ can be assumed, i.e. a triangular stress distribution. Quantity $f_{t,\mathrm{d}}$ is the design value of the tensile strength for the reinforcement in the direction of the tensile force $F_{t,90}$.

There are also some minimum and maximum values that need to be regarded for the plate reinforcements, namely the sizes for a_r and h_1 (see Figure 4.4). The first term, a_r, is limited to the range $0.25 \cdot a \leq a_r \leq 0.6 \cdot \ell_{t,90}$, with $\ell_{t,90} = 0.5(h_{\mathrm{d}} + h)$, while $h_1 \geq 0.25 \cdot a$.

4.3 Discussion

4.3.1 Internal or external reinforcements?

When faced with the choice of whether to use internal- or external reinforcements there are some variables that need to be considered. One variable might be economical, which would sway the balance toward the side of the internal reinforcements, due to their relatively low

price in comparison to the plate reinforcements that would suit the same conditions. Internal reinforcements are not only cheap, but they are also very easy to deploy. The time and work needed to insert them depends on the specific kind of internal reinforcements used (screws, glued in rods, etc.), but normally they all can be accurately placed in a short period of time and be ready for immediate use. Plate reinforcements need more time to be ready, since the same hole as the original needs to be perforated and then each plate has to be glued on the sides of the beam, which takes time. At the same time, internal reinforcements are invisible, making them a more aesthetically pleasing option.

On the other hand, external reinforcements are more effective due to their capacity to transfer both the stresses perpendicular to grain and the shear stresses. The latter can not be carried by vertically placed internal reinforcements, thus making them completely unsuited and ineffective at reducing the shear stress peaks on the corners.

In Chapter 3 it was shown, by means of a cylindrically-anisotropic FE-model, that the vertical stresses tend to concentrate at the mid-width of a glulam beam when subjected to vertical stresses. A screw placed at that position would be very efficient in carrying the stresses perpendicular to grain, and for the same reason plate reinforcements might not be as effective, since they are placed in the zones where the vertical stresses are reduced. In summary, internal reinforcements take vertical stresses very efficiently but zero shear stresses, while external reinforcements take vertical stresses less efficiently but can carry shear stresses. The sagacious reader might now well be asking himself, whether it couldn't be possible to use both types of reinforcements in some cases. The answer is that unfortunately, there are no current investigations which address this question; further, this question addresses the well-known issue in timber construction, that mechanical joints (such as screws) in general show non neglectable slip where glued joint are rigid, which leads in a first rough approximation to the design principle that both types of joints show no interaction, i.e. load sharing.

The decision for what reinforcement is to be used has to be made taking these factors into account, considering the specific conditions of each project and always regarding the safety of the structure.

4.3.2 Adequacy of the equations to obtain $F_{t,90,\mathrm{d}}$

Aicher [1] showed that the equation to compute the vertical force $F_{t,90,\mathrm{d}}$ might have some problems, especially in regions of big internal shear force, such as near a support (small ℓ_A). Consequently, some designs could be on the unsafe side and the equations should therefore be corrected. This is what motivates the next chapter, where a set of new equations is derived in order to improve the current ones.

4.3.3 Shear force and internal reinforcements

It was discussed previously how internal reinforcements are not capable of transmitting shear stresses arising in the vicinity of the hole (see Section 3.6). Currently the main consideration

in the Standard when designing reinforcements is the tensile vertical force $F_{t,90,d}$, giving little importance to the shear stresses at the corner [1]. Blaß et al. [8] and Aicher [1] have investigated the influence of the shear stresses and proposed equations to consider these shear stresses in the design. But the actual influence of the shear force on the propagation of the crack has not yet been sufficiently studied. If this shear force is determined to be of relevance, then a possible arrangement of the internal reinforcements would be needed. A good option seems to be the use of diagonally placed screws [6], which would help redistribute the shear stresses in the needed sector. Further research needs to be done, however, in order to answer this question.

Chapter 5

Modification of unreinforced-holes equations

Some evidence has shown that the current design equations for unreinforced holes might not always give safe results [1], in particular the equations for the computation of the tensile force $F_{t,90,\mathrm{d}}$ (see Equations 4.5 to 4.8). These equations were derived considering mainly circular holes, thus not considering all of the effects adequately.

In this chapter an evaluation of the current equations for $F_{t,90,\mathrm{d}}$ acc. to DIN EN 1995-1-1/NA [18] is presented by comparing their results with FE-Models. Later, a new set of equations is derived and their parameters are adjusted to match the computational model. At the end of the chapter a comparison between the two models is made and a discussion based on the results presented is carried out.

5.1 Evaluation of current equations

In the previous chapter the equations for designing beams with apertures were presented. One of the fundamental parts of this approach is to obtain an accurate computation of the vertical force $F_{t,90,\mathrm{d}}$, which will help in the dimensioning of the appropriate reinforcement. Recent investigations [1] have shown a small discrepancy between the Equations 4.6 and 4.8, and the numerical results obtained from FE computations.

In order to get a better insight into the current state of the design equations, two different parametrical FE-Models were created. The first one analyzes the pure-moment case in a beam, whilst the second tries to resemble a typical situation with moment and shear force in the zone of the hole. This distinction is useful since the design equations are separately given in the Standard for both the moment and shear effects. These models are described next.

5.1.1 Description of FE-Model: pure moment

A finite element model was designed to evaluate the accuracy of Equation 4.6, which should give the moment contribution to the tensile force $F_{t,90}$. In order to do this the hole is placed in a region of pure moment as shown in Figure 5.1. The program Ansys V.15 was used to create the model and solve it, while the post-processing of the data was a mixture between Ansys and Python scripts with known scientific libraries [22, 26, 25, 23].

The model is 3D-orthotropic and uses three-dimensional linear elements (SOLID185). Such elements present a total of 8 nodes with three *dof* at each node. The dimensions of the beam are 6000 mm × 450 mm × 120 mm and there are two forces applied at 1000 mm to each side of the middle of the hole, that is located in the center of the beam. Steel plates were modeled on top of the beam at the loading points to redistribute the stresses to the beam and avoid stress concentrations. The same was done at the supports. The dimensions of the steel plates were 350 mm × 50 mm × 120 mm. Contact elements (type CONTA173 and TARGE170) were placed on the top- and bottom faces of the beam at the support and loading areas. This eases the connection with the steel plates, by allowing the nodes of the beam and plates not to necessarily coincide. This is helpful in a parametrical model, due to the change in the distances between the nodes when the position of the hole or loading points varies.

The mechanical properties are the same as the ones listed in Table 3.2 for the glulam beam. The dimension and shape of the hole are parametrized, allowing for circular holes, as well as rectangular ones of different aspect ratios.

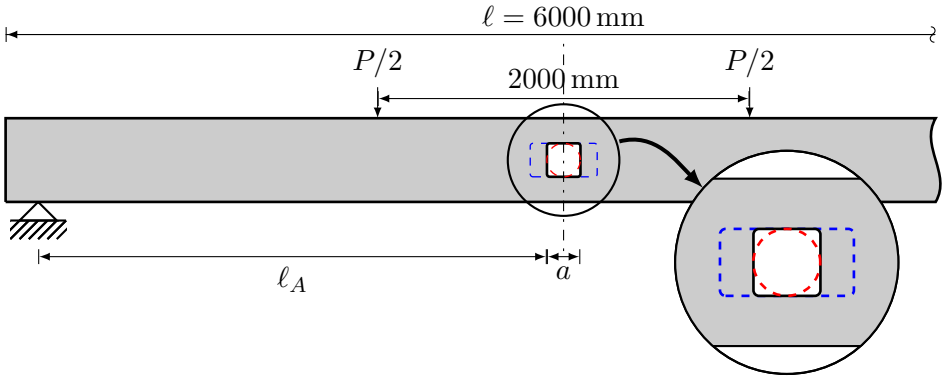

Figure 5.1: *Layout of the FE-Model used to obtain $F_{t,90}$ in a pure-moment condition. The quadrilateral hole is drawn with solid lines, while the circular and rectangular ones are drawn with dashed lines.*

5.1.2 Description of FE-Model: moment and shear

The present model is in essence a modification of the one described prior. The mechanical properties are the same as well as the dimensions of the beam (6000 mm × 450 mm × 120 mm). What changes are the position of the hole and loading point. This model uses only one loading point at mid-length of the beam as shown in Figure 5.2. Besides the dimension and shape

of the hole, the position, ℓ_A, is also considered as a variable. The considerations regarding the contact elements and steel plates are the same. As can be seen in Figure 5.2 the aperture can be placed in different positions, all of which are affected by both moment and shear force. This will help to evaluate the accuracy of Equation 4.8 once the contribution of the moment has been analyzed.

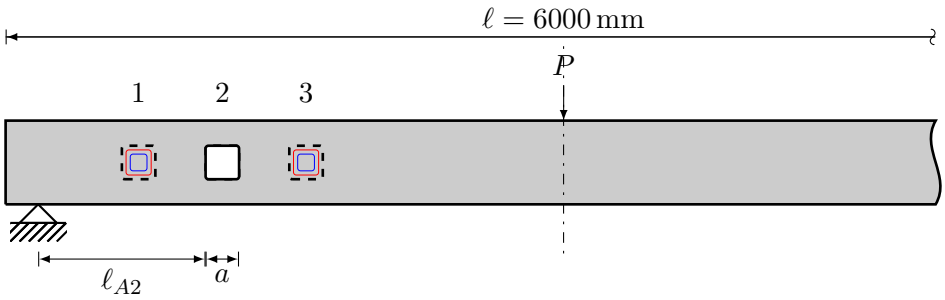

Figure 5.2: *Layout of the FE-Model used to obtain $F_{t,90}$ in a region where both moment and shear force are present. The three different positions analyzed are shown for a quadrilateral hole.*

5.1.3 Procedure

Pure moment

The model is executed for three different holes shapes (round, quadrilateral and rectangular ($a/h_\text{d} = 2.5$)) and for ratios h_d/h within a range between 0.15 to 0.4 in steps of 0.05. After the solution of each model is obtained, the tensile force at the upper-right corner of the hole is computed with an APDL-script. These results are then exported to a file and then processed with a python script. Here the values for the tensile force are calculated using Equation 4.6 and then compared with the ones extracted from the FE-Model. The comparison made is of the form $F_{t,90,\text{FE}}/F_{t,90,\text{Stand.}}$, and should give a better insight into how good both values correlate.

The corner of the rectangular and quadrilateral holes have radii of 15 mm throughout all the configurations. The width of the beam is maintained constant as well, as it shouldn't be relevant for this model.

Shear and moment

The model is executed for the same three different hole shapes, for ratios h_d/h in the range of 0.15 to 0.4 in steps of 0.05. The position of the hole is also varied in terms of the longitude ℓ_A, using three values corresponding to the ratios $\ell_A = h$, $2h$ and $3h$ with $h = 450\,\text{mm}$. The precise values can be seen in Tables 5.1 and 5.2. The same APDL-script as before is used to obtain the tensile force at the upper-right corner. Processing with the python script is carried out in the same way as for the pure moment case.

Table 5.1: *Parameters used in the model to investigate the accuracy of Equation 4.1, for the round and quadrilateral hole shapes.*

shape	round + quadrilateral					
h_d/h	0.15	0.2	0.25	0.3	0.35	0.4
	[mm]	[mm]	[mm]	[mm]	[mm]	[mm]
a	67.5	90	112.5	135	157.5	180
$\ell_{A1}+a$	517.5	540	562.5	585	607.5	630
$\ell_{A2}+a$	967.5	990	1012.5	1035	1057.5	1080
$\ell_{A3}+a$	1417.5	1440	1462.5	1485	1507.5	1530

Table 5.2: *Parameters used in the model to investigate the accuracy of Equation 4.1, for the rectangular hole shape.*

shape	rectangle					
h_d/h	0.15	0.2	0.25	0.3	0.35	0.4
	[mm]	[mm]	[mm]	[mm]	[mm]	[mm]
a	168.75	225	281.25	337.5	393.75	450
$\ell_{A1}+a$	618.75	675	731.25	787.5	843.75	900
$\ell_{A2}+a$	1068.75	1125	1181.25	1237.5	1293.75	1350
$\ell_{A3}+a$	1518.75	1575	1631.25	1687.5	1743.75	1800

5.1.4 Results

The results obtained are illustrated in Figures 5.3a to 5.3d. It can be seen from Figure 5.3d that the tensile force calculated with Equation 4.6 (moment contribution) is extremely conservative in relation to the value computed with the model. The ratio $F_{t,90,\mathrm{FE}}/F_{t,90,\mathrm{Stand.}}$ ranges from 0.1 to 0.5 for h_d/h ratios streching from 0.15 to 0.4 There is a small difference between round, and quadrilateral and rectangular holes, but it is not significant.

Table 5.3: *Values of the tensile force on the upper right corner computed with the FE-Model for the case of shear+moment. For all the cases P=1 kN is used.*

	h_d/h	0.15	0.2	0.25	0.3	0.35	0.4
	ℓ_A/h	[N]	[N]	[N]	[N]	[N]	[N]
○	1	44.1	62.8	77.5	96.3	115.3	134.6
	2	46.9	62.2	80.7	96.4	116.2	135.2
	3	46.2	62.0	77.4	97.6	116.2	135.5
□	1	54.0	76.3	101.6	127.5	153.9	179.1
	2	55.3	79.4	102.6	129.0	156.1	184.0
	3	54.7	77.1	102.7	128.1	156.6	186.1
▭	1	63.0	92.3	124.1	157.3	193.3	231.5
	2	64.7	91.7	123.6	157.8	195.2	234.5
	3	64.0	91.5	123.8	158.6	195.1	235.3

Figures 5.3a to 5.3c show the most typical situation, where moment and shear are present. For the three cases presented (for each hole shape) two common patterns can be observed, namely the increasing ratio $F_{t,90,\mathrm{FE}}/F_{t,90,\mathrm{Norm}}$ with increasing h_d/h and a decreasing value of the same ratio when the distance ℓ_A increases, i.e. when the influence of the moment grows bigger. It can be seen that for holes with $h_d/h \gtrsim 0.3$ and near the support ($\ell_A = 1h$) equation

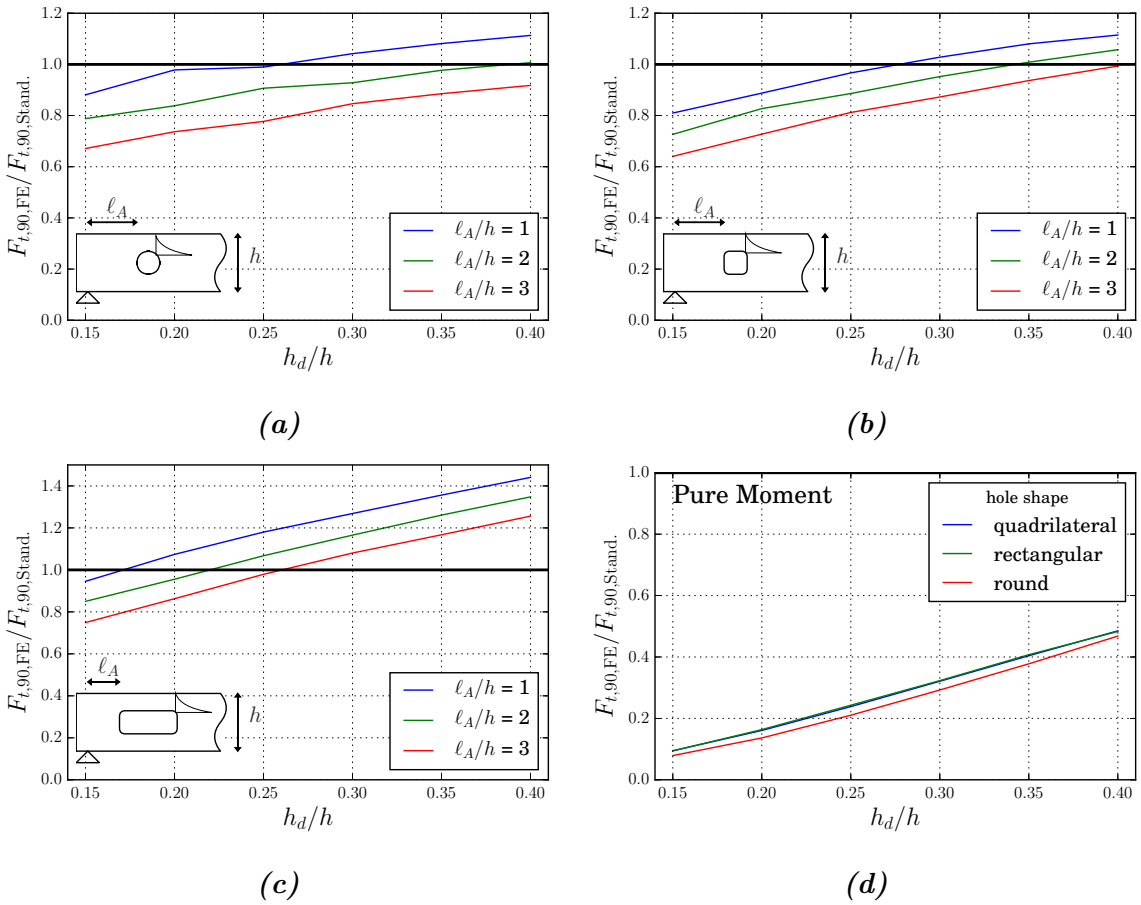

Figure 5.3: *Comparison between the tensile force $F_{t,90}$ computed with the FE-Model and those obtained with the equations from DIN EN 1995-1-1/NA [18]. Figure (a) shows the ratio $F_{t,90,FE}/F_{t,90,Stand.}$ for circular holes of different sizes (h_d/h) and three different distances ℓ_A/h from the near most support; Figure (b) shows the same comparison but for quadrilateral holes with a constant corner radius of 15 mm; Figure (c) presents the mentioned relation for rectangular holes with ratio $a/h_d = 2.5$; Finally Figure (d) depicts the same ratio but for a pure moment configuration and for the three principally different hole shapes.*

Table 5.4: *Values of the tensile force on the upper right corner computed with the FE-Model for the case of pure moment. For all the cases P=1 kN is used.*

h_d/h	0.15	0.2	0.25	0.3	0.35	0.4
shape	[N]	[N]	[N]	[N]	[N]	[N]
○	3.0	5.5	9.1	13.6	18.9	25.3
□	3.6	6.5	10.3	14.9	20.2	26.2
▭	3.6	6.6	10.5	15.0	20.3	26.1

of the Standard begins to be on the unsafe side for circular and quadrilateral holes. For the rectangular hole the solution begins to be on the unsafe side much earlier. The distance ℓ_A for this case doesn't need to be as small as for the other two situations, but it can be observed that distances of $\ell_A \geq 3h$ lie also clearly on the unsafe side.

Tables 5.3 and 5.4 show the values of the tensile forces obtained with the FE-Model for the shear+moment case and pure moment accordingly. Dividing these values by the respective result obtained from Equation 4.1 gives the data shown in Figures 5.3a to 5.3d.

5.1.5 Discussion

It is evident that the results as calculated according to Equation 4.1 are unsafe for several situations, especially in case of rectangular holes. This indicates that the governing equations need to be improved. The shifting observed in the lines corresponding to different distances ℓ_A (see Figures 5.3a to 5.3c) indicates that, in a great part, are probably caused by the inaccuracy of the $F_{t,M,\mathrm{d}}$ equation (pure moment). Since the shear force stays constant for all cases, and the moment varies linearly with ℓ_A, it follows that the only parameter that could affect the results in the observed way is the moment. This means that the pure-moment equation should be reviewed first and then the shear part can be improved. Additionally, as mentioned, since the moment in the region of the hole for a pure-moment configuration is constant while for the other case varies, one might expect a small shifting in the different lines ℓ_A due to the change in moment, ΔM, in the zone where the tensile force is computed (see Figure 5.4). Even when the ratios $F_{t,90,\mathrm{FE}}/F_{t,M,\mathrm{Stand.}}$ (pure moment) match exactly, there might still be a small shifting between the different ℓ_A-lines.

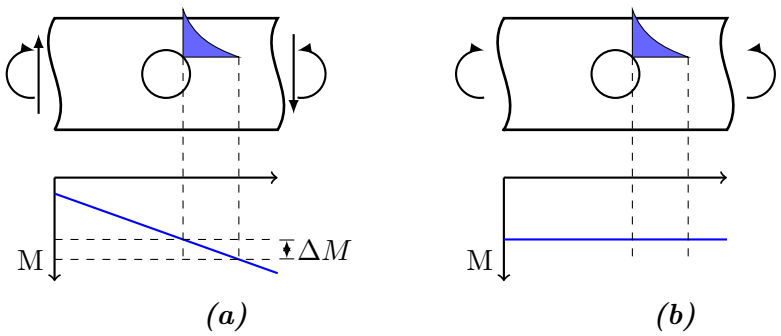

Figure 5.4: *Comparison between moment diagrams for a moment+shear condition (a) and for pure moment (b). Both figures show why shifting between the ℓ_A-lines could still be present, even after the pure-moment equation would work exactly.*

5.2 Deriving an improved set of equations

From the last section it is evident based on the models described here, that there is room for improvements in the design equations. The following attempts to do just that, where the procedure to obtain a set of new equations is described and then presented in a clear form.

The starting point for this task is the same concept used to derive the current equation for $F_{t,V,\mathrm{d}}$, which is depicted in Figure 5.5. The shear component therefore is proportional to half of the area under the shear-stress diagram located at the same height of the hole, which

is the blue area shown in Figure 5.5. Likewise, the component of the tensile force coming from the moment is linked to the area under the σ_x-stress diagram.

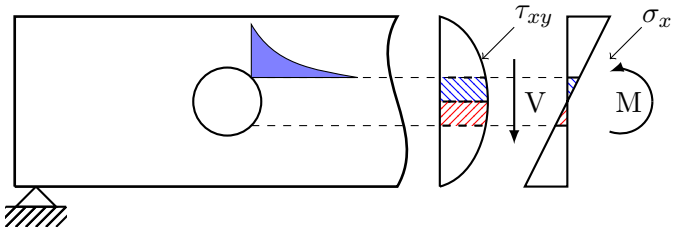

Figure 5.5: *Contribution of the internal forces (shear and moment) to the tensile force* $F_{t,90,\mathrm{d}}$

5.2.1 Procedure

To obtain the improved equations for the tensile force the contribution of the moment must be first calibrated. This is done for each of the three shapes studied so far (circles, quadrilateral and rectangle ($a/h_\mathrm{d} = 2.5$)). Afterwards, the influence of the shear is studied, also separately for each shape type. In this case every shape is positioned at three different distances from the support (ℓ_A), the same as used before. With this data it is then possible to calibrate the parameters that need fine-tuning to obtain results similar to the ones computed with the ANSYS Model.

5.2.2 New equations

Moment contribution

Based on what has been mentioned, a relationship is formulated that includes the effects of the stresses parallel to the grain at a vertical position equal to that at the aperture, as shown in Equation 5.1.

$$F_{t,M,\eta} = \eta \cdot \frac{M_\mathrm{d}}{h} \left(\frac{h_\mathrm{d}}{h}\right)^2, \tag{5.1}$$

where η is a coefficient that needs to be calibrated for each different hole shape. This process is explained later, with Figure 5.7d showing the results after this first calibration.

Shear force contribution

Following the current equation to compute $F_{t,V,\mathrm{d}}$ the Equation 5.2 is proposed as a first attempt to obtain better results. The coefficient ξ needs to first be calibrated in order to judge the appropriateness of such a relationship.

$$F_{t,V,\xi} = \frac{V_\mathrm{d} \cdot \xi \cdot h_\mathrm{d}}{4 \cdot h} \left[3 - \left(\frac{\xi \cdot h_\mathrm{d}}{h} \right)^2 \right] \tag{5.2}$$

The procedure to calibrate the coefficient ξ is explained later, but the best results for the parameter for the quadrilateral and rectangular holes are shown in Figures 5.6a and 5.6b. The values found for these coefficients are $\xi = 1.07$ and $\xi = 1.34$ for quadrilateral and rectangular holes, respectively.

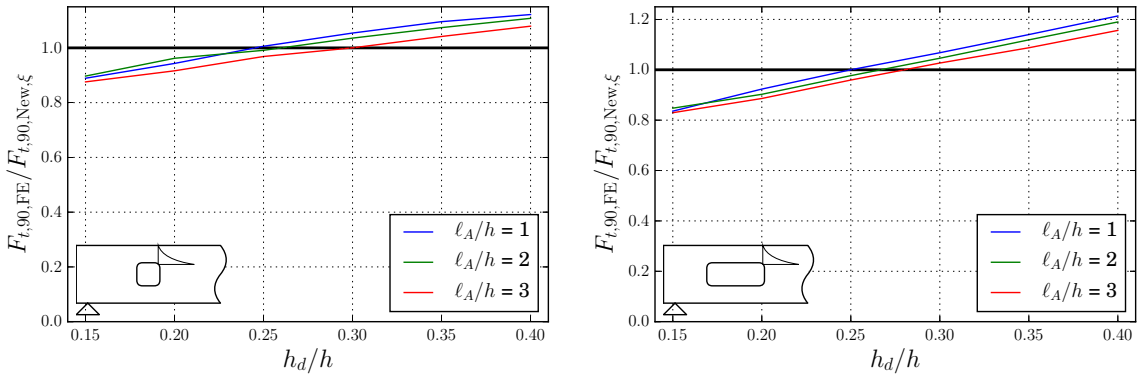

Figure 5.6: *Comparison between the tensile force $F_{t,90}$ computed with the FE-Model and those obtained with the first calibrated equations (5.1 and 5.2). Figure (a) shows the ratio $F_{t,90,FE}/F_{t,90,New}$ for quadrilateral holes of different sizes (h_d/h) and three different distances ℓ_A from the near most support ($\xi = 1.07$); Figure (b) shows the same comparison but for rectangular holes with ratio $a/h_\mathrm{d} = 2.5$, with a constant corner radius of 15 mm ($\xi = 1.34$).*

From these figures, it can be concluded that a linear relation with the ratio h_d/h should be taken into account. The factor chosen to do this is $(1 + \alpha \cdot h_\mathrm{d}/h)$ and further the new equation is the same as 5.2 but now multiplied by said factor.

$$F_{t,V,\alpha} = \frac{V_\mathrm{d} \cdot \xi \cdot h_\mathrm{d}}{4 \cdot h} \left[3 - \left(\frac{\xi \cdot h_\mathrm{d}}{h} \right)^2 \right] \left(1 + \alpha \frac{h_\mathrm{d}}{h} \right) \tag{5.3}$$

In this relation one extra coefficient (α) is introduced, which needs to be determined simultaneously with ξ for each aperture shape.

Determining the coefficients

The method chosen to find the best-fitting parameters is the least square method. It is here preferred for its simplicity and relative ease to include in a program. A Python script was designed to accomplish this task.

As was mentioned before, the first step is to obtain the coefficient η, corresponding to the Equation 5.1 of pure moment. The target function to be minimized is related to the ratio $F_{t,90,\mathrm{FE}}/F_{t,90,\mathrm{New}}$ in the following manner:

$$\text{minimize} \quad f(\eta) = \left| 1 - \frac{F_{t,90,\mathrm{FE}}}{F_{t,M,\eta}} \right| \tag{5.4}$$

This function is then fed with the data of each shape separately, after which the coefficients for η are obtained (see Table 5.5).

The next step is to minimize a similar target function 5.4, subjected to the now determined values of η, which are denoted as η_0. The difference between the two target functions is that the first only incorporates the equation for the tensile force due to the moment, while the second takes into account the tensile force due to the shear force as well. Employing the FE-computed data for the case of shear force and moment, the two remaining parameters can be obtained numerically for each shape. Table 5.5 shows a summary of the three coefficients found for each one of the different hole shapes.

$$\text{minimize} \quad g(\xi, \alpha, \eta = \eta_0) = \left| 1 - \frac{F_{t,90,\mathrm{FE}}}{F_{t,90,\mathrm{New}}} \right| \tag{5.5}$$

where the force $F_{t,90,\mathrm{New}}$ is calculated as

$$F_{t,90,\mathrm{New}} = F_{t,V,\alpha} + F_{t,M,\eta} \tag{5.6}$$

Table 5.5: *Coefficients for the Equations 5.1 and 5.3 found by using the method of the minimum squares.*

Shape	ξ	η	α
○	0.75	0.07	0.3
□	0.82	0.08	1.1
▭	0.87	0.08	1.8

5.2.3 Comparing current equations with new proposed ones

The new derived formulas are compared against the tensile forces computed with the FE-Model. For this the ratio $F_{t,90,\mathrm{FE}}/F_{t,90,\mathrm{New}}$ is used once again, which is calculated for every shape, and also for the two different cases of pure moment and shear force and moment. The results of the results are shown graphically in Figures 5.7a to 5.7d. Here it can be seen that the improved equations with the above obtained coefficients present very good correlations.

For the pure moment case shown in Figure 5.7d it can be noted that the solutions for the quadrilateral and rectangular holes lie very close to that obtained with the FE-Model and have a neglectable slope. On the other hand, looking at the graphical results for round holes one can clearly identify a positive slope, causing the curve to grow for bigger ratios h_d/h. However, even though this behavior is not optimal, the results obtained are still much better than those obtained with the current equations (see Figure 5.3d).

For the cases where shear force and moment are present, the following can be noticed: There is a very small vertical shifting of the force ratio to size ratio relationship results for different ratios ℓ_A/h for all types of holes analyzed. This shifting shows a very specific pattern where the results with smaller ℓ_A/h ratios lie higher than the ones with lower ℓ_A/h ratios. For round holes this shifting is more evident than for the other two shapes, where the separation between the results is smaller. Other than this, the solutions obtained for the three shapes can be classified as very accurate. There is no evident slope to any of the curves, which means that the term introduced before, $(1 + \alpha \cdot h_\mathrm{d}/h)$, was able to solve the problem.

5.3 Discussion

In this chapter the state of the current design equations was shown by comparing it to a parametrical finite-element model. According to what was observed the equations specified in DIN EN 1995-1-1/NA [18] can either give a very conservative solution when looking only at the effects of the moment, or an unsafe solution for specific values of the ratio h_d/h and shape of the hole. Specifically, for round or quadrilateral apertures in shear dominated zones, the solution appears to be on the unsafe side; for rectangular apertures the results obtained are very troubling, having up to 40 % error for ratios of $h_\mathrm{d}/h = 0.4$.

The new derived equations have been shown to be capable of reflecting the value of the tensile force in a more accurate way for a wide spectrum of situations. The use of differentiated coefficients for each hole shape plays a large role in the success of the proposed equations.

5.3.1 Coefficients

It is interesting to realize that the values obtained for the coefficients ξ are very similar to the ones that were already proposed. For example, DIN EN 1995-1-1/NA [18] recommends to multiply the dimension h_d by a factor of 0.7 when the hole is circular. This is very close to the value $\xi = 0.75$, obtained for round holes. The origin of this coefficient stems from the fact that the crack will initiate at an angle of about 45 °, which means that only a fraction of the area under the stress diagram (see Figure 5.5) delivers a contribution to the $F_{t,90}$-integration. This fraction of the area is what ξ represents (in relation to h_d). The term α accounts for the fact that for different ratios of h_d/h the angle ϕ (see Figure 5.9a) of crack initiation slightly varies —according to the maximum vertical stress obtained from the FE-

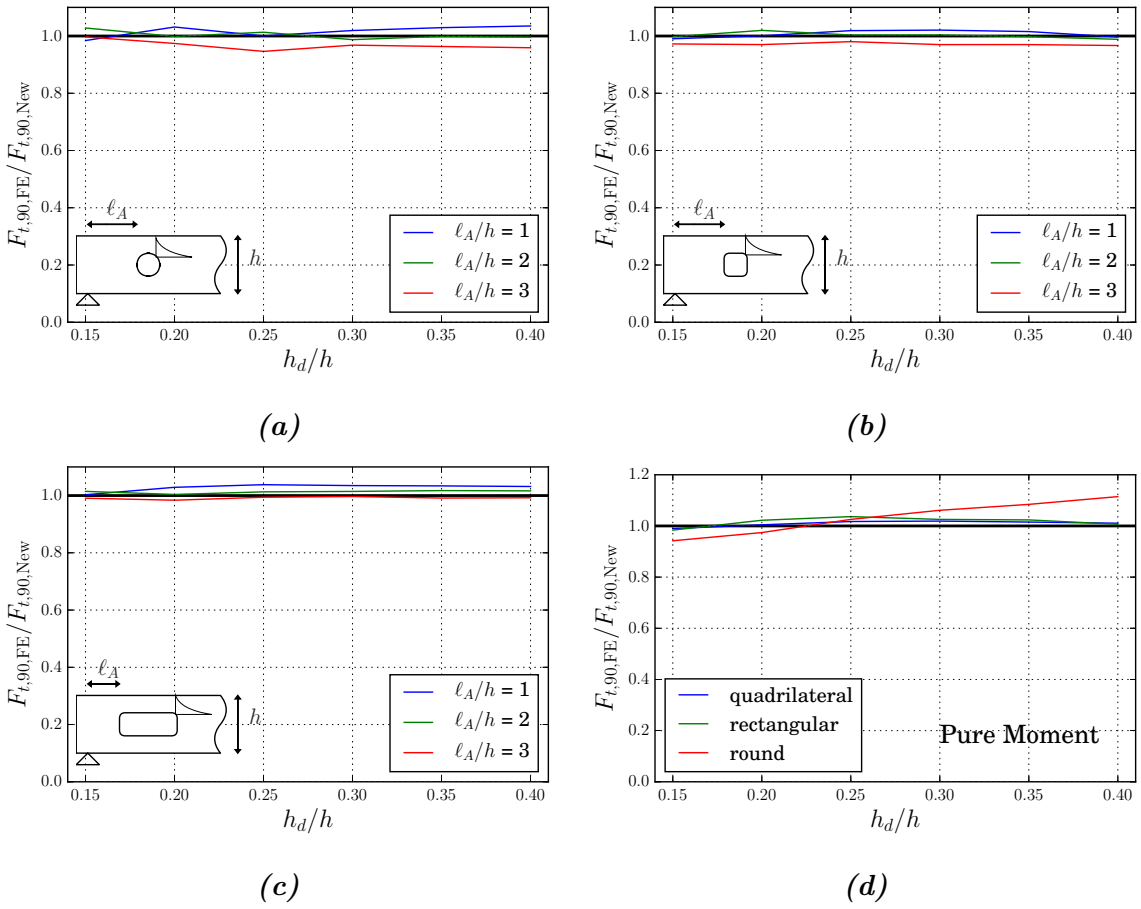

Figure 5.7: *Comparison between the tensile force $F_{t,90}$ computed with the FE-Model and those obtained with the new derived equations. Figure (a) shows the ratio $F_{t,90,FE}/F_{t,90,New}$ for circular holes of different sizes (h_d/h) and three different distances from the near most support, ℓ_A; Figure (b) shows the same comparison but for quadrilateral holes with a constant corner radius of 15 mm; Figure (c) presents the mentioned relation for rectangular holes with ratio $a/h_\mathrm{d} = 2.5$; Finally Figure (d) depicts the same ratio but for a pure moment configuration and for the different hole-shapes.*

Model— and hence this shift in the maximum value needs some correction. The necessary adjustment is in the case of circular holes very small. So, as the correction mainly applies to rectangular and quadrilateral holes the adjustment α could be interpreted as a stress concentration factor explained below in more detail. For the quadrilateral and rectangular cases the two coefficients, α and ξ, have the same meaning as for the round apertures. In the current design equations for quadratic and rectangular holes a value of $\xi = 1$ is implicitly used. For the cases studied the holes have a corner radius of 15 mm, and roughly speaking, since the crack initiates at an angle close to 45 ° from the vertical, the fraction represented by ξ would have the form $\xi = 1 - 2x/h_\mathrm{d}$, where x is the distance from the crack initiation to the top-edge of the hole (see Figure 5.9a). Considering that the analysis was performed for ratios h_d/h raging from 0.15 to 0.4, and looking at Figure 5.8, which shows the influence of each coefficient in the solution, one could then try to determine what value of ξ should theoretically correspond to the lowest h_d/h-ratio, which is 0.15. The value for h_d is then calculated for

the mentioned ratio, obtaining $h_d = 67.5\,\text{mm}$ (using $h = 450\,\text{mm}$). The coefficient ξ for this case is obtained from $1 - 2 \cdot 4.4/67.5$[1], which gives a value of 0.87. This is exactly the value found in the optimization for the studied rectangular case.

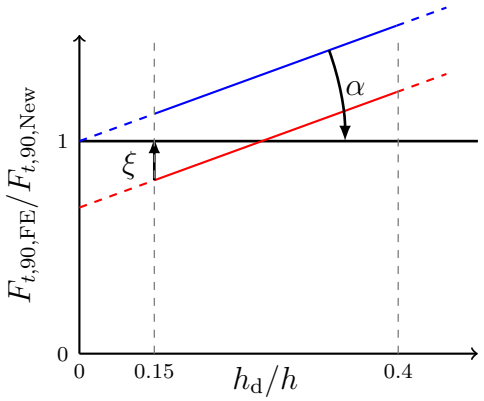

Figure 5.8: *Influence of each coefficient in the solution starting from the point shown in Figure 5.6*

The fact that the corner radius represents a constant dimension introduces a size relationship in the computations (see Figure 5.9b), regarding both a change of the h_d/h ratios, as shown above, and an increase of the absolute value of h (the latter would not occur if the corner radius would be specified proportional to h). Having the above in mind, it is obvious that for larger beam-heights the corner radius will have a progressively smaller impact on the value of ξ, pushing ξ closer to unity. A safe and conservative coefficient to use would then be precisely that, i.e. $\xi = 1$. It is assumed that the value of α should probably work rather well for other beam sizes h, since α per definition compensates for the relative size of the geometries of the hole and beam (h_d/h), delivering a higher stress concentration situation for increasing h_d/h ratios (due to $r = \text{const.}$).

Note: The coefficient η is very similar to the one given in DIN EN 1995-1-1/NA [18], but here it has a totally different meaning, since the terms of the equations are different. Hence, a comparison between these coefficients has no meaning.

5.3.2 Applicability

Due to time limitations not every possible aspect of this problem could be addressed in this thesis, which, in a certain way, limits the applicability of the equations here described. Some of these aspects relate to the position of the hole and the corner radius. The width of the beam, which was here held constant, should not have a great influence however, since the model used was orthotropic. Of course, the same analysis could be carried out with a cylindrical-anisotropic model, where the width of the beam might probably have some influence.

[1]The value 4.4 comes from $15 \cdot (1 - \sin 45°)$

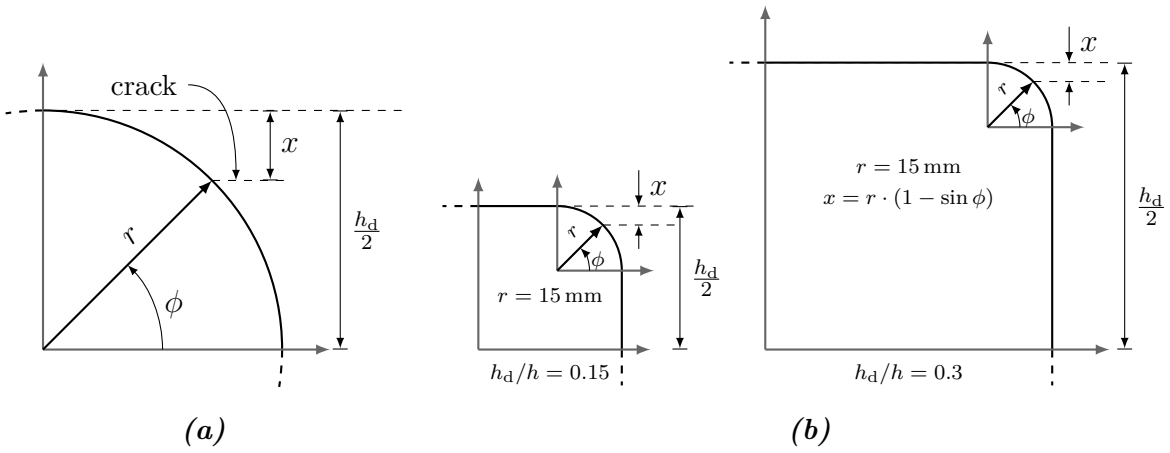

Figure 5.9: *Description of parameters to identify location of crack initiation (factor ξ) for different hole shapes (round (a) as well as quadrilateral and rectangular (b)), and visualization of size effect due to the use of a constant radius at the corner (b). All figures show a quarter of the hole.*

Position of the hole

The different configurations studied here consider always the hole placed in the mid-height of the beam. This is of course a limitation, since in a typical real-life project the aperture could be vertically shifted from the vertical center. Extending the new derived formulas to these cases should be possible, but further investigations and FE-Models would need to be created in order to obtain a more general solution.

Corner radius

The corner radius used throughout all the simulations was 15 mm, which is the minimum accepted acc. to the DIN EN 1995-1-1/NA [18]. Since smaller radii tend to produce larger stress concentrations, it is expected that these results will be on the safe side if a bigger radius is chosen for a rectangular hole.

Chapter 6

Test results

Several experimental series were carried out on glulam beams with different hole shapes to investigate the effectiveness of distinct reinforcement configurations. These series were tested at the Material Testing Institute, University of Stuttgart, over a period spanning from 2001 to 2014, and can be classified into two principal groups, namely internal and external reinforcements. The first test series took place between 2001 and 2008 [5, 20] and consisted mainly of glulams with round holes with different configurations of internal reinforcements; the second group was tested in 2011 [7] and includes different shapes of holes as well as a variety of reinforcement configurations. Experiments were also carried out especially for this thesis, which consists of a series of three glulam beams made of Chilean radiata pine, with round holes and internal reinforcements.

In this chapter the relevant data corresponding to every test series are presented and compared against each other to gain a better insight into each reinforcement's behavior. The data are also compared against the finite element model used in Chapter 5 in order to validate the results obtained from it.

6.1 Test program

6.1.1 General and materials

Spruce glulams with extarnal reinforcements

The reported experimental investigation was carried out on a total of 16 medium sized glulam members with round, quadrilateral and rectangular holes. Out of those, a total of 8 holes had a circular shape, 4 had a quadrilateral one ($a = h_\mathrm{d}$) and 4 holes had a rectangular shape. All of them had a ratio of $h_\mathrm{d}/h = 0.4$. The aspect ratio of the rectangular holes is $a/h_\mathrm{d} = 2$, where a = length of hole parallel to beam axis and h_d = depth of hole perpendicular to beam axis. The corners of the quadrilateral and rectangular holes were manufactured with a fillet radius of 15 mm, the smallest permissible value according to [18]. The diameter of

the circular holes was $\emptyset = 180\,\text{mm}$ throughout. All glulam beams had the same dimensions. The width and the depth of the beams were 120 mm and 450 mm, respectively, and the span and the total beam length were 3150 mm and 3500 mm.

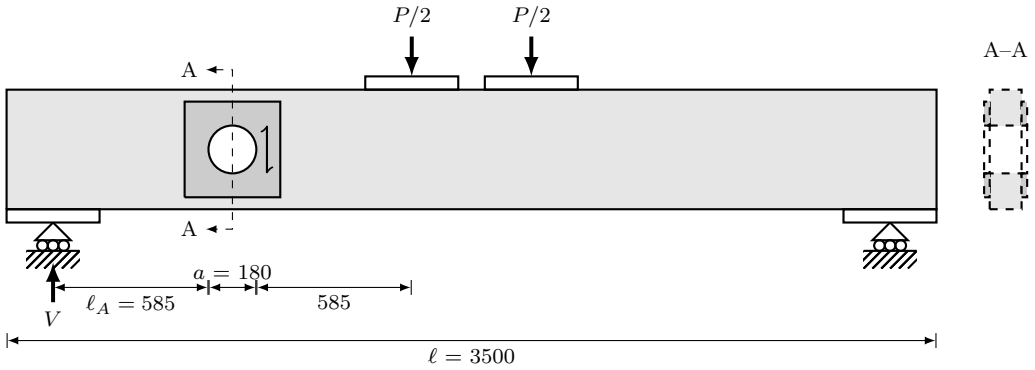

Figure 6.1: *Dimensions, notations and test scheme of investigated reinforced specimens with round and quadrilateral holes.*

The quadrilateral and circular holes are placed at the same position, that is, exactly at the midpoint between the vertical reaction force V of the left support and the leftmost acting force $P/2$, as can be seen in Figure 6.1. This configuration was chosen to minimize the effects that those zones of stress concentrations —reaction and acting force points— could induce on the vicinity of the hole. For the rectangular holes some changes must be made in order to preserve the same distances between the reaction force of the left support and the leftmost acting force; the later has to be moved 180 mm to the right (see Figure 6.2). By doing this, the influence of these two points should be the same for the whole series of tests: round, quadrilateral and rectangular.

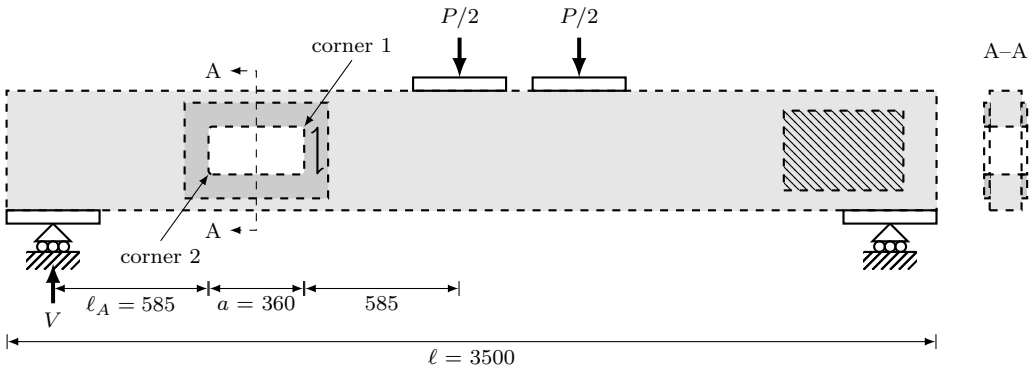

Figure 6.2: *Dimensions, notations and test scheme of investigated reinforced specimens with rectangular holes. For the unreinforced specimen No. 13 all dimensions except for the reinforcement panels apply, too.*

Two beams were selected as reference specimens. Beam No. 9 serves as reference for the quadrilateral holes and beam No. 13 for the rectangular ones. Both of these were tested without any reinforcement. Except for these reference specimens just mentioned, all the openings were reinforced laterally and symmetrically by plywood panels of different dimensions and/or plywood species and strength classes. The thickness of the panels was throughout 21 mm, except for specimen No. 1, where the thickness was 15 mm. Two types

of plywood were used. One type was a rather typical 7-layer spruce plywood, and the other one was birch plywood with 15 layers.

Table 6.1 contains a compilation of the essential material and geometrical configurations of the beam specimens. The relevant material properties of the panels, as specified by the producer, are given in Table 6.2.

Table 6.1: *Material specifications for the panel reinforcements and dimensions (see Figure 4.4) of investigated specimens with rectangular holes.*

Specimen No. and hole shape		wood species of plywood reinforcement	strength (F) and MOE (E) class of plywood	dimensions of reinforcement panels					dimensions of holes		
				t_r [mm]	a_r [mm]	h_r [mm]	L_r [mm]	H_r [mm]	a [mm]	h_d [mm]	a/h_d [–]
1	○	spruce	F20/15 : E40/25	15	150	123	480	426	180	180	1
2	○	spruce	F20/15 : E40/25	21	150	123	480	426	180	180	1
3	○	spruce	F20/15 : E40/25	21	150	123	480	426	180	180	1
4	○	spruce	F20/15 : E40/25	21	90	90	360	360	180	180	1
5	○	spruce	F20/15 : E40/25	21	45	45	270	270	180	180	1
6	○	birch	F40/30 : E70/50	21	45	45	270	270	180	180	1
7	○	birch	F40/30 : E70/50	21	150	123	480	426	180	180	1
8	○	birch	F40/30 : E70/50	21	90	90	360	360	180	180	1
9[1]	□	–		–	–	–	–	–	180	180	1
10	□	spruce	F20/15 : E40/25	21	45	45	270	270	180	180	1
11	□	spruce	F20/15 : E40/25	21	90	90	360	360	180	180	1
12	□	birch	F40/30 : E70/50	21	90	90	360	360	180	180	1
13[1]	▭	–		–	–	–	–	–	360	180	2
14	▭	spruce	F20/15 : E40/25	21	45	45	450	270	360	180	2
15	▭	spruce	F20/15 : E40/25	21	90	90	540	360	360	180	2
16	▭	birch	F40/30 : E70/50	21	90	90	540	360	360	180	2

1: reference specimen without reinforcement

The glulam beams were built-up homogeneously of machine graded spruce laminations, conforming to strength class C35 (5%-quantile bending strength value $f_{m,k} = 35\,\mathrm{MPa}$), resulting in glulam beam strength class GL32h acc. to DIN EN 1194 [12] and DIN 1052 [10]. The characteristic strength and stiffness values of GL32h as specified in the mentioned standards are given in Table 6.2.

The strong panel axis, i.e. the fiber direction of the outermost veneers of the plywood reinforcement is oriented perpendicular to the beam axis (see Figure 6.2). The reinforcement panels are glued on the beams by means of so-called screw gluing as described in DIN 1052 [10]. The dimensions of the employed partially threaded screws, conforming to German general building approval Z-9.1-453 [28] are $4.0\,\mathrm{mm} \times 70\,\mathrm{mm}$. A deviation from DIN 1052 [10], a considerably more dense screwing pattern with maximum edge distances and spacings of about 25 mm and 45 mm, respectively, was used [1]. The given dimensions result in an influence/press area of about $20\,\mathrm{cm}^2$ per screw in order to ensure a high quality bond line strength. The adhesive used for the bonding was a two component melamine-urea formaldehyde (MUF) adhesive (type BASF Kauramin 683 with hardener 686) applied to both sides with an amount of $600\,\mathrm{g/m}^2$.

Table 6.2: *Material properties of plywood reinforcement panels and of glulam*

Characteristic strength or stiffness property (in case of plywood all properites refer to in-plane loading)		plywood species and strength (F), stiffness (E) class[1]		glulam species and strength class	
		spruce F20/15 E40/25 N/mm^2	birch F40/30 E70/50 N/mm^2	spruce GL32h DIN 1052:2008 and EN 1194 N/mm^2	radiata GL25h DIN EN 14080 N/mm^2
bending strength	$f_{m,0,k}$	8	29	32	25
	$f_{m,90,k}$	7	31	32	25
tension strength	$f_{t,0,k}$	16	39	22,5	20.6
	$f_{t,90,k}$	14	36	0.5	0.5
compression strength	$f_{c,0,k}$	16	27	29	25.7
	$f_{c,90,k}$	14	25	3.3	2.5
shear strength	$f_{v,0}$	3.5	9.5	2.5[2]	3.5
	$f_{v,90}$	3.5	9.5	2.5[2]	1.2
modulus of elasticity	$E_{t,c,0}$	6400	9100	13700	16170
	$E_{t,c,90}$	5600	8400	460	300
shear modulus	G	350	620	850	650

1: all values except for in-plane bending ($f_{m,0,k}$, $f_{m,90,k}$) acc. to Technical data sheets for WISA spruce and WISA birch plywood of producer UPM-Kymmene Wood Oy. The values for in-plane bending are taken from DIN 1052:2008 [10], Tab. F.11 and F.12
2: acc. to EN 1194 [12]: $f_v = f_{v,0} = f_{v,90} = 3.8$ MPa; DIN 1052 [10] value includes a crack factor of 0.7

Radiata Pine with internal reinforcements

This test series is carried out on a total of 3 medium sized glulam members with round holes. Out of those, two are provided with internal reinforcements, whilst the third serves as a control specimen. All glulam beams have the same dimensions, which are exactly the same as the spruce beams. The width and the depth of the beams are 120 mm and 450 mm, respectively, and the span and the total beam length are 3150 mm and 3500 mm. All of the apertures have a diameter of $\varnothing = 135$ mm, corresponding to a ratio $h_\mathrm{d}/h = 0.3$, which is the biggest ratio allowed acc. to DIN EN 1995-1-1/NA [18] when internal reinforcements are to be used.

The glulam beams are built-up homogeneously of Radiata pine laminations conforming to strength class T-15 (5%-quantile tensile strength value $f_{t,0,\ell,k} = 15$ MPa), resulting in glulam beam strength class GL25h acc. to DIN EN 14080 [14]. The characteristic strength and stiffness values of GL25h as specified in the mentioned standards are given in Table 6.2. The origin of the Radiata pine wood is the Región del Maule, Chile. The laminations stem from a batch used for the glulam production for the members employed in the construction of the Chile Expo 2015 Pavillion.

The internal reinforcements used are full-threaded Spax-S screws of dimensions $\varnothing$=12 mm and $\ell = 350$ mm, placed at an horizontal distance of 36 mm from the hole's edge. Acc. to Z-9.1-519 [29] the screws have a characteristic tensile strength $R_{t,u,k} = 38\,000$ N and a characteristic fracture torque $M_{t,u,k} = 70\,000$ Nmm.

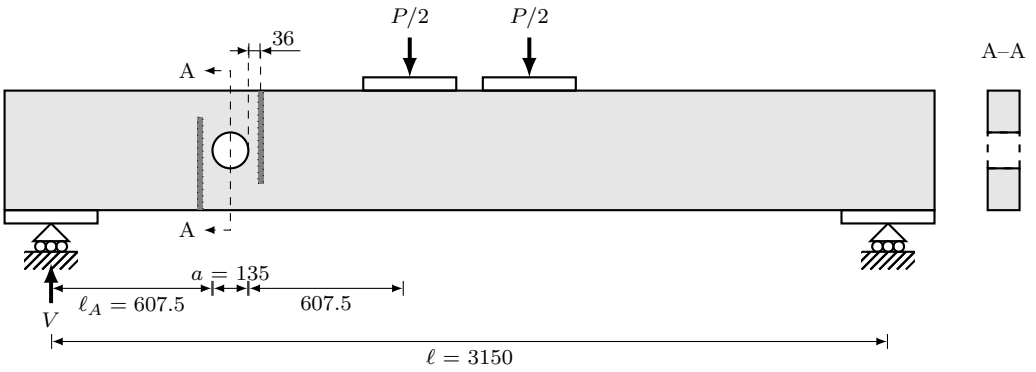

Figure 6.3: *Dimensions, notations and test scheme of investigated reinforced Radiata pine specimens with round holes (all dimensions in mm).*

6.1.2 Specimen instrumentation and test set-up

To verify the calculations and the design model, some of the specimens were equipped with a fairly high number (between 15 and 28) of linear and triaxial planar (rosette) strain gauges. Table 6.3 shows the amount and type of the strain gauges used for the respective specimens. As can be seen, a total of 7 beams out of the 16 spruce glulams were equipped with these sensors, as well as 2 of the 3 Radiata pine beams, being a fairly high number considering the material and application costs. The strain gauges at the surfaces of the glulam and the panel reinforcement were placed symmetrically on both opposite wide sides of the specimens. The linear strain gauges mounted on the narrow sides of the glulam beam were either placed symmetrical vs. mid-width or at mid-width at the end-grain surface of the hole wall. Figure 6.4 shows in an exemplary manner the positions and the numbering of the strain gauges of specimen No. 16; Figure 6.5 shows the placement of the strain gauges on the radiata pine beams. Apart from the strain measurements, the deflection of the beam was measured at mid-span by two displacement transducers (LVDTs) for all the tested beams.

The specimens were loaded in 4-point bending (see Figure 6.1) actually being a quasi 3-point bending scheme. For the rounded and quadrilateral openings the loading was applied symmetrically at mid-span. However, as explained before, this configuration had to be changed for the rectangular holes, requiring the application of load to be somewhat eccentric to mid-span, as it is shown in Figure 6.2 (hence: $V_A = 0.44286 \cdot F$). The reason for this stems from the intention to ensure equal distances of the vertical forces at the loading and reaction point from the relevant hole corners 1 and 2. [1]

6.1.3 Test procedure

The tests were performed with a computer controlled, servo-hydraulic test machine in a heated, but not climatized, laboratory at a temperature of about 19 °C to 21 °C. The wood moisture content of the beams was determined at different locations with a calibrated electric

[1] Longer spans were not considered as the dimensions of all specimens in the test campaign with different holes/reinforcements were chosen identically.

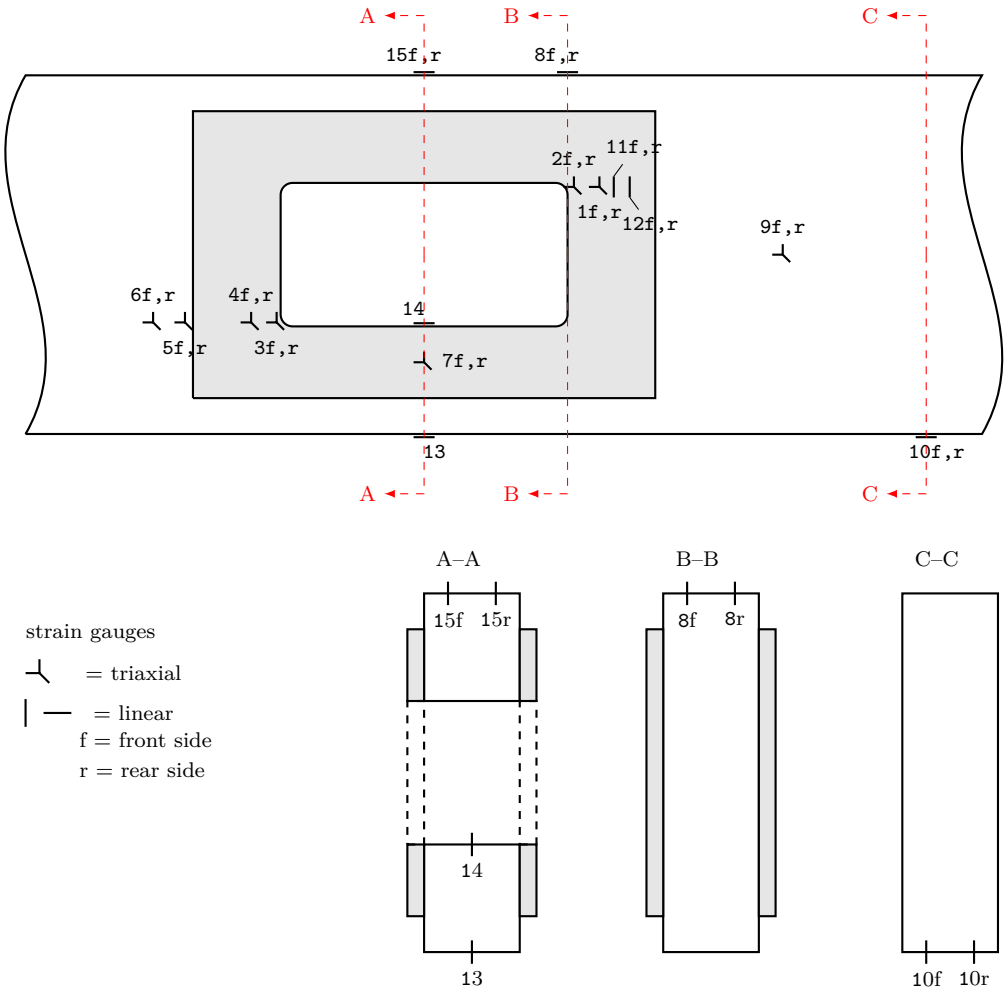

Figure 6.4: *Positions and numbering of the strain gauges at laterally reinforced specimen No. 16.*

Table 6.3: *Total number and type of strain gauges used at the respective specimen. Additionally, the material to which they where attached is specified (glulam or plywood panel).*

Specimen	on glulam		on plywood panel	
	lin*	triax†	lin	triax
4	6	4	8	–
8	6	4	8	–
9	12	8	–	–
12	8	4	8	4
13	16	8	–	–
14	–	7	–	8
16	6	8	10	4
S_1	12	8	–	–
S_2	12	8	–	–

* lin: linear strain gauge
† triax: triaxial strain gauge

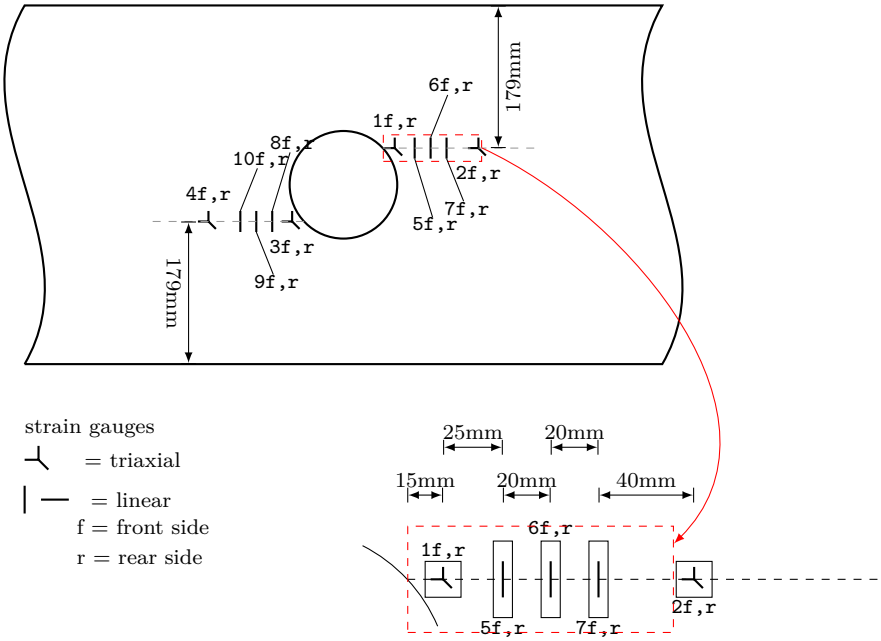

Figure 6.5: *Positions and numbering of the strain gauges at internally reinforced Radiata pine glulam specimens S_1 and S_2*

moisture meter immediately before testing. After completion of the mechanical tests, a full cross-sectional slab was cut from each beam for determination of density and moisture content by the oven drying method.

The loading of the beams was performed displacement controlled at constant stroke rate of 2 mm/min until ultimate failure of the specimen. Special consideration was paid to an exact monitoring of the crack initiation and propagation in the hole areas and its relation to the respective load levels. This monitoring and registration was performed by several staff members at both beam sides whereby in each case one person was in charge of one of both

corners 1 and 2 (see Figure 6.2) at one of both beam sides. Since these measurements are made by direct eye inspection while the test is running, there is of course a certain amount of error associated with these results. Nevertheless, they give very good reference values to compare the test results between the different configurations, as the observation bias should be rather similar.

6.2 Test results

6.2.1 Failure description

The specimens were tested as described in the previous section. With these configurations it is expected that high concentration zones of tension stresses perpendicular to the fiber appear at both the bottom leftmost corner of the hole (near the support) as well as the upper rightmost corner (near the load application point). The cracks begin to spread from these zones, more precisely, from the points where the tensile stresses have their largest values. The exact location of said points depend on the geometry of the hole itself and the distribution of the internal forces. In a rough approximation it can be assumed for a circular hole, in a region of dominant shear force, that the cracks will start roughly at 45° and 135° from the vertical axis for the upper rightmost corner and bottom leftmost corner, respectively (see Figure 6.6a).

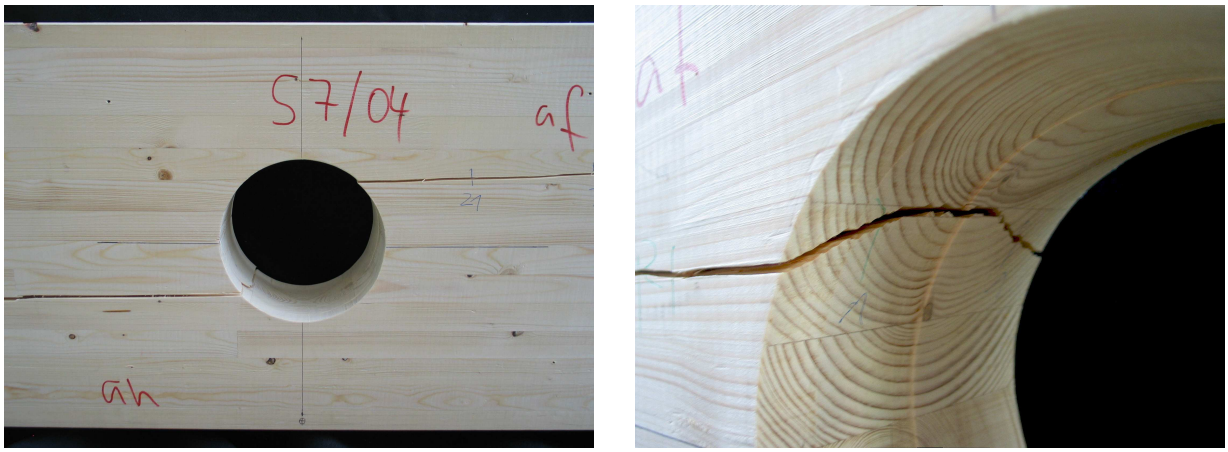

(a) *(b)*

Figure 6.6: *Figures of specimen No. S7/04, taken from a series of experiments carried out at MPA Universität Stuttgart [20]. The propagation of the cracks can clearly be seen along the upper right and bottom left highest stressed areas of the hole periphery. Figure (b) shows a detail of the crack on the upper high stressed area.*

Rectangular holes behave in a similar way, but a higher stress concentration is expected due to the geometric discontinuity present at each corner, despite being diminished by means of a small rounded corner. Therefore, the starting point of the crack is also located at those diagonally opposite corners subjected to tension stresses perpendicular to grain.

The crack will initiate at roughly mid-width of the cross-section as a result of the elevated, anisotropy-bound tensile stresses perpendicular to grain. At further loading the crack spreads to the sides, to later continue spreading in the direction of the fiber and beam axis, which comprise several stages, to be defined later, until the beam reaches brittle global failure. This point can easily be recognized, as the crack starting near the support will then have split the beam entirely. Ultimate failure is further denoted by a very loud crack-sound.

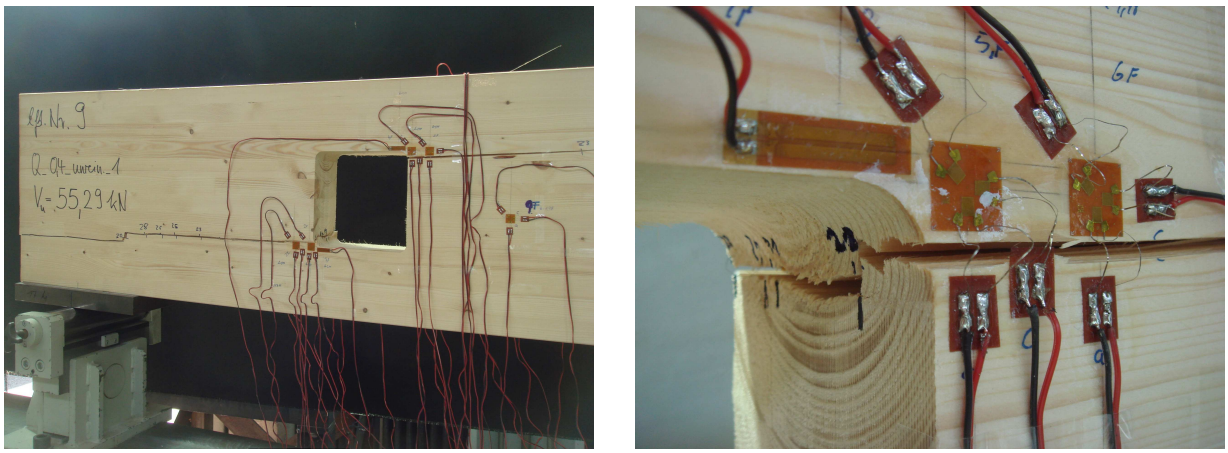

(a) *(b)*

Figure 6.7: *Figures of specimen No. 9 after reaching the ultimate load. The propagation of the cracks can be clearly seen on the upper right and bottom left corners. A non-reinforced specimen is shown, so that the crack paths are more easily visible.*

6.2.2 Ultimate loads and crack stages

During load application, cracks will start spreading from the tensile stress concentration zones. To better understand how these cracks evolve with the internal forces of the beam, different stages have been defined. The ones that are used here are taken from [21] and are described in the following.

Definition of crack stages

The observed stages for each crack during the experiments were:

1. Initial crack is defined as the first crack that is visible at plain sight at each corner. Influenced by the cylindrical stiffness anisotropy present in each lamination, the initial crack usually appears at the center of the cross-sectional width of the beam. The crack formation is difficult to observe at the very beginning, since its location lies normally between early and late wood, whose colors make it hard for the very fine crack to easily stand out.

2. The second stage is defined as the progress of the initial crack along the inner surface of the hole, towards the edges at both sides of the glulam.

3. When the crack has spread along the total glulam width, it has reach the third stage. From this point on the crack begins to spread along the longitudinal direction of the glulam beam, in general along the full cross-sectional width.

4. The crack continues to spread along the wood's fibers until the ultimate load is reached and the beam suffers a global failure.

Definition of important loads

To better describe the whole process of crack-opening it is also helpful to introduce some specific loads expected to mark the beginning or end of different stages during the experiments. These loads are derived from the above-described crack stages, and are likewise taken from [21].

Load at initial crack ($V_{\mathbf{init}}$): this load is represented by the shear force at the instant when the initial crack is first seen. For each aperture there are two of these loads, one for each corner with tensile stress concentration. If no such initial crack is observed before the crack appears along the total glulam width or the beam comes to global failure, then the load at initial crack is defined to be the same as the crack load along the total glulam width or ultimate failure, accordingly. It is also important to note, that the determination of this load during the test is complicated, thus a relatively large error should be expected.

Load at crack along the total glulam width (V_c): this load is defined as the shear force at the instant when the crack has spread along the total cross-sectional width of the beam. For each aperture there are two of these loads, one at corner 1 and the other at corner 2 (see Figure 6.2). If no crack along the full cross-sectional width of the glulam has been observed before the ultimate load is achieved, then the load at crack along the total glulam width is defined as being equal to the ultimate load.

Ultimate load (V_u): the ultimate load represents the highest shear force value that the glulam beam with the aperture can take.

Crack stages

The damage of each glulam beam was monitored as described earlier. With these data it is then possible to determine the load at which each crack stage is reached and then make comparisons between the different reinforcements or hole geometries used. Table 6.4 shows the results for the described crack stages of every test specimen.

The first thing to be noted is that in almost every beam tested, the initial crack first appeared at corner 1, i.e. the top-right one. These results pose the question of whether the

first crack location is purely coincidental or driven by some other factor. To answer this we can look at a large test series carried out by Aicher and Höfflin [20], where this behavior was observed and was linked to the relation M/V present in the glulam beam, in the center of the hole. With small M/V ratios (M/V = 1.5h) both initial cracks tend to appear within a low load level. For larger M/V ratios, for example M/V = 5h, the initial crack at corner 1 tends to appear considerably earlier than the one at the corner diagonally opposite. In this test series the relation M/V is 1.5h, which, as described, should give very similar initial crack loads for both corners.

Table 6.4: *Test results showing the different crack stages of the panel reinforced and reference unreinforced glulam specimens until ultimate failure*

Specimen No.	Reinforcement characteristics				Hole characteristics		Ultimate load	Shear force at crack initiation		Shear force at crack along total glulam width		Shear force at ultimate load
	a_r	h_r	thickness	species	a	h_d	F_u	$V_{init,1}$	$V_{init,2}$	$V_{c,1}$	$V_{c,2}$	V_u
	[mm]	[mm]	[mm]		[mm]	[mm]	[kN]	[kN]	[kN]	[kN]	[kN]	[kN]
1	150	123	15	sp	180	–	213.9	51.3	–			107.0
2	150	123	21	sp	180	–	184.0	32.8	–			92.0
3	150	123	21	sp	180	–	219.5	49.8	–	–	–	109.8
4	90	90	21	sp	180	–	227.2	30.0	64.0	45.5	103.0	113.6
5	45	45	21	sp	180	–	165.0	36.1	42.2	78.4	82.5	82.5
6	45	45	21	bi	180	–	202.4	73.1	76.0	101.2	85.0	101.2
7	150	123	21	bi	180	–	282.0	88.4	114.0	140.6	140.6	140.6
8	90	90	21	bi	180	–	226.6	66.2	86.0	111.4	90.5	113.3
9	–	–	–	–	180	180	106.9	36.1	38.2	41.2	41.1	55.3
10	45	45	21	sp	180	180	143.6	40.0	36.2	67.0	60.0	71.8
11	90	90	21	sp	180	180	165.4	57.4	62.4	82.7	71.4	82.7
12	90	90	21	bi	180	180	213.1	40.0	49.5	106.6	106.6	106.6
13	–	–	–	–	360	180	123.5	14.9	23.5	25.2	24.4	54.7
14	45	45	21	sp	360	180	139.7	15.3	30.1	47.1	46.9	61.9
15	90	90	21	sp	360	180	195.8	25.5	38.5	77.6	53.1	86.7
16	90	90	21	bi	360	180	195.7	32.2	35.0	71.6	59.8	86.7

Corners 1 and 2 as shown in Figure 6.2

The maximal theoretical load that these beams without the presence of holes can bear is 192 kN (see Appendix C). Table 6.4 shows that the panel kind of reinforcement is very effective, provided the sizing of the panel reinforcement was chosen adequately. So for the case of specimens No. 9 and 13, the ultimate load is in the range of 106.9 kN to 123.5 kN, and hence on average 40 % lower as compared to the theoretical capacity. It can be seen from Table 6.4 that for the unreinforced specimens No. 9 and 13, the ultimate load was 55 % and 64 % of the maximal theoretical load, respectively. This is somehow to be expected, due to the already discussed mechanism of failure. What is important to notice are the relatively low load capacities of the specimens 5, 10 and 14, all of which have a spruce reinforcement-plate with dimensions $a_r = h_r = 45$ mm and $t = 21$ mm. These reinforcements fail in restoring the maximal theoretical load capacity to the beams, only achieving between 72 % and 85 % of it, depending on the geometry of the aperture.

Although more data would be needed to know statistically how far below the theoretical capacity such reinforcements can go, these results show clearly that, at least for the spruce reinforcements of the mentioned dimensions, they are not a viable choice to reinforce such elements. Acc. to [18] this is the lowest dimension allowed for this kind of reinforcement

$(0.25\,a \leq a_r \leq 0.6\,\ell_{t,90})$, which means this relation may need to be improved.

Pinus Radiata glulam beams

The results corresponding to the experiments carried out with the Radiata pine are presented in Table 6.5. Due to the smaller hole size present in the Radiata pine glulams ($h_\mathrm{d}/h = 0.3$), in relation to the ones used in the first test series ($h_\mathrm{d}/h = 0.4$), a direct comparison between the results is not possible. However, particular observations regarding the behavior of the internal reinforcements can be made.

Table 6.5: *Test results showing the different crack stages of the Radiata pine glulam until ultimate failure*

Specimen No.	Reinforcement characteristics		Hole characteristics	Ultimate load	Shear force at crack initiation		Shear force at crack along total glulam width		Shear force at ultimate load
	Ø [mm]	ℓ_r [mm]	a [mm]	F_u [kN]	$V_{\mathrm{init},1}$ [kN]	$V_{\mathrm{init},2}$ [kN]	$V_{c,1}$ [kN]	$V_{c,2}$ [kN]	V_u [kN]
S_1	12	350	135	248.1	101.0	101.0	101.0	101.0	124.1
S_2[1]	12	350	135	226.3	89.9	89.9	89.9	89.9	113.2
S_3	–	–	135	182.9	91.5	91.5	91.5	91.5	91.5

Zones 1 and 2 as shown in Figure 6.2
1: specimen S_2 exhibited bending failure

The data contained in Table 6.5 reveal that an internal reinforcement can effectively increase the load required to induce global failure, with increases on average of 30 % for the cases studied. It is interesting as well to note that for the internally reinforced beams, no apparent initial crack was observed on the surface of the hole periphery (on the cross-section), but rather the crack abruptly appeared concurrently at the sides, at both high stressed regions (upper right and bottom left). Although the sample has only very few specimens (1 unreinforced and 2 reinforced ones; hence, no statistical comparison can be made), it can be seen that the internal screw does not seem to have an important influence until the crack has already spread, which is best illustrated by comparing the specimens S_2 and S_3, with and without reinforcement, respectively. In both cases the crack initiation took place practically at the same load, but in the reinforced case the screw was able to stop the crack propagation and delay global failure.

6.2.3 Discussion

Results for different reinforcement and hole configurations have been shown and commented. Since the amount of data presented for holes with internal reinforcements is very limited, results obtained from experiments carried out by Aicher and Höfflin [21] are presented as well (see Table 6.6) in order to expand the existing data base.

Comparing the specimens S_1 and S_2 with the test series V1 of Table 6.6, which have the same reinforcement configuration, several differences can be observed. In the first place,

Table 6.6: *Summary of test-results obtained in [20] for seven series of experiments in glulam beams with different reinforcement configurations.*

Test series	Shear force at crack initiation V_{ini}			Shear force at crack along the total glulam width			Shear force at ultimate load		
	mean val. [kN]	s [kN]	Cov. [%]	mean val. [kN]	s [kN]	Cov. [%]	mean val. [kN]	s [kN]	Cov. [%]
L	36.82	8.78	23.86	46.61	7.56	16.21	62.51	11.86	18.97
V1	44.17	12.51	28.33	63.08	9.08	14.39	85.37	7.97	9.34
V2	44.84	18.98	42.32	64.91	17.14	26.41	92.88	10.35	11.15
V3	38.67	12.45	32.19	56.78	10.84	19.09	87.36	11.53	13.20
V4	40.49	10.43	25.77	52.36	5.00	9.54	99.11	16.24	16.38
V5	31.57	4.14	13.10	45.39	18.13	39.94	83.44	0.37	0.45
R	–	–	–	–	–	–	155.22	29.65	19.10

Table 6.7: *Reinforcements used in every test series shown in Table 6.6*

Test series	reinforcement used
L	–
V1	1× Spax screw Ø=12 mm
V2	2× Spax screws Ø=12 mm (side by side)
V3	1× glued in threaded rod Ø=16 mm
V4	2× glued in threaded rods Ø=12 mm
V5	1× glued in threaded rod Ø=12 mm
R	Reference without hole

the V1-specimens show a crack initiation at the hole periphery on the cross-section, unlike what was observed in the S-specimens. This is probably explained by the difference in the mechanical properties of the two varieties of wood employed. Radiata pine seems to have higher strengths associated with a more brittle behavior.

It is interesting to compare specimens V1 and V2 as well, and to observe that, although V2 has one extra screw to prevent the crack propagation, it does not seem to make a significant difference as compared to V1, which has only one screw. This supports the cylindric-anisotropic model shown in Chapter 3, where the screw clearly would take more load when placed at mid-width of the cross-section. Placing two screws side by side was not modeled explicitly, but it is easy to assume that when no screw is placed directly in the zone of maximum vertical stresses, the efficiency of each would be reduced somewhat.

Series V4 and V5 seem to contradict what has previously been observed. However, looking at the crack initiation load of the series L (unreinforced), where $V_{\text{ini}} = 36.8\,\text{kN}$, it can be noted that the series V5 (1 glued in threaded rod) exhibited crack initiation at 31.6 kN, meaning that the V5 series might have had a particular material weakening. In this way it is confirmed that internal reinforcements don't help prevent the crack initiation.

In looking at the ultimate loads, one can notice that the test series with two internal reinforcements achieved higher values before failure. This is explained by the fact that once the crack has propagated, the internal reinforcements begin to gradually take more load, which means that the use of two rods may certainly add extra carrying capacity and delay a possible global failure.

6.2.4 Comparison with FE-model (model validation)

The results obtained from the strain gauges used in the experiments are compared against a finite element model. This helps establish a connection between the numerical computations previously made and real data obtained from the specimens.

Spruce specimens

The strain data obtained from the experiments were used to create the Figures 6.8a to 6.8c, which show different paths along the surface of the glulam. These paths help to evaluate how good the FE-model correlates with the results of the real beams. The data shown in said figures correspond to the specimen No. 13, which has no reinforcement.

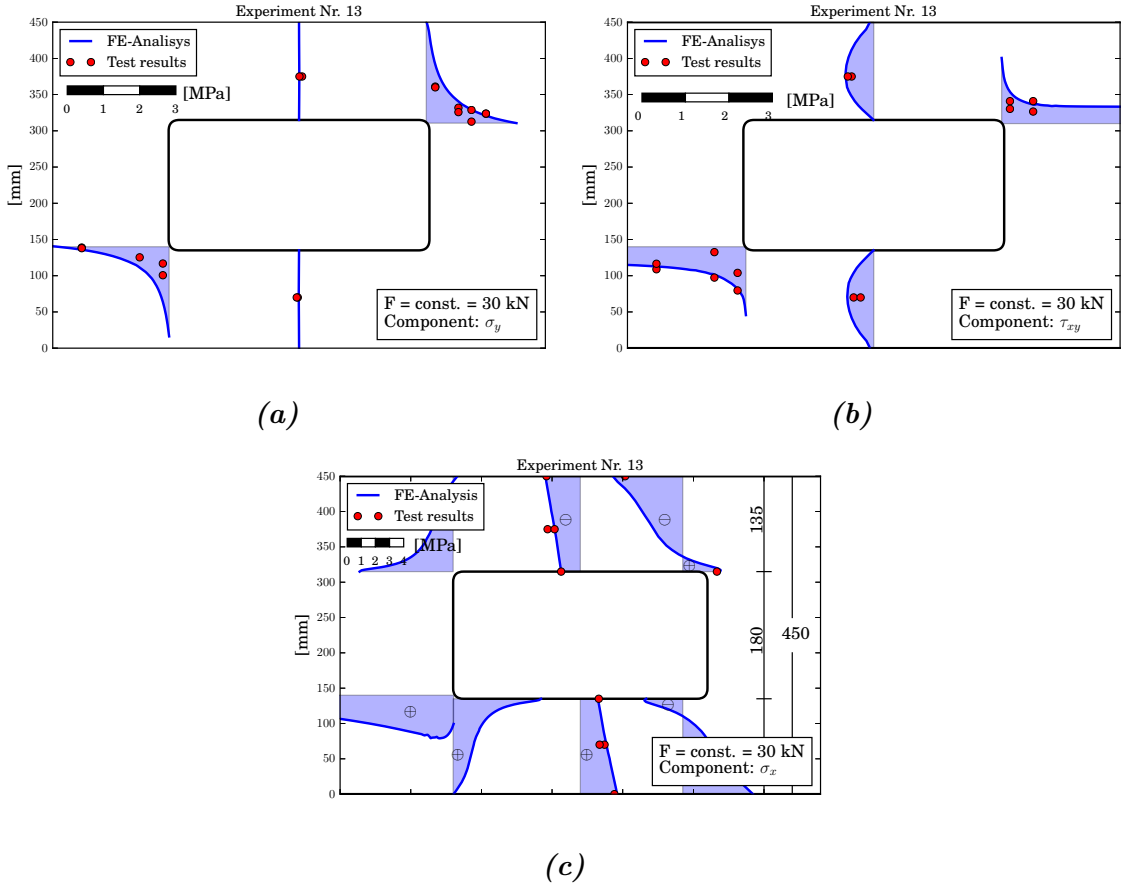

Figure 6.8: *Comparison of the data obtained from the strain gauges and the FE-model, for the Specimen No. 13. (a) and (b) gives stresses in tension perpendicular to grain and shear; (c) shows the stresses in the longitudinal direction*

It can be seen that the experimentally obtained strains correlate very well with the computed FE-results. The stresses in the direction perpendicular to grain (see Figure 6.8a) follow the expected pattern, but show smaller values near the corners, as compared to the FE-model. The shear stresses of Figure 6.8b show a good correlation as well and show that the glulam sections above and below the hole behave like separate beams, each one carrying

half of the shear force of the full cross-section. The stresses parallel to grain direction show a very good agreement with the simulations at every location.

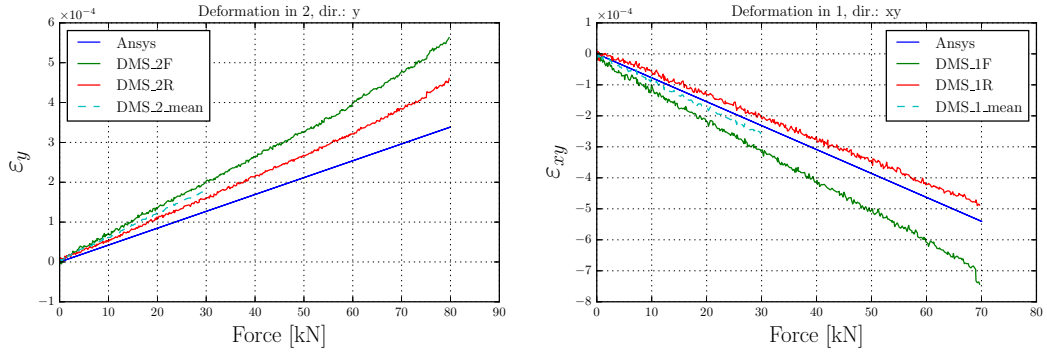

(a) ***(b)***

Figure 6.9: *Strains measured at strain gauges number 2 (a) and 1 (b) of specimen No. 16, located at positions indicated in Figure 6.4. The strains computed with the FE-model are presented as well.*

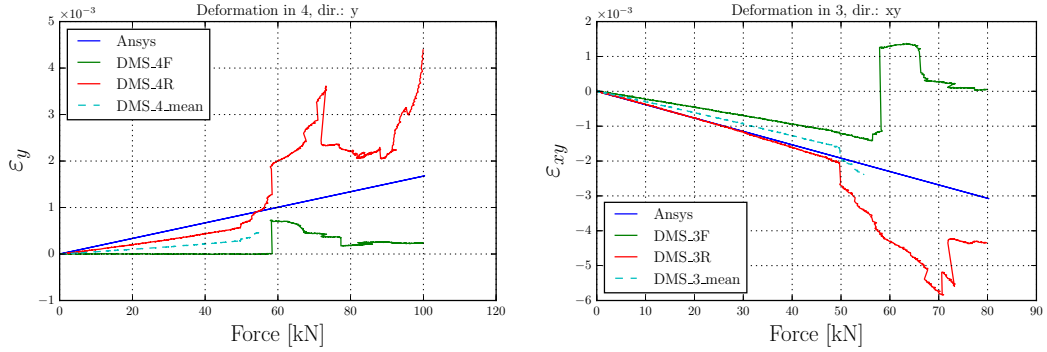

(a) ***(b)***

Figure 6.10: *Strains measured at strain gauges number 4 (a) and 3 (b) of specimen No. 13, located at positions indicated in Figure 6.4. The strains computed with the FE-model are presented as well.*

Figures 6.9 and 6.10 show exemplarily some load vs. strain paths for different strain gauges of specimens 13 and 16. The strains computed using the FE-model are included as well, and the average value between the strain gauges in the front and rear side of the beam are displayed as well. The graphs in the specified figures show a good correlation between the FE-model and the experimental data. It is possible to identify when the material begins to fail, i.e. when the crack propagates at the positions of each strain gauge.

Radiata pine specimens

The test data representations from the Radiata pine specimens were processed with regard to two different kinds of graphical representations. The first graphic type shows the normal and shear strains ε_y and ε_{xy}, respectively, along both horizontal paths starting from the upper

and bottom regions of tensile stress concentrations at the hole periphery, (see Figures 6.11 and 6.12) at a load $P = 30\,\text{kN}$. At the specified load the load-strain behavior is still linear elastic, which is substantiated by the second graphic type showing exemplarily the load vs. strain, ε_y and ε_{xy}, paths (Figures 6.13 and 6.14).

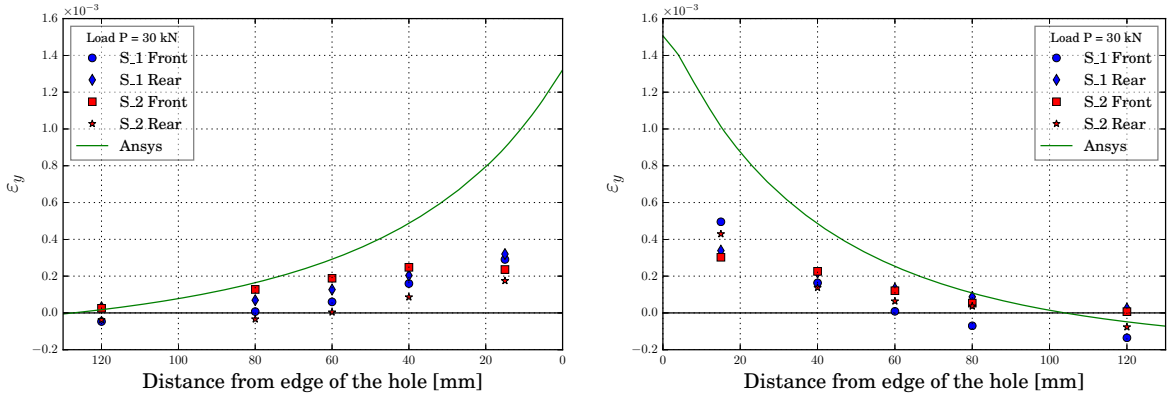

Figure 6.11: *Vertical strains along the path at the bottom (a) and upper (b) tension stress hole area for the specimens S_1 and S_2. In both plots the FE-computations are also presented, for comparison purposes.*

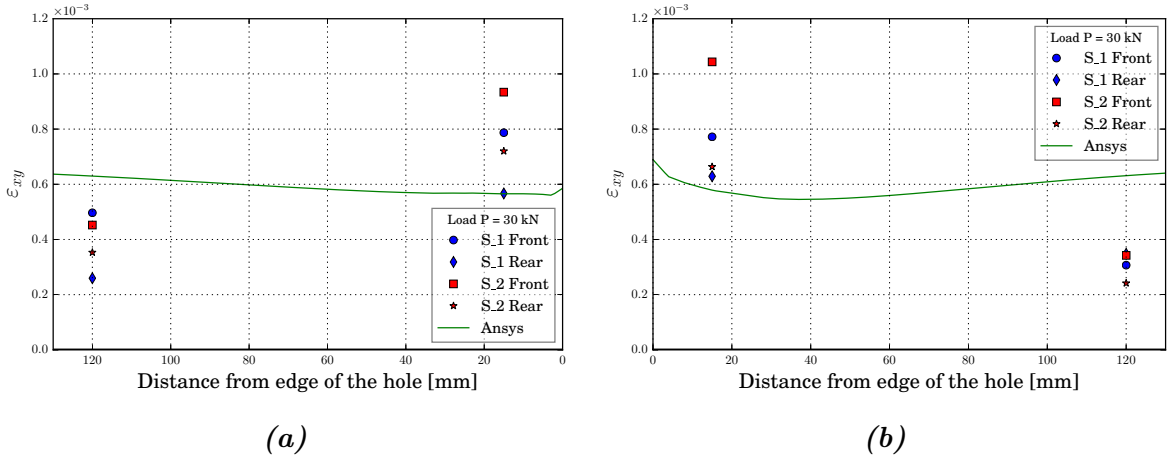

Figure 6.12: *Shear strains along the path at the bottom (a) and upper (b) tension stress hole area for the specimens S_1 and S_2. I both plots the FE-computations are also presented, for comparison purposes.*

Similarly, as it was observed from the comparison between the first results and the FE-model for the spruce specimens, it can be seen from Figures 6.11a and 6.11b that the obtained measurements and the simulation results coincide very well with regard to the shape of the distribution, but the absolute values from the model are larger for ε_y. In contrast, the shear stresses in this case don't show a good agreement with the FE-computations at the measured points. This could be explained by the fact that the elastic parameters that were assigned to the material are related to European spruce, which might not be well suited for the Chilean Radiata pine. Since the most relevant mechanical parameter for the deflection is the modulus of elasticity along the grain direction, and since this was the only value

that was actually measured (the others are obtained from the [14]), the results depending mainly on this property should give better results. Figure 6.15 presents the load-deflection relationship measured at specimen S_1; the comparison with the FE-results shows a very good correlation.

Figures 6.13 and 6.14 show a quite brittle behavior of the Radiata pine glulam beams, since they only exhibit two visible points of crack-progression (marked with red dots), contrary to what was observed in the spruce specimens, where many crack-progression load points were observed. It can be observed here that the crack propagation occurs at the same loads for both tensile-stressed hole periphery zones, as was explained before.

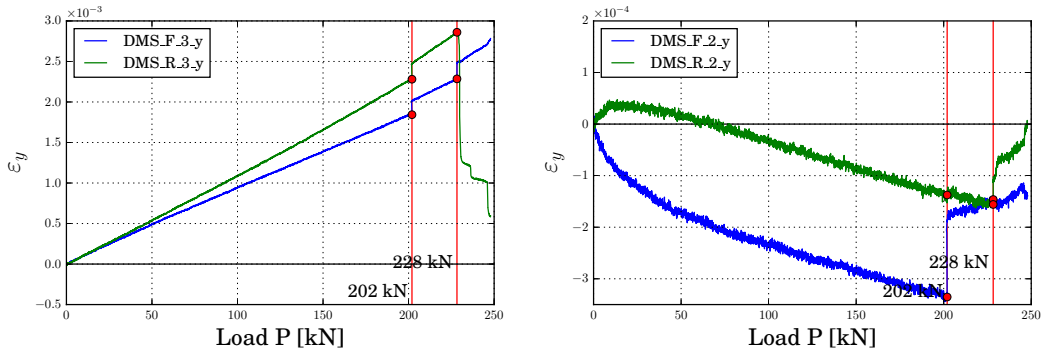

(a) *(b)*

Figure 6.13: *Strains measured on strain gauges number 3 (a) and 2 (b), located along the path starting from the corner 2 and 1 respectively. The crack growth can be seen from the jumps of the data from specimen S_1.*

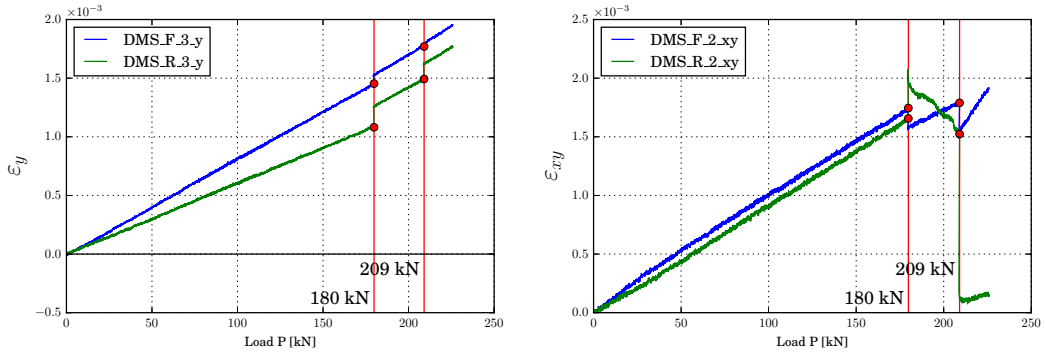

(a) *(b)*

Figure 6.14: *Strains measured on strain gauges number 3 (a) and 2 (b), located along the path starting from the corner 2 and 1 respectively. The crack growth can be seen from the jumps of the data from specimen S_2.*

6.3 Discussion

The comparison between the data obtained from the experiments and the FE-models results in a satisfactory agreement of the experimental and numerical determination of the stress

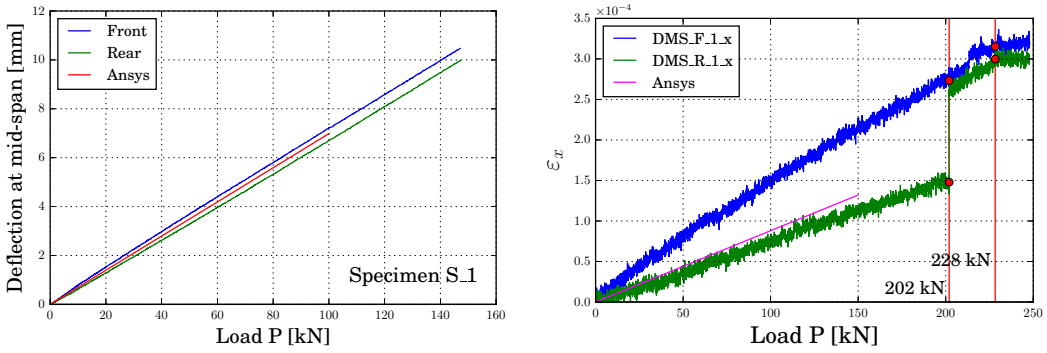

(a) *(b)*

Figure 6.15: *Comparison of the deflection at the mid-span of specimen S_1 and the results obtained from FE-Analysis (a) and strains parallel to grain direction of strain gauge location No. 1 (b)*

situation within the vicinity of the hole. It is expected that some level of discrepancy will occur, mainly due to the very nature of the material, which may present different kinds of local perturbations. However, the results help to validate the finite element models, which are the same models used in Chapter 5, and in turn validating the computations as well.

Conclusion

Material simplification in glulam beams and internal reinforcements

A good material idealization prevents unnecessary effort when solving a specific problem; poor material idealization may be used if the deficiencies are known to the person using it; poor material idealization used without knowing its weak spots can be catastrophic. Based on what was presented in this thesis, the following conclusions can be made regarding this subject:

- using 2-D FE-Models to represent the interaction between internal reinforcement and the glulam in the vicinity of the hole produces a larger influence of the named reinforcement, giving the impression that the reinforcement carries more load than it actually does;

- when creating 3-D FE-Models, internal reinforcements should not be defined using 1-D Beam elements, since they are not able to take the load appropriately when embedded within a mesh of 3-D elements, leading to a very small percentage of load-uptake of the reinforcement;

Regarding the design of holes acc. to DIN EN 1995-1-1/NA [18]

Some provisions of the German National Annex to DIN EN 1995-1-1 [18] dealing with the design of holes and the respective reinforcements in glulam beams, mentioned in the following, should be considered for amendment:

- the equation to compute the tensile force perpendicular to grain in the periphery of the hole due to the moment is incorrect and gives results extremely conservative for most cases. The proposed equation (see Eq. 5.1) seems to be a good alternative;

- the equation to calculate the effect of the shear force on the tensile force in the periphery of the hole, $F_{t,90,\mathrm{d}}$, gives unsafe results for some cases, depending on the shape and size of the hole. To solve this problem, a special term was introduced that takes into account the stress concentrations in relation to the hole's shape and ratio h_d/h. This equation is calibrated for different shapes and sizes of holes, which makes it adequate for all holes currently present in the Standard;

- the usage of a constant value for the corner radii in rectangular holes introduces a size-dependence regarding both *(i)* hole geometry, h_d/h ratio, —covered by the introduced α factor and, *(ii)* beam height, h, whose real influence should be further studied;

- due to the cylindrical anisotropy present in glulam, the most efficient positioning of the internal reinforcements lies at the mid-width of the cross-section of the glulam, where the tensile stresses reach their maximum values;

- according to the FE-Models and the experiments carried out, rod-like internal reinforcements cannot substantially reduce stresses perpendicular to grain in the region of crack initiation. Further, they are not able to alleviate the shear stresses present along the crack-plane and they do not stop the shear stress driven crack propagation once it has already begun. This means that checking the maximum shear stresses at the hole's periphery during the design process, only makes sense when lateral panel reinforcement is used, which allows to take up shear stresses as compared to vertically installed rods, which are ineffective against such stresses.

Bibliography

[1] Aicher, S. (2011). Glulam beams with internally and externally reinforced holes - test detailing and design. In *International Council For Research And Innovation In Building And Construction, Working Commission W18 - Timber Structures, Alghero, Italy*, volume 44.

[2] Aicher, S. and Dill-Langer, G. (2005). Effect of Lamination Anisotropy and Lay-Up in Glued-Laminated timbers. *Journal of Structural Engineering*, 131(7):1095–1103.

[3] Aicher, S. and Höfflin, L. (2001). Runde Durchbrüche in Biegeträgern aus Brettschichtholz. Teil 1: Berechnung. *Bautechnik*, 78(10):706–715.

[4] Aicher, S. and Höfflin, L. (2004). New design model for round holes in glulam beams. In *Proceedings of the 8th World Conference on Timber Engineering*, volume 1, pages 67–72, Lahti, Finalnd.

[5] Aicher, S. and Höfflin, L. (2006). Tragfähigkeit und Bemessung von Brettschichtholzträgern mit runden Durchbrüchen – Sicherheitsrelevante Modifikationen der Bemessungsverfahren nach Eurocode 5 und DIN 1052. Technical report, MPA Universität Stuttgart.

[6] Aicher, S. and Schrank, M. (2006). Shear reinforcement of glulam beams with glued-in steel rods – a case study. *Otto Graf Journal*, 17:143–160.

[7] Aicher, S. and Tapia, C. (2012). Glulam with laterally reinforced rectangular holes. In *World Conference on Timber Engineering*.

[8] Blaß, H. J., Ehlbeck, J., Kreuzinger, H., and Steck, G. (2004). *Erläuterungen zu DIN 1052: 2004-08; Entwurf, Berechnung und Bemessung von Holzbauwerken*. Deutsche Geselschaft für Holzforschung, Bayerstr. 57-59 80335 München.

[9] Boding, J. and Jayne, B. A. (1993). *Mechanics of wood and wood composites*. Krieger, Malabar, Florida, repr. with corr. edition.

[10] DIN 1052:2008. Design of timber structures – General rules and rules for buildings.

[11] DIN 20000-1:2013. Anwendung von Bauprodukten in Bauwerken - Teil 1: Holzwerkstoffe.

[12] DIN EN 1194:1999. Holzbauwerke - Brettschichtholz - Festigkeitsklassen und Bestim-

mung charakteristischer Werte; Deutsche Fassung EN 1194: 1999.

[13] DIN EN 13986:2010. Holzwerkstoffe zur Verwendung im Bauwesen — Eigenschaften, Bewertung der Konformität und Kennzeichnung; Deutsche Version FprEN 13986:2010. Einsprüche bis 2010-09-05 Vorgesehen als Ersatz für DIN EN 13986:2005-03.

[14] DIN EN 14080:2013. Holzbauwerke – Brettschichtholz und Balkenschichtholz – Anforderungen; Deutsche Fassung EN 14080:2013.

[15] DIN EN 14279:2009. Furnierschichtholz (LVL) – Definitionen, Klassifizierung und Spezifikationen;.

[16] DIN EN 14374:2005. Holzbauwerke – Furnierschichtholz für tragende Zwecke – Anforderungen; Deutsche Fassung EN 14374:2004.

[17] DIN EN 1995-1-1:2010. Eurocode 5: Design of timber structures – Part 1-1: General – Common rules and rules for buildings; German version en 1995-1-1:2004 + ac:2006 + a1:2008.

[18] DIN EN 1995-1-1/NA:2013. Nationaler Anhang – National festgelegte Parameter – Eurocode 5: Bemessung und Konstruktion von Holzbauten – Teil 1-1: Allgemeines – Allgemeine Regeln und Regeln für den Hochbau.

[19] DIN EN 636:2012. Sperrholz - Anforderungen; Deutsche Fassung EN 636:2012.

[20] Höfflin, L. (2004). *Runde Durchbrüche in Brettschichtholzträgern – Experimentelle und theoretische Untersuchungen*. PhD thesis, Universität Stuttgart.

[21] Höfflin, L. (2006). Tragfähigkeit und Bemessung von Brettschichtholzträgern mit runden Durchbrüchen – Sicherheitsrelevante Modifikationen der Bemessungsverfahren nach Eurocode 5 und DIN 1052. Technical Report 760 4050 3000, MPA, Universität Stuttgart.

[22] Hunter, J. (2007). Matplotlib: A 2D Graphics Environment. *Computing in Science Engineering*, 9(3):90–95.

[23] Jones, E., Oliphant, T., Peterson, P., et al.:2001–. SciPy: Open source scientific tools for Python. [Online; accessed 2014-10-10].

[24] Kolb, H. and Epple, A. (1985). Verstärkung von durchbrochenen Brettschichtholzbindern. Research report I.4 – 34810, Otto-Graf-Institute, Stuttgart.

[25] McKinney, W. (2010). Data Structures for Statistical Computing in Python. In van der Walt, S. and Millman, J., editors, *Proceedings of the 9th Python in Science Conference*, pages 51 – 56.

[26] Millman, K. J. and Aivazis, M. (2011). Python for Scientists and Engineers. *Computing in Science Engineering*, 13(2):9–12.

[27] Rumplmayr, R. (1999). Einfluss der zylindrischen Anisotropie und des gezielten Lamel-

leneinschnitts auf die Querzugfestigkeit von Brettschichtholz. Master's thesis, Universität Stuttgart.

[28] Z-9.1-453:2009. HECO-fix-plus-Schrauben und HECO-TOPIX-Schrauben als Holzverbindungsmittel Bescheid über änderung und Ergänzung zur Zul. vom 12.10.2005.

[29] Z-9.1-519:2014. SPAX-S Schrauben mit Vollgewinde als Holzverabindungsmittel. gültig bis 01.08.2017.

Appendix A

Experimental results

A.1 Graphic record of experiments

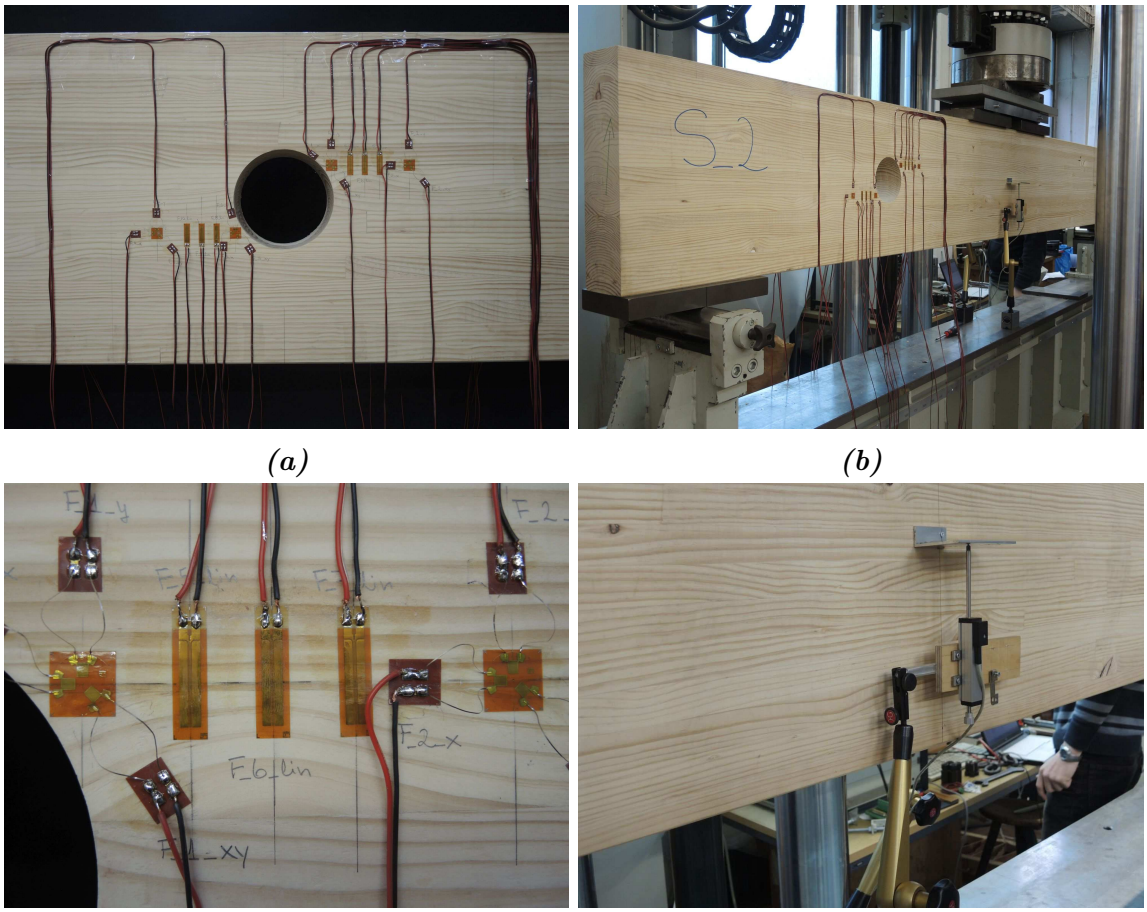

(a) *(b)*

(c) *(d)*

Figure A.1: *Figures of the configuration used for specimens S_1 and S_2. (a) shows the placement of strain gauges in the expected zones of crack initiation; (b) shows a general view of the configuration; In (c) a detail view of the strain gauges used on the top-right corner of the front size can be seen; (d) shows one of the path transducer positioned at the mid-span of the beam.*

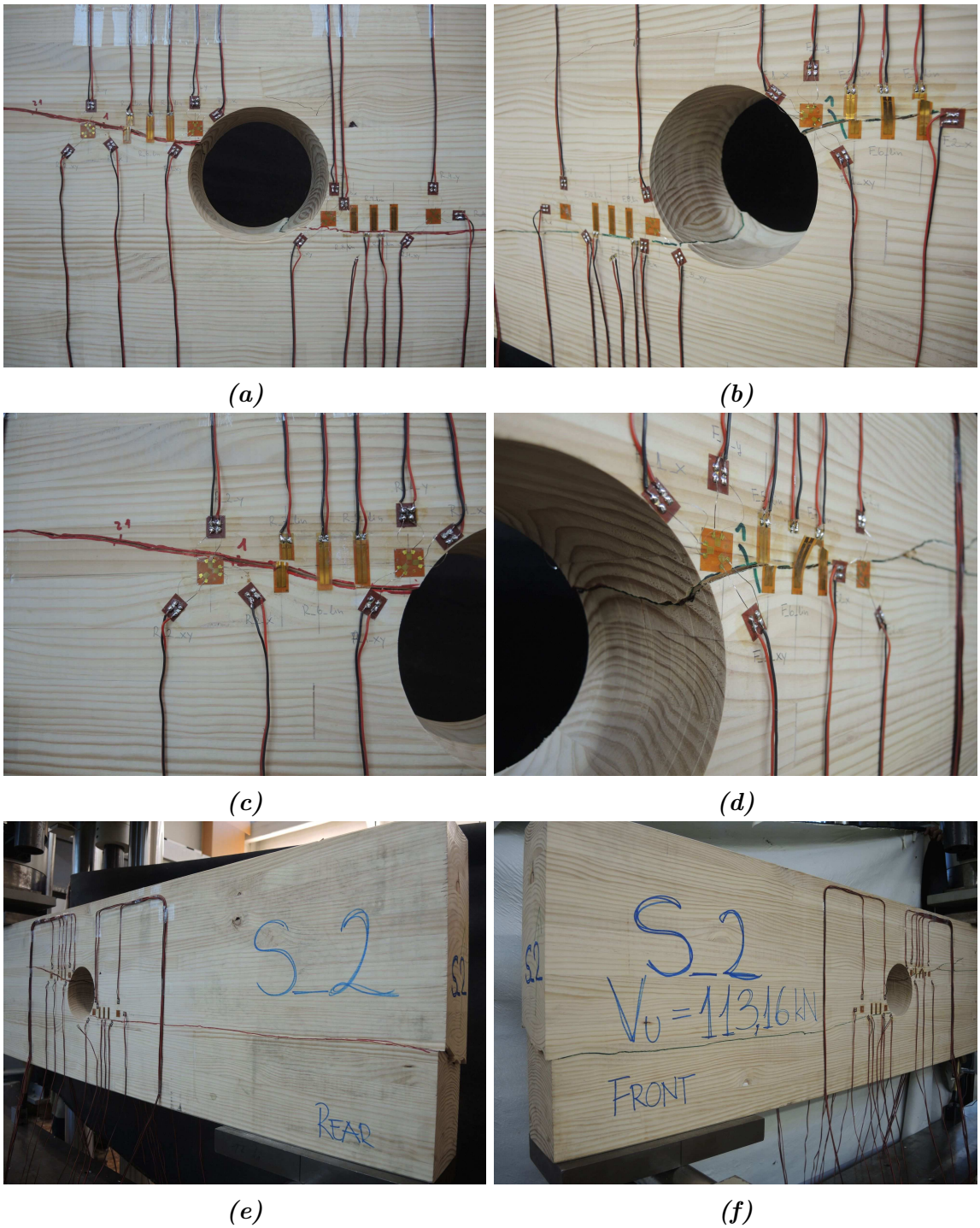

(a) ***(b)*** ***(c)*** ***(d)*** ***(e)*** ***(f)***

Figure A.2: *Figures of the specimen S_2 after failure. Figures (a), (c) and (e) show the rear side, whilst Figures (b), (d) and (f) show the front side.*

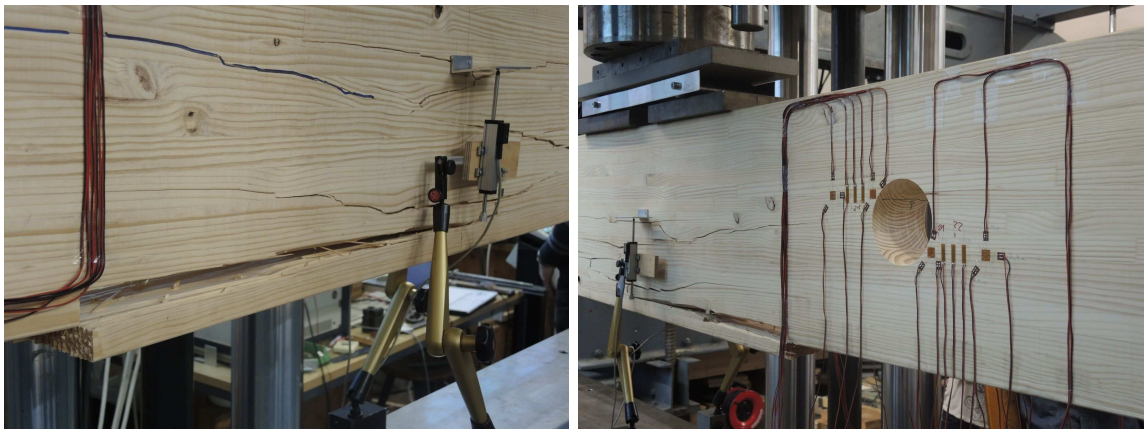

(a) ***(b)***

Figure A.3: *Figures of the bending failure of specimen S_1 (with reinforcements). (a) shows the front side and (b) the rear of the beam.*

(a) ***(b)***

(c) ***(d)***

Figure A.4: *Figures of the specimen S_3 (without reinforcements) after failure.*

A.2 Measured data

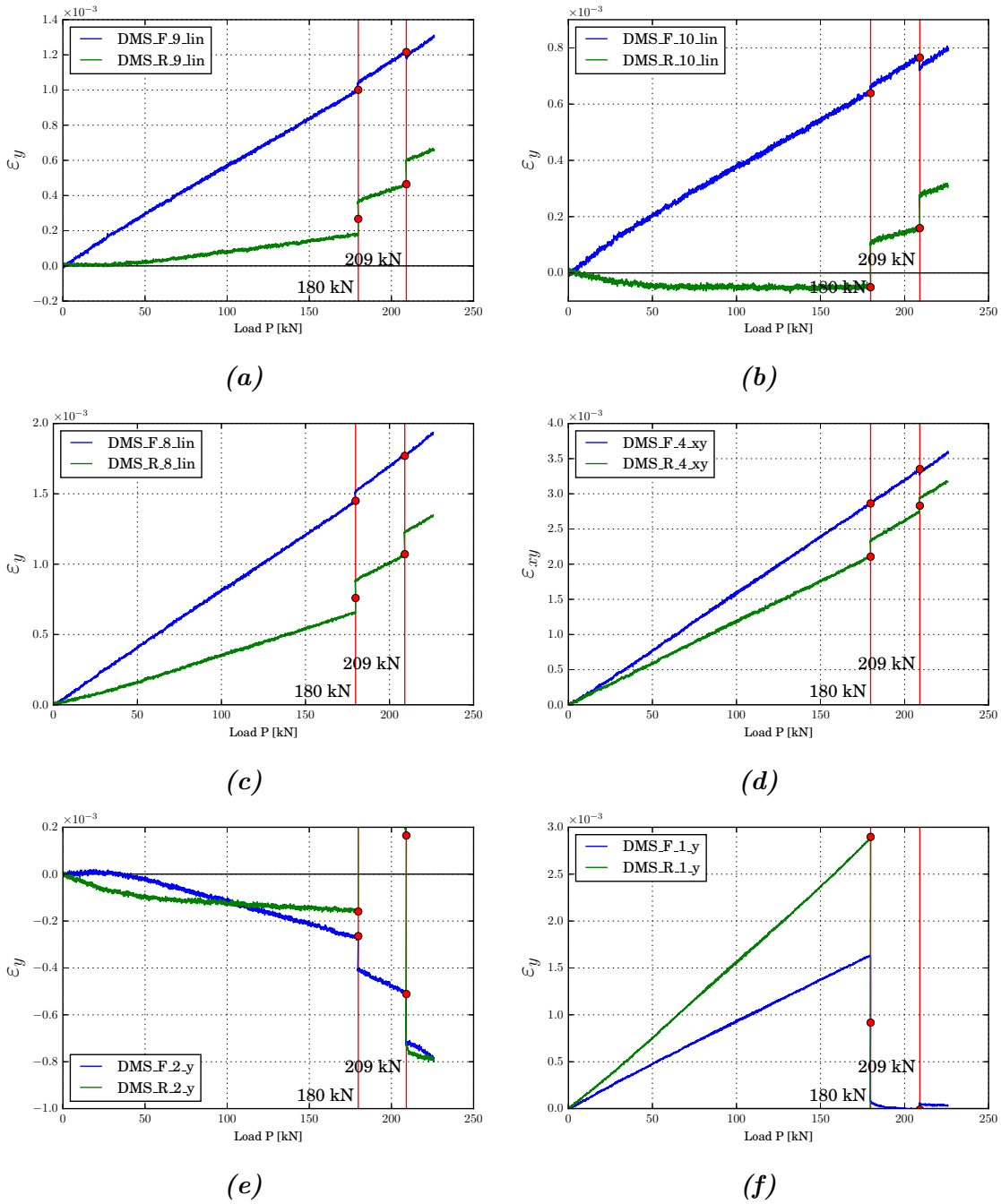

Figure A.5: *Results for the specimen S_2 for the strain gauges 9 (a), 10 (b), 8 (c), 4 (d), 2 (e) and 1 (f)*

Appendix B

Determining characteristic values for glulam made of Radiata pine (origin Chile)

B.1 Properties of the laminations

The mechanical properties of the laminations are taken from a test-report for the respective material, provided by MPA University of Stuttgart.

Table B.1: *Properties of the laminations acc. the test-report MPA University of Stuttgart*

$f_{t,0,\ell,k} =$	$15.4\,\mathrm{N/mm^2}$
$E_{\mathrm{mean}} =$	$15\,400\,\mathrm{N/mm^2}$
density, $\rho =$	$492\,\mathrm{kg/m^3}$

According to DIN EN 14080 [14] these laminations may be classified in the tension strength class T-15.

Table B.2 shows the results obtained for the bending strength of finger-joints in the respective laminations.

Table B.2: *Bending strength obtained for the finger-joints*

$f_{m,\mathrm{fj},k} =$	$51.8\,\mathrm{N/mm^2}$

B.2 Computation of characteristic values for the glulam beam

To calculate the bending strength of the glulam beam, characteristic (5 %-quantile) finger joint bending strength value, $f_{m,j,k}$, has to conform to a certain range, influenced by the tension strength of the laminations, as specified in Eq. B.1.

$$1,4 \cdot f_{t,0,\ell,k} \leq f_{m,\mathrm{fj},k} \leq 1,4 \cdot f_{t,0,\ell,k} + 12 \tag{B.1}$$

$$21.6\,\mathrm{N/mm^2} \leq f_{m,\mathrm{fj},k} \leq 33.6\,\mathrm{N/mm^2} \tag{B.2}$$

Since this is not the case for this particular laminations ($f_{m,\mathrm{fj},k} = 51.8\,\mathrm{N/mm^2} \gg 33.6\,\mathrm{N/mm^2}$), the maximal value of the permissible range could be used to compute the bending strength of the glulam timber in Equation B.3.

$$f_{m,g,k} = -2.2 + 2.5 \cdot f_{t,0,\ell,k}^{0.75} + 1.5 \cdot \left(\frac{f_{m,j,k}}{1.4} - f_{t,0,\ell,k} + 6\right)^{0,65} \tag{B.3}$$

$$= -2.2 + 2.5 \cdot 15.4^{0.75} + 1.5 \cdot \left(\frac{33.6}{1.4} - 15.4 + 6\right)^{0,65} \tag{B.4}$$

$$f_{m,g,k} = 25.7\,\mathrm{N/mm^2} \tag{B.5}$$

Table B.3 shows the computed characteristic values for a glulam beam built up with the studied laminations. According to these values the glulam may be classified as a *GL 25h*. The calculations made are shown in Equations B.1 through B.5.

Table B.3: *Characteristic values for a glulam beam built up using the studied Radiata Pine laminations acc. to DIN EN 14080 [14]*

Property	Characteristic value
$f_{m,g,k}$ =	25.7 N/mm²
$f_{t,0,g,k}$ =	20.6 N/mm²
$f_{t,90,g,k}$ =	0.5 N/mm²
$f_{c,0,g,k}$ =	25.7 N/mm²
$f_{c,90,g,k}$ =	2.5 N/mm²
$f_{v,g,k}$ =	3.5 N/mm²
$f_{r,g,k}$ =	1.2 N/mm²
$E_{0,g,\mathrm{mean}}$ =	16 170 N/mm²
$E_{90,g,\mathrm{mean}}$ =	300 N/mm²
$G_{g,\mathrm{mean}}$ =	650 N/mm²
$G_{r,g,\mathrm{mean}}$ =	65 N/mm²
$\rho_{g,k}$ =	541 kg/m³
$\rho_{g,\mathrm{mean}}$ =	–

In case the actual finger joint strength falls bellow the lower limit of the range in Eq. B.2 the beam bending strength as described from Eq. B.3 is overestimated. In case, as given

here, $f_{m,j,k}$ is larger than the upper limit, the beam equation delivers a conservative result. However, no higher value that the upper limit, i.e. here $f_{m,j,k} = 33.6\,\mathrm{N/mm^2}$ shall be chosen for implementation in Eq. B.3.

Appendix C

Characteristic load capacity of a glulam beam (with specific dimensions and load configuration) without hole

Description of the problem

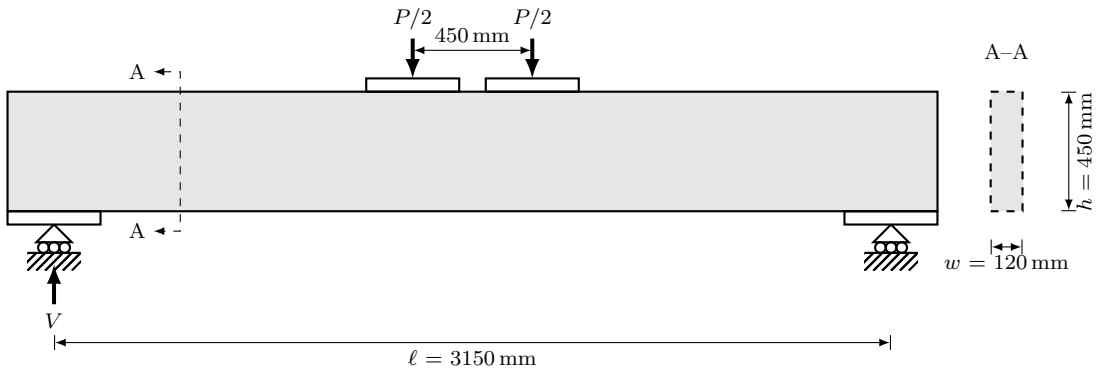

Figure C.1: *Dimensions, notations and load configuration of investigated glulam beams without hole (all dimensions in mm)*

Table C.1: *Characteristic values for the analyzed beam*

Property	
Class	GL 32h
$f_{m,k}$	$32\,\mathrm{N/mm^2}$
$f_{v,k}$	$3.5\,\mathrm{N/mm^2}$

Moment capacity

The maximum moment within the beam, $M_{\max}$, is found as

$$M_{\max} = \frac{P}{2} \cdot 1350\,\text{mm} \tag{C.1}$$

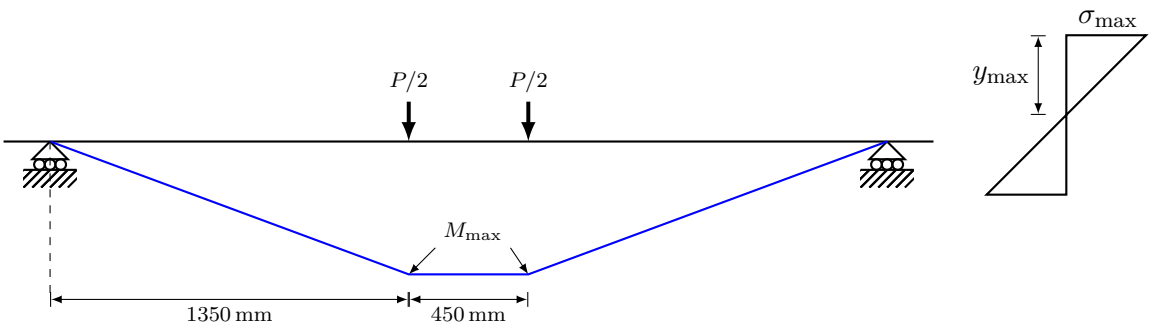

Figure C.2: *Moment diagram and distribution of stresses parallel to grain direction along cross-sectional depth*

The characteristic value of the bending strength, $f_{m,k}$, can be related with the load, P as

$$f_{m,k} = \frac{M \cdot y_{\max}}{I} \tag{C.2}$$

$$32\,\text{N/mm}^2 = \frac{\frac{P}{2} \cdot 1350 \cdot \frac{450}{2}}{\left(\frac{450^3 \cdot 120}{12}\right)}, \tag{C.3}$$

from where the characteristic maximum load, $P_{\max,k}$, can be obtained as:

$$P_{\max,k} = 192\,\text{kN} \tag{C.4}$$

Shear force capacity

The maximum shear force within the beam, $V_{\max}$, is $P/2$

The maximum shear stress in the beam is:

$$\tau = \frac{3V}{2 \cdot h \cdot k_{\text{cr}} \cdot b} \tag{C.5}$$

According to [17] the width needs to be reduced by the crack factor $k_{cr} = 2.5/f_{v,k}$. This factor considers the change in bearing capacity that a timber element might experience over a long period of time, due to crack formation expected based on a statistical distribution. In this case the beam element such factor has no meaning, since the load application occurs over a very short period of time, hence a value $k_{cr} = 1$ is used.

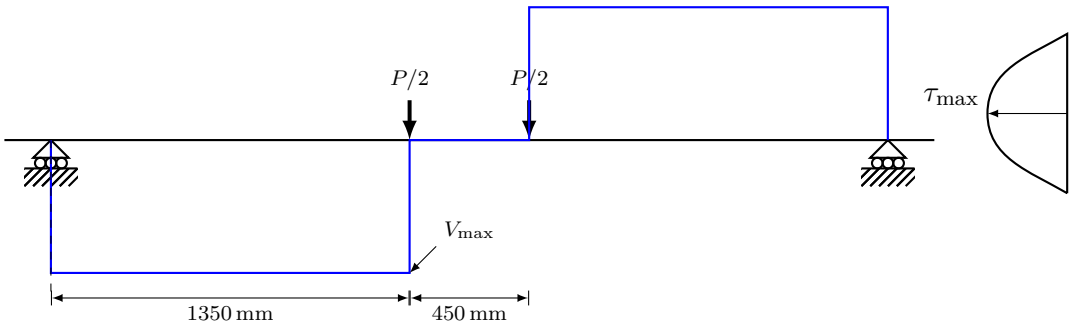

Figure C.3: *Shear diagram and shear stress distribution along cross-sectional depth*

$$f_{v,k} = \frac{2V}{3 \cdot h \cdot b} \tag{C.6}$$

$$3.5\,\mathrm{N/mm^2} = \frac{2V}{3 \cdot 450 \cdot 120} \tag{C.7}$$

from where a maximum shear capacity, $V_{\max,k}$, is found.

$$V_{\max,k} = 283\,\mathrm{kN} \tag{C.8}$$

$$P_{\max,k} = 567\,\mathrm{kN} \tag{C.9}$$

This means that the bearing capacity of the beam is controlled by the bending strength,

$$P_{\max} = 192\,\mathrm{kN} \tag{C.10}$$